T2R2 東京科学大学 リサーチリポジトリ
Science Tokyo Research Repository

論文 / 著書情報
Article / Book Information

題目(和文)	コンビナトリアルレーザー薄膜堆積法による遷移金属ドープ酸化物薄膜の作製と評価
Title(English)	Combinatorial laser molecular beam growth and characterization of transition metal doped oxide thin films
著者(和文)	村上真
Author(English)	
出典(和文)	学位:博士(工学), 学位授与機関:東京工業大学, 報告番号:甲第5420号, 授与年月日:2003年3月26日, 学位の種別:課程博士, 審査員:
Citation(English)	Degree:Doctor (Engineering), Conferring organization: Tokyo Institute of Technology, Report number:甲第5420号, Conferred date:2003/3/26, Degree Type:Course doctor, Examiner:
学位種別(和文)	博士論文
Type(English)	Doctoral Thesis

Powered by T2R2 (Science Tokyo Research Repository)

Combinatorial Laser Molecular Beam Growth and Characterization of Transition Metal Doped Oxide Thin Films

Makoto Murakami

Department of Innovative and Engineered Materials
Tokyo Institute of Technology

Combinatorial Laser Molecular Beam Growth and Characterization of Transition Metal Doped Oxide Thin Films

Makoto Murakami

Contents

Chapter 1 General Introduction

1-1 Oxide complex and Laser Molecular Beam Epitaxy (LMBE)

Metal oxides possess such a wide variety of interesting physical properties as high temperature superconductivities, colossal magnetoresistance (CMR), quantum paraelectricity, and giant piezoelectricity. Furthermore, recent remarkable progress of oxide thin film technology, such as molecular beam epitaxy (MBE), metal-organic chemical vapor deposition, suputtering, sol-gel methods, pulsed laser deposition (PLD) and laser molecular beam epitaxy (LMBE), enables us to fabricate good quality oxide thin films. LMBE is an especially useful process for fabricating stoichiometric oxide thin films with atomically controlled equipped with in-situ RHEED system.

As a result of enormous time-consuming efforts, various new materials and phenomena have been discovered in metal oxides. However, metal oxide materials have been complicated along with property progressing. Considering of development trend of superconducting and ferroelectric materials, complexity of materials are increasing. The history of superconducting materials is shown in Fig. 1-1. Superconducting critical point temperature (T_C) vs. year of investigated. The first element of superconducting material, which is Hg with Tc = 4.15K, is one component. Then the number of element is increasing, recent most highest T_C (> 160K at high pressure) material HgBaCaCuO is composed of 5 elements. These trends have been seen in any kinds of materials and physical properties. To improve the developing speed of material science, novel ideas are necessary. The remarkable turning point, combinatorial chemistry is first concerned in the development for new drug synthesis. Discussing about combinatorial chemistry will be shown in section 1-3.

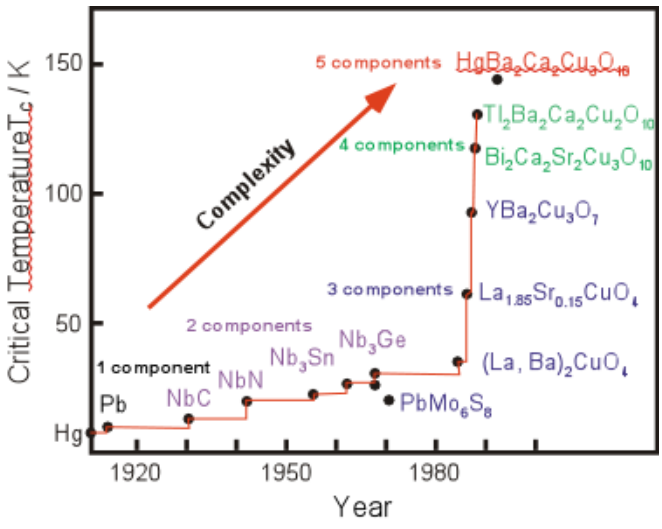

Fig. 1-1 The increase of T_C versus year. This figure shows that the constituent numbers of the superconductors are proportional to the corresponding T_C value.

1-2 Diluted Magneto Semiconductor (DMS)[1,2]

Recently, magnetic semiconductors based on non-magnetic semiconductors, called diluted magnetic semiconductors (DMSs), can be realized by alloying with magnetic elements.

Spins can be controlled by carrier, photon and photon-carrier spin interactions. DMSs have been attracted for the new device application with these special features. The concentration works as a DMS have been interested in II-VI, III-V semiconductors. The highest curie temperature was 110K of (Ga,Mn)As. However, the materials, which ferromagnetic magnetism remains above room temperature, are critically important in the development of spintronics as spin injectors for semiconductor heterostructures that can operate without cryogenic cooling. The backgrounds about DMS are discussing follows.

Coexistence of ferromagnetism and semiconducting properties in Eu chalocogenides and semconducting spinels opened a rich field of interplay between magnetic cooperative phenomena and semiconducting properties. In these magnetic semiconductors, extensively studied in the late 1960s through early 1970s, exchange interactions between the electrons in the semiconducting band and the localized electrons at the magnetic ions leads to a number of peculiar and intriguing properties.

Study of DMSs and its heterostructures had been centered mostly on II-VI based DMSs such as CdTe and ZnS, where the valence of group 2 cations is identical to that of the common magnetic ions like Mn^3. Although this made them relatively easy to prepare, difficulty in doping of II-VI based DMSs to p- and n-type made the material less attractive for applications. The magnetic interaction in II-VI DMSs is dominated by the Mn spins, which results in paramagnetic, antiferromagnetic, or spin glass behavior. The effort to grow such III-V based DMSs was rewarded with successful MBE growth of uniform (In,Mn)As films on GaAs substrates[4]. Subsequent discovery of hole-induced ferromagnetic order in p-type (In,Mn)As[5] encouraged reresarchers to investigate GaAs-based systems[6] and lead to the successful growth of ferromagnetic (Ga,Mn)As[7].

The key of fabrication of high doping Mn in III-V semiconductors were low temperature MBE growth technique. When the Mn flux or the substrate temperature or both were too high, an RHEED pattern indicative of the appearance of the MnAs (NiAs-structure) second phase on the surface emerges. Fig. 1-2 shows schematic phase diagram showing the relation between growth parameters (substrate temperature and Mn concentration) and the properties of (Ga,Mn)As grown by MBE.

Magnetic properties of $(Ga_{1-x}Mn_x)As$ are discussing. The highest ferromagnetic transition temperature T_C so far obtained is 110K[8] around x = 0.05. Below x = 0.005 no

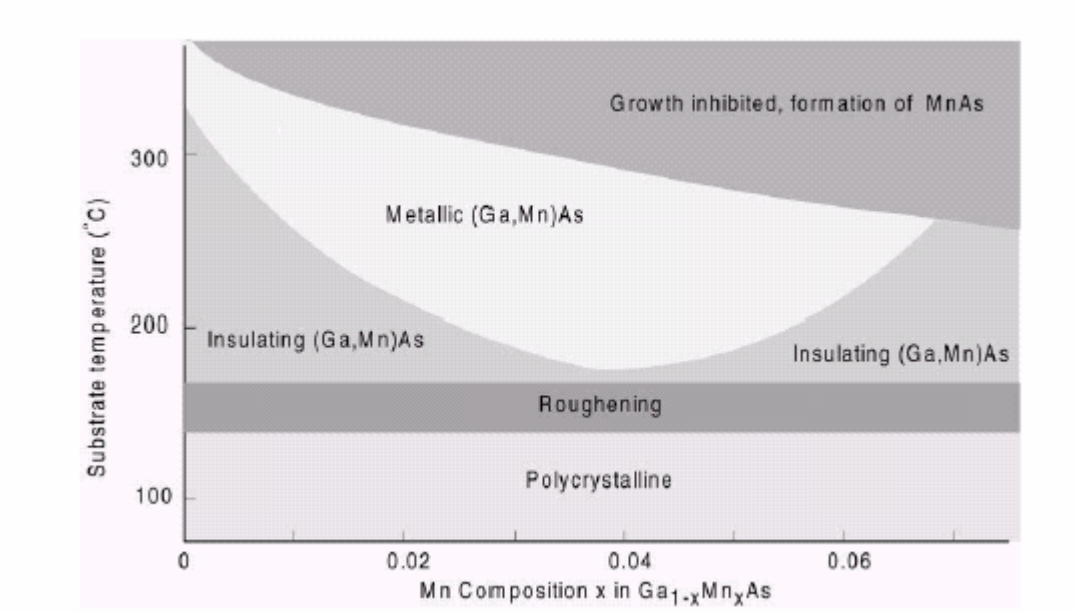

Fig. 1-2 Schematic phase diagram showing the relation between growth parameters (substrate temperature and Mn concentration) and the properties of (Ga,Mn)As grown by MBE.

ferromagnetism was detected. The relationship between x and T_C was found approximately 2000x ± 10K up to x = 0.05. Fig. 1-3 shows summarize the x dependence of T_C for 200 nm $(Ga_{1-x},Mn_x)As$ grown on $(Al_x,Ga_{1-x})As$ buffer layers (x_{Al} = 0.9).

Origins of ferromagnetism are discussing follows. Since the magnetic interaction between Mn has been shown to be antiferromagnetic in n-type (In,Mn)As [9] and in semi-insulating fully compemsated (Ga,Mn)As using Sn as a donor[10], the ferromagnetic interaction in magnetic III-Vs is most likely hole induced. There are currently two approaches to the present carrier-induced ferromagnetic interaction; one starts from the interaction between a carrier Fermi sea and localized magnetic moments, and the other starts from a d-band formed by the magnetic impurity, which is partially occupied because of the presence of carriers (holes). Discussion about Ruderman – Kittel – Kasuya - Yoshida(RKKY) interaction

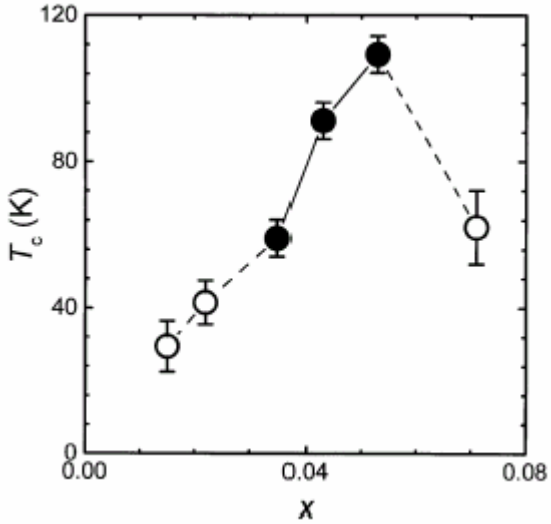

Fig. 1-3 Ferromagnetic transition temperature Tc determined from magnetotransport measurements as a function of Mn composition x. Closed circles show metallic samples, whereas open circles show insulating samples.

and double exchange interaction will be discussed in Appendix *II*.

Since the ferromagnetism in Mn-doped III-Vs is hole induced, change in hole concentration is expected to result in modification of ferromagnetic interaction among Mn spins and lead to change in transition temperature. This has been demonstrated in insulating-gate field-effect transistor (FET) structure having an (In,Mn)As channel[11]. The 5 nm thick channel layer (x = 0.03) was grown on a buffer layer structure designed in such a way to relax almost all the lattice mismatch between the epitaxial structure and the GaAs substrate. Fig. 1-4 shows the magnetization curves at three different gate voltages V_G (+125, 0, -125 V) applied to the gate of the magnetic FET, having a 0.8 μm gate insulator. Here, magnetization is measured by the Hall resistance, which is proportional to M. At zero gate bias, the channel is weakly ferromagnetic at 22.5 K as can be seen from the presence of small hysteresis. Application of positive gate voltage partially depletes the holes and reduces the ferromagnetic interaction mediated by them resulting in a paramagnetic magnetization curve without hysteresis. When holes are accumulated by applying negative gate voltage, a clear hysteresis appears. The magnetization curve resumes its original curve as the gate voltage returns to 0V. The 125 V swing gives rise to + 6% change in hole concentration and results in the transition temperature change of +4%. This agrees well with that expected from the mean-field model by Dietl et al.[12]. It is worth noting that photo generated carriers can also be used to modify the properties of (In,Mn)As, as has been recoiled in literatures[13,14].

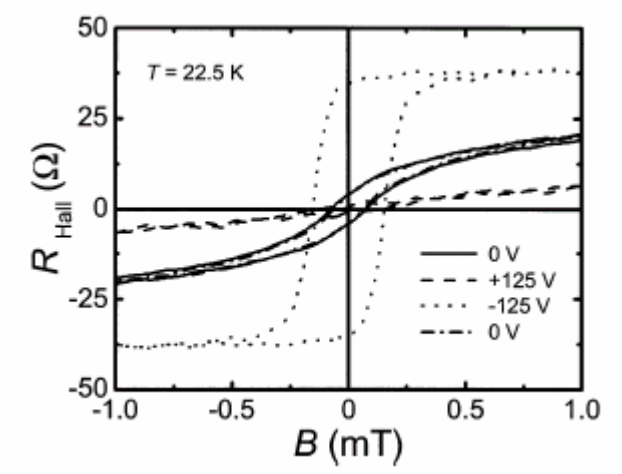

Fig. 1-4 Hall resistance, R_{Hall}, of an insulated gate (In,Mn)As FET as a function of magnetic field under three different gate voltages. R_{Hall} is proportional to the magnetization of the (In,Mn)As channel. Positive gate voltage of 125 V partially depletes holes and results in weaker ferromagnetic interaction and a paramagnetic response, whereas negative gate voltage produces square hysteresis. Zero gate voltage results before and after application of positive and negative gate voltage are virtually identical.

Carrier control and bandgap engineering are one of the most important techniques in semiconductors researches and applications. Furthermore, development of DMS field, doping technology will be more important. Thinking about development of DMSs, it will take a lot of

try and error to optimize the doping concentration, doping element, and fabrication conditions such as fabrication temperature and process gas partial pressure. From these point of views, high speed synthesis and high-throughput screening technique will be impossible to develop DMS because for the example of GaMnAs, InMnAs III-V systems.

We first succeeded in discovering of transparent ferromagnetic semiconductor Co doped titanium dioxide (TiO_2) even above room temperature through the combinatorial screening. The discovery of this transparent magnet above room temperature allows us a possibility to develop functional device applications. From these points of view, combinatorial chemistry is becoming a more and more attractive concept. Combinatorial technique are discussing in next section 1-3.

1-3 Combinatorial Chemistry[15]

Combinatorial chemistry and high-throughput screening represent a powerful research strategy as applied to materials science as shown in before sections. The combinatorial process aims at efficiently exploring the large parameter space that controls the properties of a product through the combination of rapid parallel or combinatorial synthesis of vast numbers of compounds and subsequent high-throughput assaying of these compounds for any give application. By combinatorially varying process and reaction conditions, combined with combinatorial synthesis, the total number of experiments one can screen rises experiments one can screen rises exponentially, which drastically increases the chances of identifying a new material or catalyst.

Combinatorial chemistry, which was originally developed in drug industry[16], starts attracting much interest for the discovery of new or improved materials. From the periodic table, we can readily see many more possible combinations of elements to produce inorganic compounds than to produce organic compounds.

The properties of many functional solid–state materials arise from complex interactions involving the host structure, dopants, defects, and interfaces, and therefore they depend heavily on composition and processing conditions. Conventional one-at-a-time synthesis and evaluation is generally a long and expensive process, and combinatorial materials science holds great promise in facilitating the materials discovery and optimization process. Fig. 1-5 shows schematically the combinatorial process in one manifestation as applied to materials deposited by vapor methods in two-dimensional arrays. A diverse library of different materials in created through automated synthesis. The libraries are then subjected

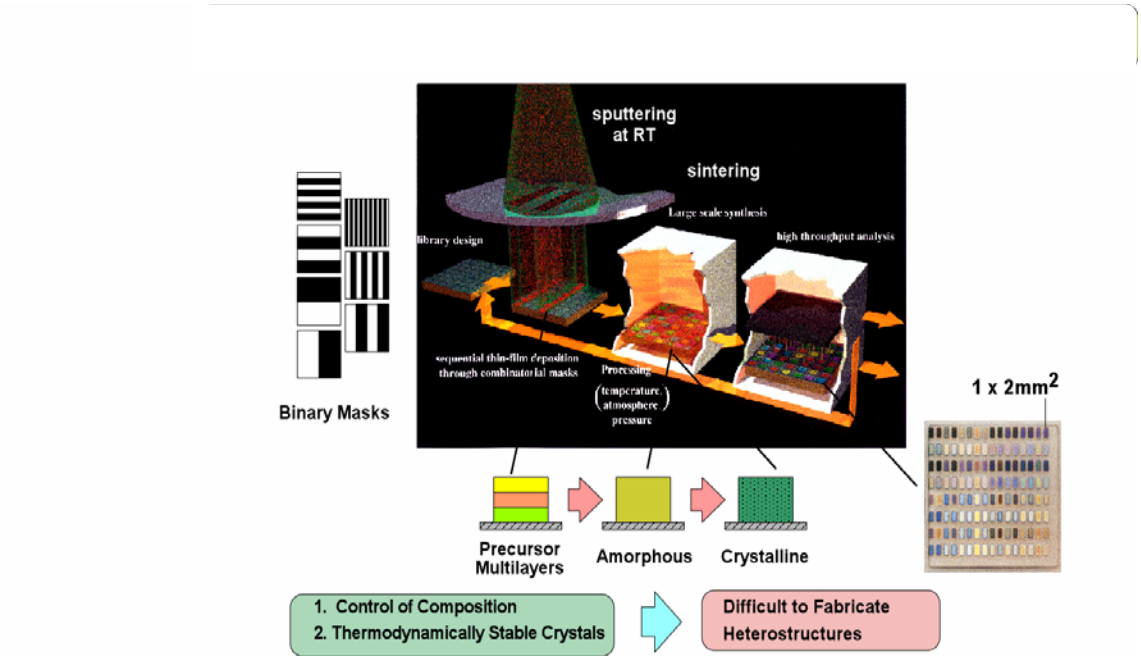

Fig. 1-5 Combinatorial materials discovery: a diverse library containing large numbers of individual samples in a spatially addressable two-dimensional array format is deposited by one of several automated deposition methods. Each spatial location represents a different composition or processing history. Multiple high-throughput screening for a variety of specific or general properties identifies lead materials that can be used to guide the design of subsequent libraries to search for new materials or property relationships.

to one or multiple screens for a variety of specific or general properties, and the data trends within the library are compared to previously created libraries to search for new materials or property relationships.

Unlike the case of drug discovery, where the use of solid-phase resins has proven important in combinatorial synthesis, solid-state materials synthesis often relies on sample preparation at temperatures in excess of 800°C, and two-dimensional, spatially addressable arrays of samples have emerged as the standard library framework.

Thin-film vapor deposition is commonly used in the semiconductor and some oxide materials synthesis to deposit thin films of material onto a substrate. A typical vacuum deposition system for combinatorial materials science has several source materials and is used in conjunction with masking techniques (physical or shadow masks, movable shutters, or photolithography) to sequentially or simultaneously deposit different materials in particular areas of the substrate. The design of masks and the sequence in which they are used determine which materials are deposited at any given location of the substrate. By altering the sequence,

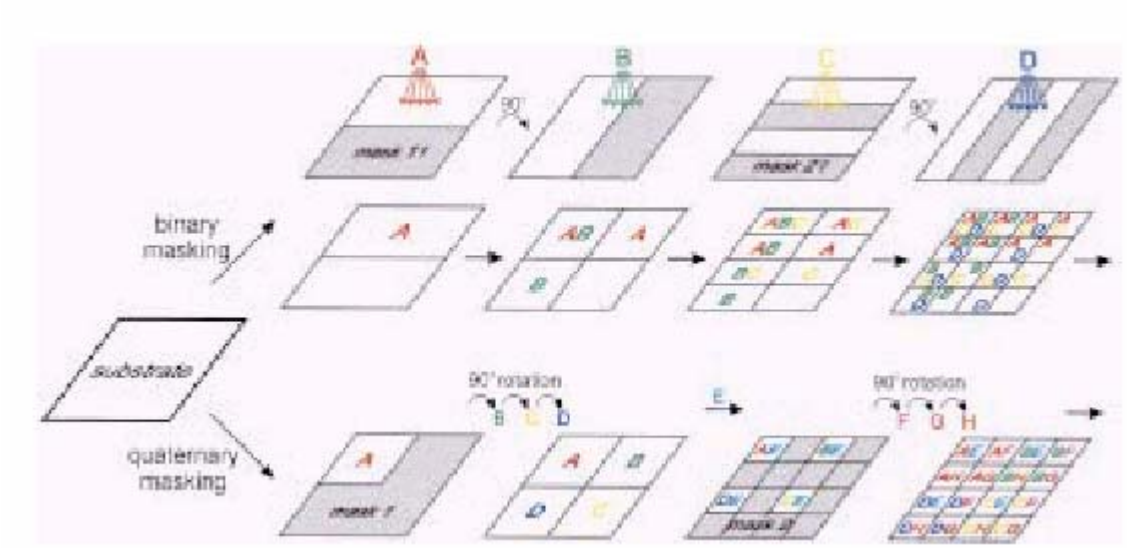

Fig. 1-6 Binary and quaternary masking strategies for combinatorial materials library fabrication.

time, and rate of deposition, it is possible to control the exact chemical composition of each element in the library.

The efficiency with which one can survey a particular materials landscape of interest is dictated by the masking strategy employed[17]. Simple binary and gradient masks are useful for optimizing the composition of a known material. In the binary masking strategy only half of the substrate area is exposed to thin-film deposition with different patterns (1,2,4,...stripes oriented in two different directions) in each step (Fig. 1-6) The number of different compositions after N steps is 2^N, which includes all possible combinations of N elements. Gradient or x-y shutter masking utilizes movable masks that expose or shield certain areas of the substrate, which allows for controlled concentration and/or thickness variations of the deposited films. Subsequently, the films are heated to a high temperature to be crystallized. Hence, the products obtained are generally in thermal equilibrated poly-crystalline phase.

Recent progress in thin film technology has been making possible to fabricate atomically controlled lattices and heterojunctions even if they are not in thermodynamically stable phases by laser MBE. The formation of atomically defined structures, however, requires a lot of time due to the necessity of optimization parameters. In order to provide a breakthrough in this situation, we have developed a novel prototype technology denoted as combinatorial laser MBE (CLMBE). CLMBE apparatus and combinatorial technique development will be discussed in next chapter. And demonstrations of CLMBE chamber also discussed in next chapter. Through these experiments we show the potentials of the

combinatorial chemistry not only for high-throughput synthesis and screening, but also for reducing statistical errors in experiments.

1-4 Organization of the Thesis

First, development of combinatorial laser MBE (CLMBE) apparatus, which is laser MBE combined with powerful combinatorial concept, will be discussed. With this CLMBE apparatus, following studies are carried out:

Titanium dioxide (TiO_2) which is famous as photo-catalyst, $Sr_xBa_{1-x}Nb_2O_6$ (SBN) which is ferroelectric materials to be expected photorefractive application, ZnO which is excitonic UV lasing at room temperature, and Eu doped Y_2O_3 which is red fluoresced materials.

Development of CLMBE apparatus, combinatorial fabrication techniques, and combinatorial characterization apparatuses will be discussed in Chapter 2. And also discussed in Chapter 2 about application to Mg doped ZnO and Eu doped Y_2O_3 system with these technique. Furthermore, investigations of TiO_2 will be discussed in Chapter 3 to Chapter 6 with combinatorial technique. Structural control of TiO_2 and optical characterization of high-quality anatase thin films will be discussed in Chapter 3, characterization and photo-catalytic screening of 3d transitions metals doped TiO_2 combinatorial libraries will be discussed in Chapter 4, discovery of room temperature ferromagnetic oxide materials of Co doped TiO_2 will be discussed in Chapter 5, and structural characterization and ferromagnetic properties of Co doped TiO_2 thin films in detail will be discussed in Chapter 6. And fabrication and characterization of SBN will be discussed as an appendix *I*. And related magnetic theory will be discussed in Appendix *II*.

Reference

[1] Hideo Ohno, J. Magn. Magn. Matter. 200 (1999) 110-129

[2] H. Ohno, F. Matsukura, Y. Ohno, Solid State Comun. 119 (2001) 281-289

[3] J. K. Furdyna, J. Kossut (Sds.), Semiconductor and Semimetals, Vol. 25, Academic, New York, 1988.

[4] H. Munekata, H. Ohno, S. Von Molnár, A. Segmüller, L. L. Chang, L. Esaki, Phys. Rev. Lett. 63 (1989) 1849.

[5] H. Ohno, H. Munekata, T. Penney, S. Von Molnár, L. L. Chang, Phys. Rev. Lett. 68 (1992) 2664.

[6] J. De Boeck, R. Oesterholt, A. Van Esch, H. Bender, C. Bruynseraede, C. Van Hoof, G. Borghs, Appl. Phys. Lett. 68 (1996) 2744.

[7] H. Ohno, A. Shen, F. Matsukura, A. Oiwa, A. Endo, S. Katsumoto, Y. Iye, Appl. Phys. Lett. 69 (1996) 363.

[8] F. Matsukura, H. Ohno, A. Shen, Y. Sugawara, Phys. Rev. B 57 (1998) R2037.

[9] S. Von Molnár, H. Munekata, H. Ohno, L. L. Chang, J. Magn. Magn. Mater. 93 (1991) 356.

[10] Y. Satoh, N. Inoue, Y. Nishikawa, J. Yoshino, Third, Symposium on Physcs and Application of Spin Related Phenomena in Semiconductors, 17-18 Nov. 1997, Sendai, Japan, P. 23.

[11] H. Ohno, D. Chiba, F. Matsukura, T. Omiya, E. Abe, T. Dietl, Y. Ohno, K. Ohtani, Nature 408 (2000) 944.

[12] T. Dietel, H, Ohno, F. Matsukura, J. Cibert, D. Ferrand, Science 287 (2000) 1019.

[13] S. Koshihara, A. Oiwa, M. Hirasawa, S. Katsumoto, Y. Iye, C. Urano, H. Takagi, H. Munekata, Phys. Rev. Lett. 78 (1997) 4617.

[14] A. Oiwa, T. Slupinski, H. Munekata, Appl. Phys. Lett. 78 (2001) 518.

[15] Brend Jandeleit, Dieter J. Schaefer, Timothy S. Powers, Howard W. Turner, and W. Henry Weinberg, Angew. Chem. Int. Ed. 38 (1999) 2494-2532.

[16] M. J. Plunkette, J.A. Ellman: Scientific American: April, 54 (1997)

[17] Potential Masking Systems and Methods for Combinatorial Library Synthesis, E. W. McFarland, E. Danielson, M. Devenney, C. Warren (Symyx Technologies), WO-A 98/14641, 1998; b) Systems and Methods for the Combinatorial Synthesis of Novel Materials, X. D. Wu, Y. Wang, I. Goldwasser (Sumyx Technologies), WO-A 98/47631, 1998.

Chapter 2 Combinatorial Laser Molecular Beam Epitaxy Apparatus and Combinatorial Characterization Tools

2-1 Combinatorial Laser Molecular Beam Epitaxy (CLMBE) apparatuses

Giant Combinatorial Chamber

Laser MBE is an excellent technique for fabricating oxide thin films. Combing powerful combinatorial concept[1] with laser MBE method, we developed combinatorial laser MBE (CLMBE) apparatus[2] [Fig.2-1]. As shown in Fig.2-2, the CLMBE apparatus is composing of three rooms, Pre-heating chamber (Pre-H), Deposition chamber (Depo) and Post- annealing chamber (Ann). They are all related to thin films fabrication process. In Pre-H, the substrate surface was cleaned by burning out surface carbon. Fabricating combinatorial thin films was carried out in Depo [Fig.2-3 (a)]. In Ann, the fabricated thin films were annealed at various oxygen pressures from UHV to atmosphere. This can be defined as "Continuous materials factory", because we can continuously fabricate combinatorial thin films. Specially, Depo chamber has some good characters. As shown in Fig. 2-3 (a), this room has masking system, multi target system and scanning refraction high-energy electron diffraction (RHEED) system. Combinatorial mask placed between target and substrate is about 2mm away from substrate. Six targets were placed in target holders separated by plates to avoid inter-contamination during laser ablation. KrF excimer laser (λ = 248 nm) (Lmbda-physik Compex 102) was used for beam generation. The laser was introduced into Depo chamber at a incident angle of 30° through a fused quartz window. The laser beam is focused on the surface of sintered ceramic targets by focusing lens. We used a halogen lamp heater having an output power of 1.5W at 100V as a source for heating substrate.

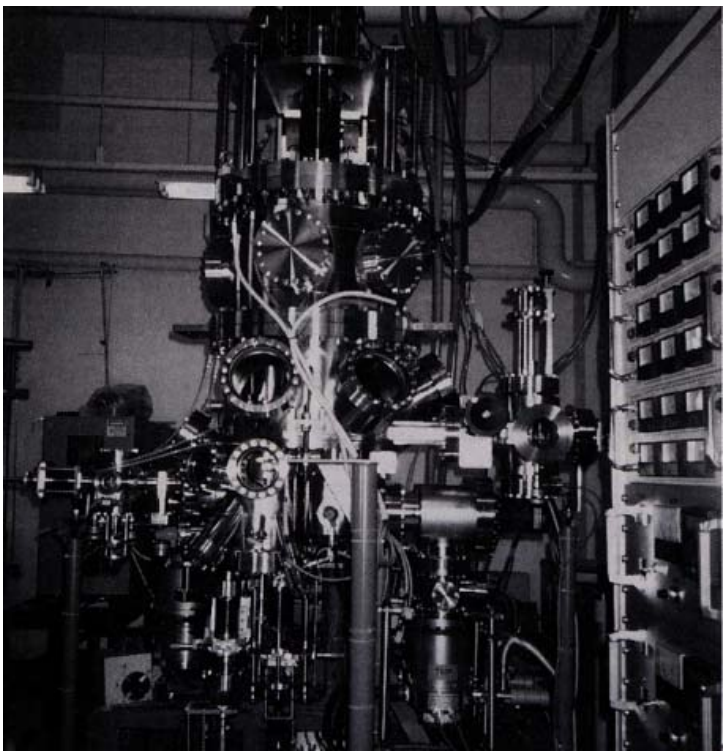

Fig. 2-1 Combinatorial laser MBE (CLMBE) apparatus.

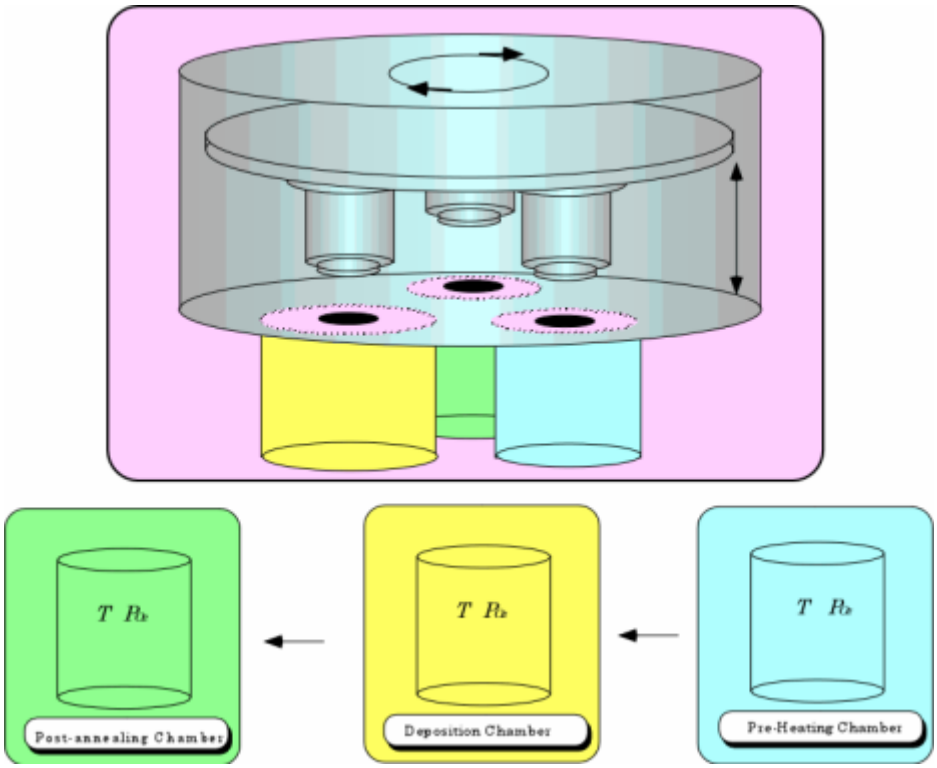

Fig. 2-2 Schematic drawing of the CLMBE apparatus.

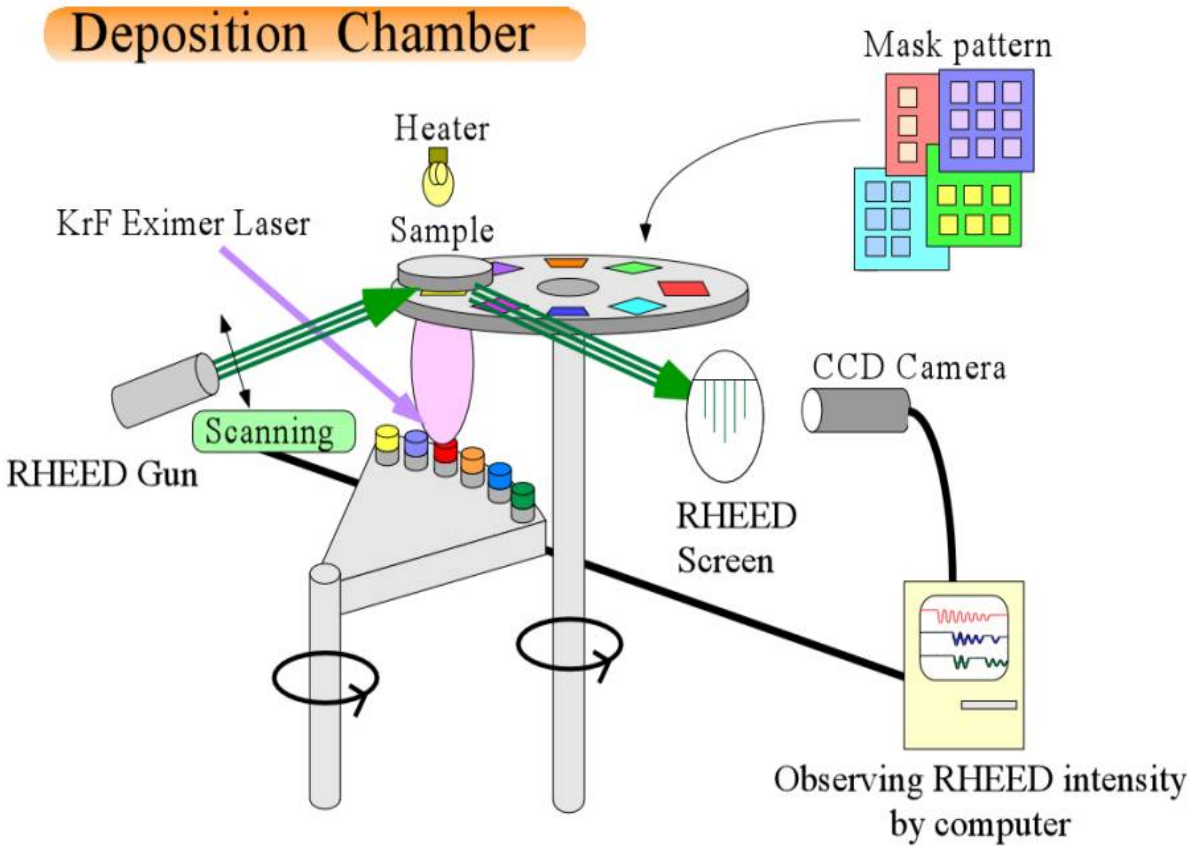

Fig. 2-3(a) Schematic drawing of Deposition chamber.

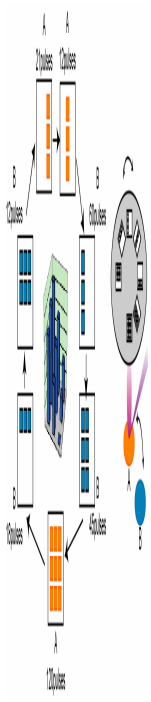

Fig. 2-3(b) A typical CLMBE procedure of 9 devided thin films fabrication on a substrate.

Scanning RHEED System

We can observe the surface morphology of thin films by in-situ scanning RHEEDsystem[3] [Fig.2-4]. During combinatorial synthesis, film growth has to be monitored systemically at several points on the substrate. A scanning RHEED system was developed for this purpose. The electron beam was scanned across the substrate surface by using a compensated deflection technique. The compensation was performed by two sets of magnetic coils to obtain parallel beam sweeping. The second coils bent back the electron beam by the same extent as the tilt generated by the first coils. The detection of the specula beam spot intensity was done by CCD camera facing at the RHEED screen.

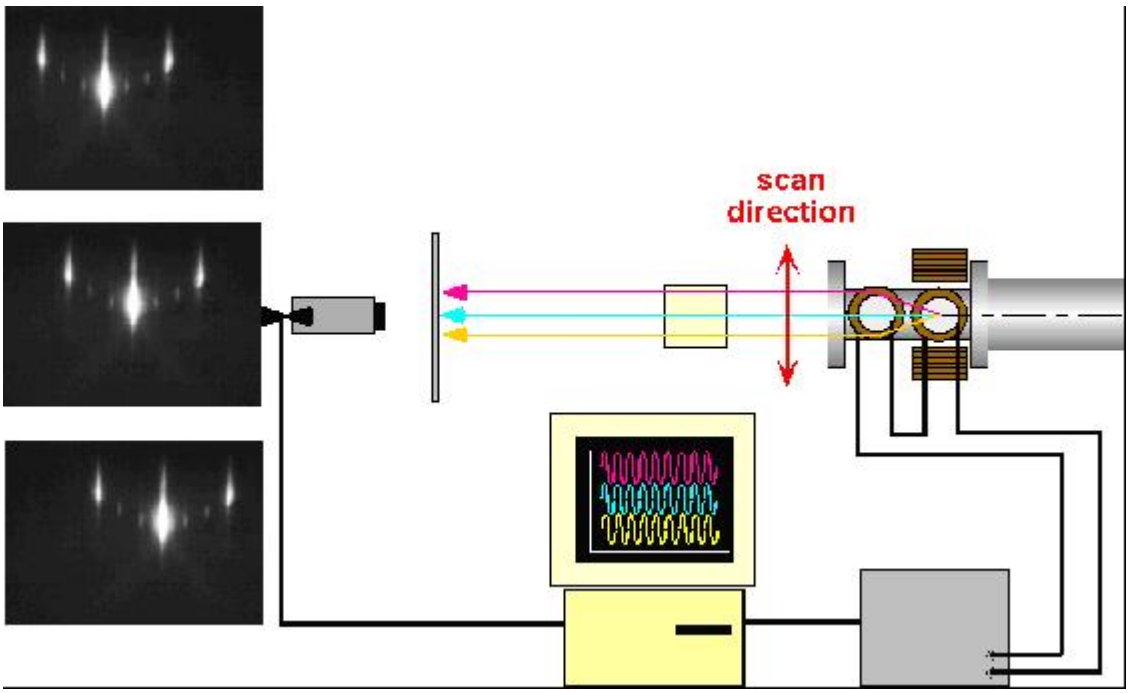

Fig. 2-4 Scanning RHEED system. Two sets of deflection coils enable parallel electron beam sweeping. Synchronization between the beam sweeping and image acquation is performed in software.

2-2 Combinatorial Films Fabrication Technique

2-2-1 Separated Combinatorial Libraries (3x3 pixels)

Giant CLMBE apparatus has round shape combinatorial mask plate between substrate and ceramics target 1-3 mm away from substrate surface. There are eight kinds of mask patterns and one pixel size is 3 x 3 mm^2 the distance between two pixels is 1 mm shown in Fig. 2-3(b). As a result, 3 x 3 mannered combinatorial library, with composition A and B is systematically controlled, can be fabricated on a single substrate through the process shown in

Fig. 2-3(b).

2-2-2 Compositional Spread Thin Films[4,5]

Combinatorial laser MBE are used for fabricating compositional spread films on a substrate. Schematic illustration is shown in Fig. 2-5. By using the moving mask system precisely controlled by stepping motors, the composition at each position is addressable. Two targets are switched synchronizing with the mask motion to deposit lower than one unit cell of the film during a period. Ceramic targets A and B are ablated by KrF excimer laser pulses alternately by switching the targets, while the moving masks were slid synchronously to give a linear gradient of x is $A_{1-x}B_x$.

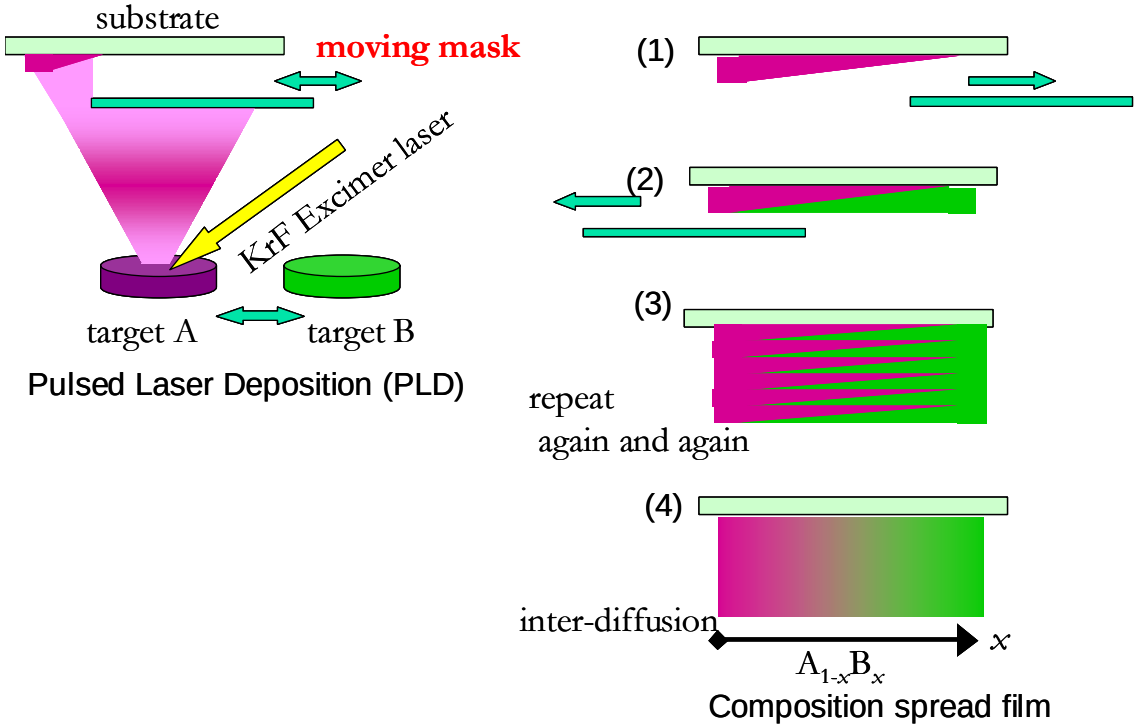

Fig. 2-5 Schematic illustration of compositional spread techniques

2-2-3 Temperature Gradient Films[6]

The temperature gradient over the film deposition surface was achieved by placing such a specially designed sample holder shown in Fig. 2-6 (a) and 2-6 (b). A continuous wave Nd:YAG laser beam is introduced through an optical lens to focus on the backside of the sample holder for heating the substrate. A 5 x 15 mm^2 substrate is attached to the substrate holder with platinum paste and clamps. A U-shaped cutout isolates the sample mounting area thermally from the frame of the sample holder. The Nd:YAG laser beam is focused in 3 mm

diameter to the free standing end of the sample holder while heat is lost mainly by the conduction through the other end attached to the main sample holder. A steady temperature gradient was achieved in this way, covering a rang of temperatures from about 600°C to 900°C over a distance of 11 mm. The temperature profile on the $SrTiO_3$ substrate was measured as depicted in Fig. 2-6(c) by scanning the optical pyrometer across the sample surface. The measurement spot size was about 2 mm.

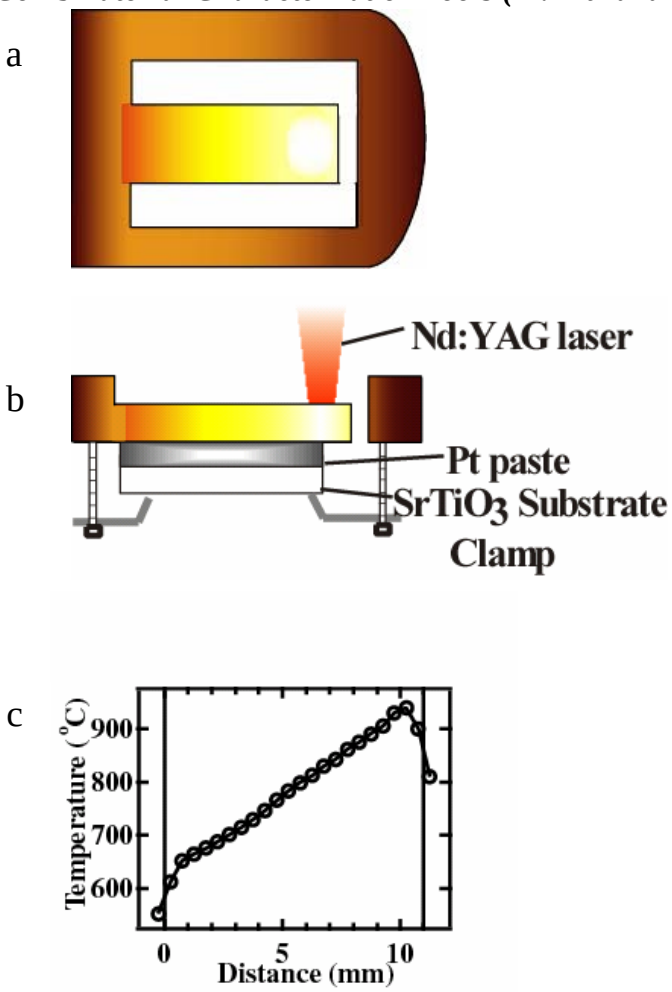

Fig. 2-6 Sample holders and temperature profiles: the top view (a) and side view (b) of the holder for temperature-gradient method and the temperature

2-3 Combinatorial Characterization Tools

2-3-1 Two Dimensional pH Imaging Apparatus[7,8]

Although combinatorial methods have recently been applied to the catalyst synthesis, catalyst discovery still involves inefficient one by one characterization techniques owing to the lack of techniques to screen the catalytic activity in combinatorial fashion. And TiO_2 catalysis appears to be impracticable. Towards this end, we have developed a new high throughput evaluation technique for the electrochemical catalysts.

Since most electrochemical processes involve the generation of pH distribution around the anode and cathode, a two-dimensional pH imaging can facilitate the evaluation of electrochemical reaction occurring on each pixel integrated in the combinatorial libraries. Fig.2-7 shows the measurement set up employed by us to generate the pH image pattern by using the scanning laser beam on the chemical imaging sensor. The sensor is made of semiconductor silicon covered with silicon nitride. The density of protons in the sample solution is locally sensed by the same mechanism as that of conventional potentiometric

electrodes such as pH field effect transistor.

The parallel evaluation of photo-catlytic activity in the combinatorial libraries was performed for the photo-decomposition of water in the presence of small amount of oxidizing or reducing agent by using the two-dimensional pH imaging apparatus described above. For example, in the presence of Fe^{3+} ions as oxidizing agent, a series of chemical reactions are expected to occur on the TiO_2 surface which can be summarized as:

$$2\,H_2O + 4\,Fe^{3+} \rightarrow 4Fe^{2+} + 4H^{+} + O_2 \uparrow$$

where the generation of H^+ should be accompanied with water decomposition.

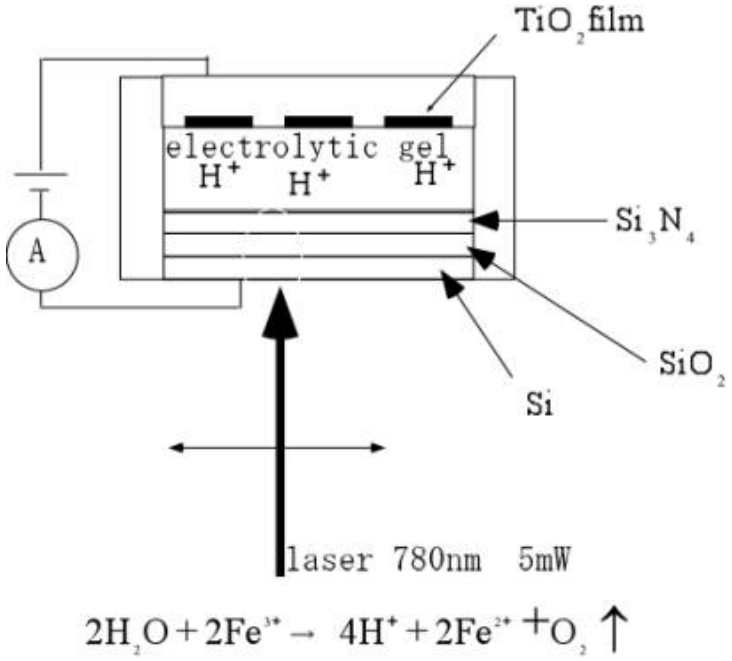

Fig. 2-7 Electrochemical cell and measurement setup of pH imaging apparatus

2-3-2 Scanning SQUID Prove Microscope

Several scanning probe microscopic techniques for studying local magnetic properties have been developed such as magnetic force microscope (MFM)[9], scanning Hall probe microscope (SHPM)[10], and scanning SQUID microscope (SSQM)[11]. These techniques have their own advantages: very high spatial resolution for MFM, high spatial reslution and broad range of the operating temperature and the applied and measured magnetic field for SHPM, and very high sensitivity to magentic field for SSQM. We have used a scanning SQUID microscope with a spatial resolution of ~10μm and a very high magnetic field sensitivity of ~10 nT operated from 3 to 100K. Schematic drawing of SSQM and photograph

of SQUID micro probe chip are shown in Fig. 2-8.

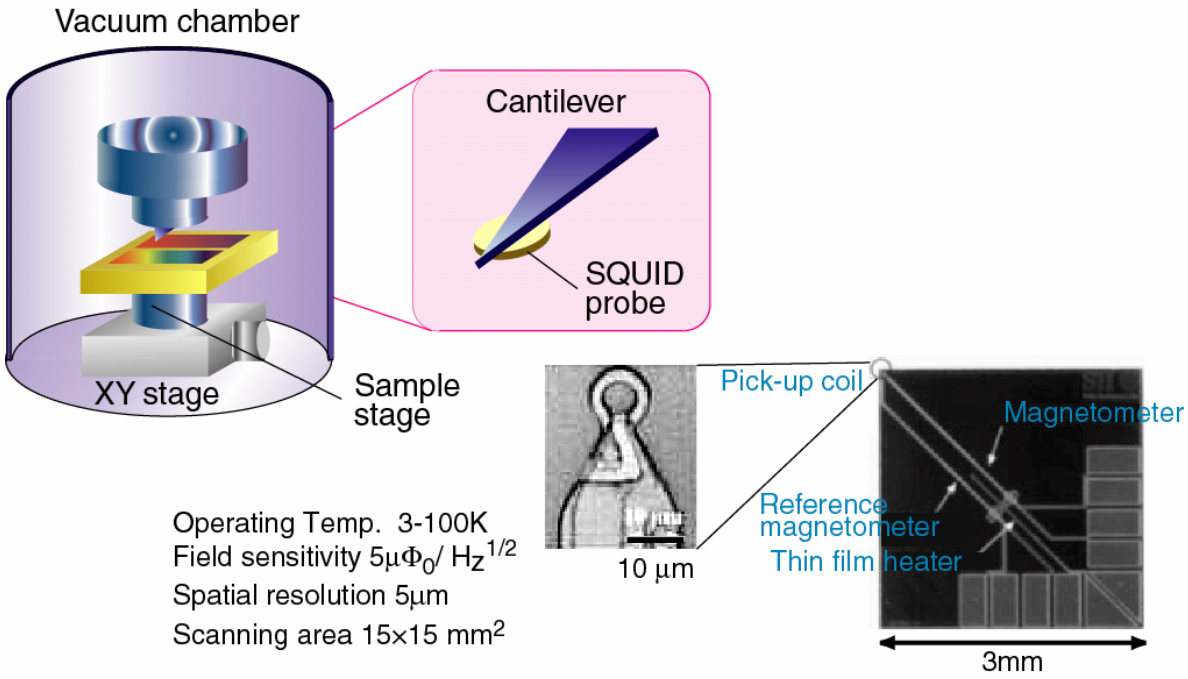

Fig. 2-8 Schematic diagram of scanning SQUID microscope (upper left) and photograph of Pick-up coil of SQUID probe.

2-3-3 Scanning Microwave Prove

Fig. 2-9 shows a schematic diagram of the LC lumped-constant resonator probe, where L and C_0 represent the inductance and the stray capacitance between the needle and the electric circuit of the probe, respectively. The free carrier frequency f_0 with the sample kept far away from the probe is given by

$$f_0 = \frac{1}{2\pi\sqrt{LC_0}} \tag{1}$$

When the tip contacts the sample surface, the carrier frequency shifts from f_0 to $f_0 + \Delta f_s$ due to the additional contribution of the capacitance between the needle and the ring (C_s):

$$f_0 + \Delta f_s = \frac{1}{2\pi\sqrt{L(C_0 + C_s)}} \tag{2}$$

Usually, C_s is much smaller than C_0, and thus the ration $\Delta f_s / f_0$ is approximated as

$$\frac{\Delta f_s}{f_0} = -\frac{1}{2}\frac{C_s}{C_0} \tag{3}$$

The capacitance Cs can be calculated explicitly using the image change method as

$$C_s = -4\pi\varepsilon_0 a\left(\frac{\ln(1-b)}{b}+1\right) \quad (4)$$

with

$$b = \frac{\varepsilon_r - 1}{\varepsilon_r + 1} \quad (5)$$

where a is the effective tip radius of the needle, and ε_r the relative dielectric constant of the sample, respectively. Substituting Eq. (4) into Eq. (3), we get

$$\frac{\Delta f_s}{f_0} = 2\pi\varepsilon_0 \frac{a}{C_0}\left(\frac{\ln(1-b)}{b}+1\right) \quad (6)$$

In Eq. (6), only the unknown parameter is the ratio al C_0, indicating that the dielectric constant of any sample can be determined if Δf_s is calibrated against one standard sample with know dielectric constant.

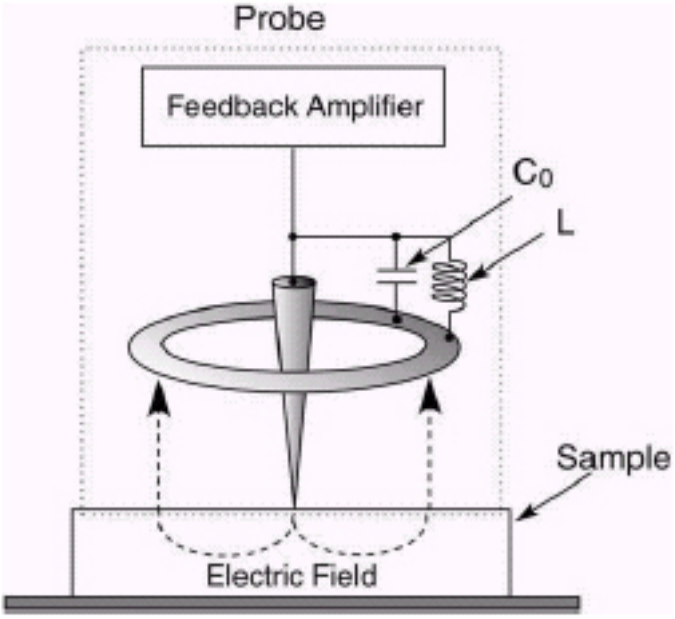

Fig. 2-9 Schematic diagram of the LC resonant probe

2-3-4 Combinatorial X-ray Diffraction (CXRD) Machine[12,13]

Figure 2-10 shows a schematic diagram of the CXRD. An x-ray beam with a diameter of about 100 μm is produced from rotating copper anode fine-focus x-ray generator (1.2kW). A Johan-type curved monochromator is used to eliminate Cu$K\alpha_2$, Cu$K\beta$, and white radiation and to focus Cu$K\alpha_1$ divergence beam into an area of ~10 mm x 100 μm on the sample surface with the convergence angle of 2°. The sample and CCD camera are mounted on the ω and 2θ stage of conventional two-circle goniometer, respectively. The diffracted beam is imaged on the CCD camera, where the two axes of image correspond to the position in the sample and 2θ angle. The spatial resolution of the image is limited by the diameter of x-ray beam for both axes in the present geometry. The measurement time varies from 5 seconds to a few minutes.

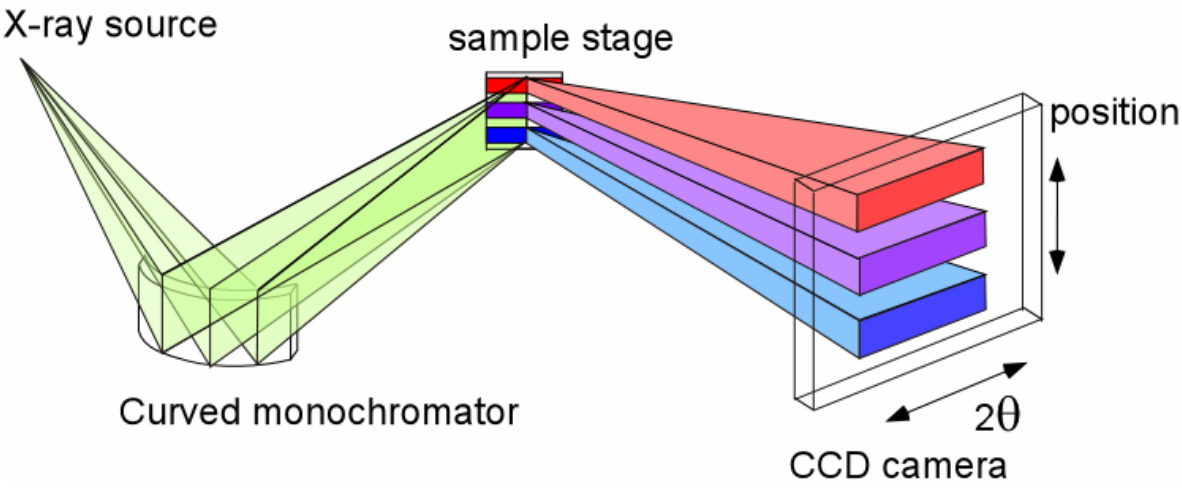

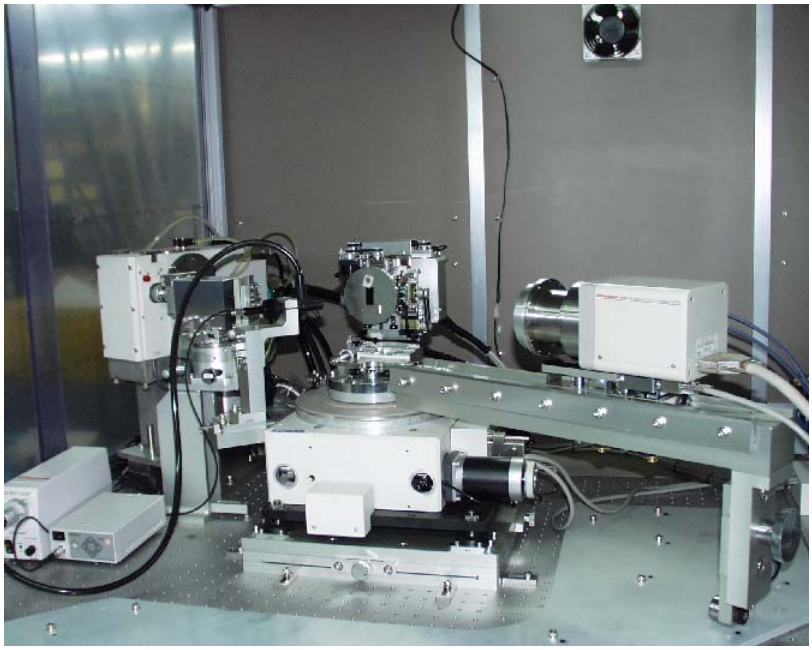

Fig. 2-10 (Color) Schematic diagram (top) and a photograph (bottom) of CXRD. The x-ray beam is focused by a Johan-type monochromator to form a convergent beam of; 10 mm x 100 μm with a convergence angle of 2° on the sample. The sample and the CCD camera for two-dimensional x-ray detector are mounted on the ω and 2θ stages of the two-circle goniometer, respectively. The diffracted beam is imaged on the CCD camera with axes of diffraction angle 2θ and position in the sample.

2-4 Demonstration of Combinatorial Synthesis (Mg doped ZnO and Y_2O_3: Eu)

In order to confirm the feasibility of Giant CLMBE apparatus, we fabricated and characterized Mg doped ZnO and Eu doped Y_2O_3 (Y_2O_3: Eu) combinatorial thin films

ZnO

ZnO has a wide and direct bandgap of 3.37 eV at room temperature and wurtzite crystal structure. ZnO has attracted considerable attention for the application as ultraviolet light emitting devices (LEDs) and laser diodes (LDs). Room temperature lasing was demonstrated by our group upon optical pumping from ZnO thin films grown on sapphire substrate by laser molecular beam epitaxy (L-MBE)[14]. Hence band gap engineering of ZnO is an interesting and important part of fabricating a ZnO-based laser diode. Mg doped ZnO oxide thin films were already reported by our laboratory for controlling the band-gap.

Y_2O_3: Eu

Trivalent rare-earth ion doped oxides are the most promising phosphors for flat panel displays (FPD's) applications[15]. In contrast to sulfur-based materials, oxides do not contaminate the electron emitters in field emission displays and are chemically inert to plasmas commonly used in plasma-operated FPD's. Europium-doped mono-crystalline yttrium oxide (Y_2O_3:Eu) was firstly proposed in 1964 for solid state laser applications due to the sharp emission (λ = 611 nm) of the europium ion activator (Eu^{3+}) in the host lattice (Y_2O_3). Subsequent applications of this material as powders were found in cathode ray tubes (CRT's) and fluorescent lamps.

2-4-1 Characterization of $Mg_xZn_{1-x}O$ Thin Films.

To demonstrate the previous result, we have applied the CLMBE technique to the fabrication of highly Mg-doped ZnO thin films. Characterization of Mg doped combinatorial libraries was carried out by X-ray diffraction (MXP18HF[22]), UV transmittance measurements, and Mg contents were determined by Rutherford back scattering (RBS). General CLMBE process is shown in Fig. 2-3 (b). It is sketched for the case of the fabrication of Mg doped ZnO combinatorial libraries. The process was achieved by combining mask patterns and targets in an automatic way controlled by a local computer. As a result, nine different ZnO films having different Mg contents were fabricated on a single substrate by mixing Mg 10 mol% doped ZnO ($Mg_{0.1}Zn_{0.9}O$) and pure ZnO (99.999% purity) in one unit cell. Laser

ablation pulses ratio was easily achieved for each ceramic target. The targets were 70mm away from the substrate and ablated by KrF excimer laser pulses (248 nm, 5Hz, 30ns) with a fluence of 3 J/cm^2. Oxygen partial pressure was kept at 1 x 10^{-6} Torr during the deposition and typical deposition rate was about 0.002 nm/pulse. Nine pixels, of which the doping concentrations were different from 0 to 20 mol%, were obtained by this process. Because enrichment factor is about 2 in the case of Mg doped ZnO will be discussed in Chapter 4.

It was known that when Mg 10 mol% doped ZnO target was ablated at 600℃, Mg contents in the fabricated thin films were nearly 20 mol%, in which enrichment factor is estimated to be around 2. This enrichment factor will be discussed in follow section 4-2-2. Designed Mg contents were 1～15% by our process. From XRD patterns, all combinatorial pixels showed single wurzite phase in spite of the excess of Mg contents compared to phase diagram. Fig. 2-11 shows the calculated *c*-axis length from XRD measurements and band-gap energy estimated from ultraviolet/visible light transmittance spectra as a function of Mg contents. It is clearly observed that c-axis length was shortened and band gap energy was increased with increased Mg contents (●). As a comparison, the data obtained from conventional one by one experiments (□) is also plotted in these figures. Some of conventional data (□) were deviated from the fitting line of combinatorial data (●). It is considered that combinatorial thin films were fabricated in the same conditions, such as substrate temperature, atmosphere pressure. When fabricating thin films, there is a little changes in conditions, more or less, because it is very difficult to keep the conditions the same for all nine films.

It can be concluded that the CLMBE technique provides not only high-throughput synthesis and screening of new materials but can also be used to reduce statistical errors in experiments where the dependence of material properties on film composition or decomposition conditions is studied. The greatest advantage of the L-MBE technique is its ability to stabilize kinetically controlled phases which would not exist under thermodynamic equilibrium conditions. We can demonstrate the capability of the CLMBE technique through fabrication and characterization of Mg doped ZnO combinatorial thin films.

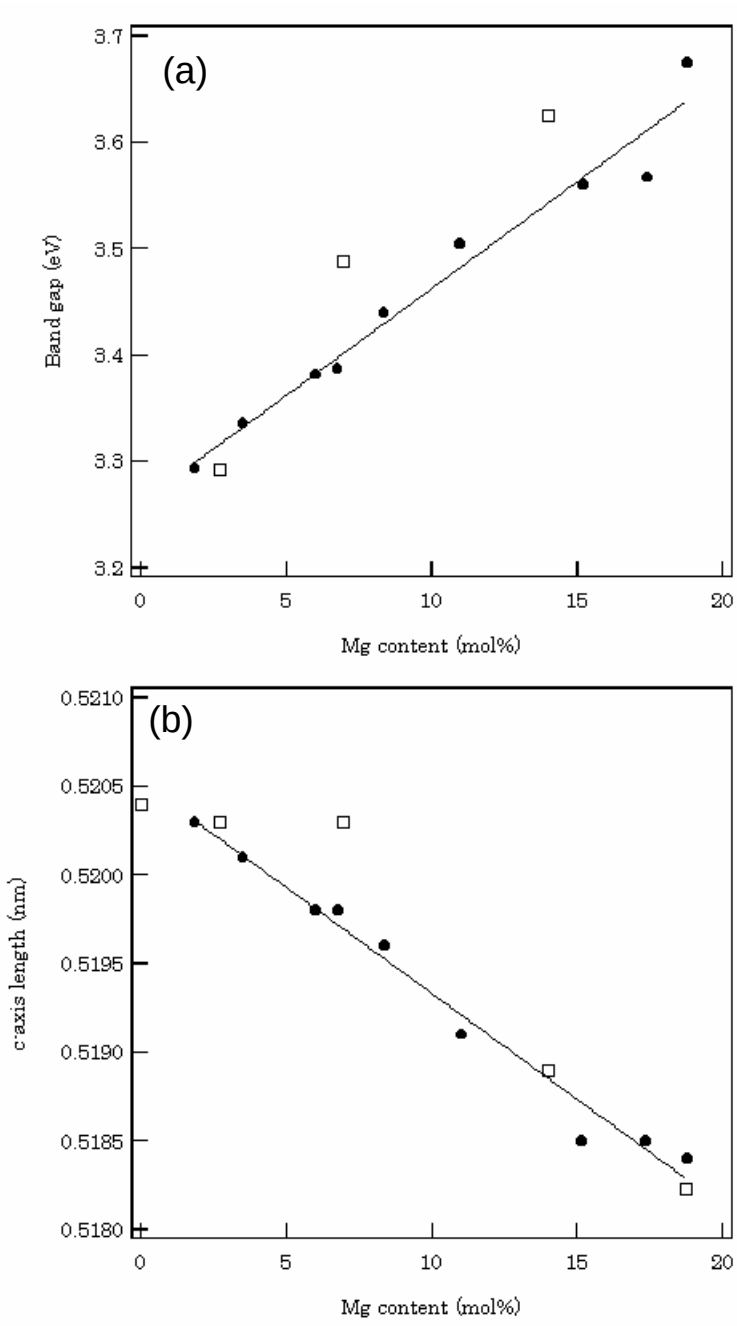

Fig. 2-11 The band gap (a) and *c*- axis length (b) dependence on the Mg doping.

● and □ are obtained for a combinatorial and conventional manner, respectively.

2-4-2 Characterization of Y_2O_3: Eu Thin Films

We fabricated Y_2O_3: Eu combinatorial thin films on $SrTiO_3$ (STO) (001) substrate under P_{O2} =1×10^{-6} Torr oxygen pressure and T_S = 800℃. Nine different Y_2O_3 films having different Eu contents were fabricated on a single substrate by mixing Eu 50 mol% doped Y_2O_3 and pure Y_2O_3 ceramic target ablated by KrF excimer laser (λ = 248 nm). Laser fluence and repetition rate was 3 J/cm^2 and 10HZ. Designed europium dopant concentration was from 0～20 mol%. XRD pattern [Fig. 2-12 (a)] and RHEED pattern [Fig. 2-12 (b)] show epitaxially growth of deposited Y_2O_3 thin films on STO (001) substrate. Fig.2-13 (a) shows in-situ observation of fluorescence from Y_2O_3: Eu combinatorial thin films, which was achieved by hitting electron beam to the sample surface. It was clearly observed that fluorescent is from Y_2O_3: Eu instead of non-doped Y_2O_3 sample. A *c*-axis length determined by XRD is increasing with increasing europium dopant concentration as shown in Fig. 2-13 (b). It is thought from the fact that ion-radius of europium is larger than that of yttrium. From these results, it can be considered that Eu atom will substitute for Y atom.

Then, we studied cathode luminescence of Y_2O_3: Eu films. The electron beam energy was 5 *k*V. Fig. 2-14 shows brightness and peak intensity of luminescence at 609 nm calibrated film thickness were plotted with designed Eu doped concentration. Peak maximum was clearly observed around Eu 5 mol%, it follows previous bulk data of Y_2O_3: Eu. It can be considered that at low Eu concentration, Eu acts luminescence center but extra Eu will act as trap-center.

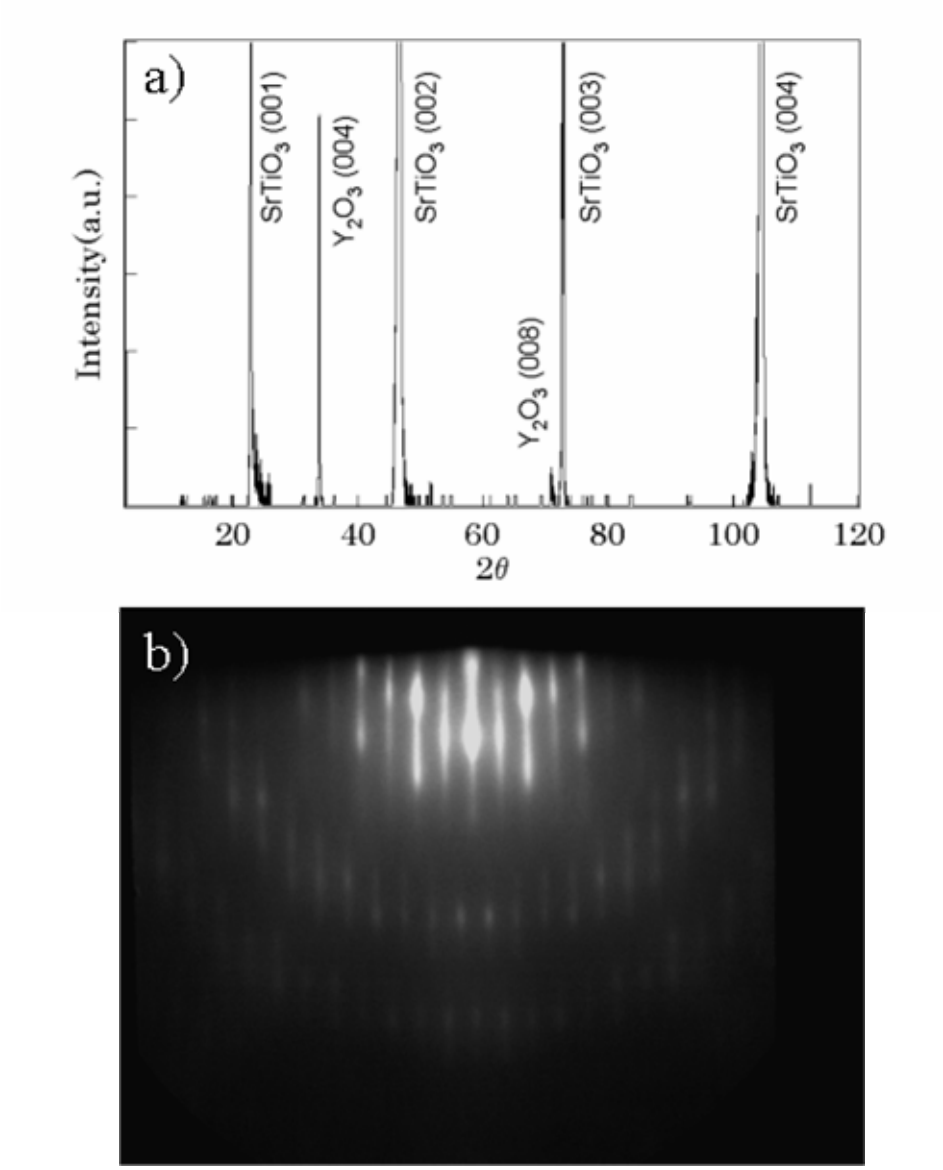

Fig. 2-12 XRD pattern (a) and RHEED pattern (b) of Y_2O_3 thin film deposited on $SrTiO_3$ (001) in $Po_2=10^{-6}$ at Ts=800°C.

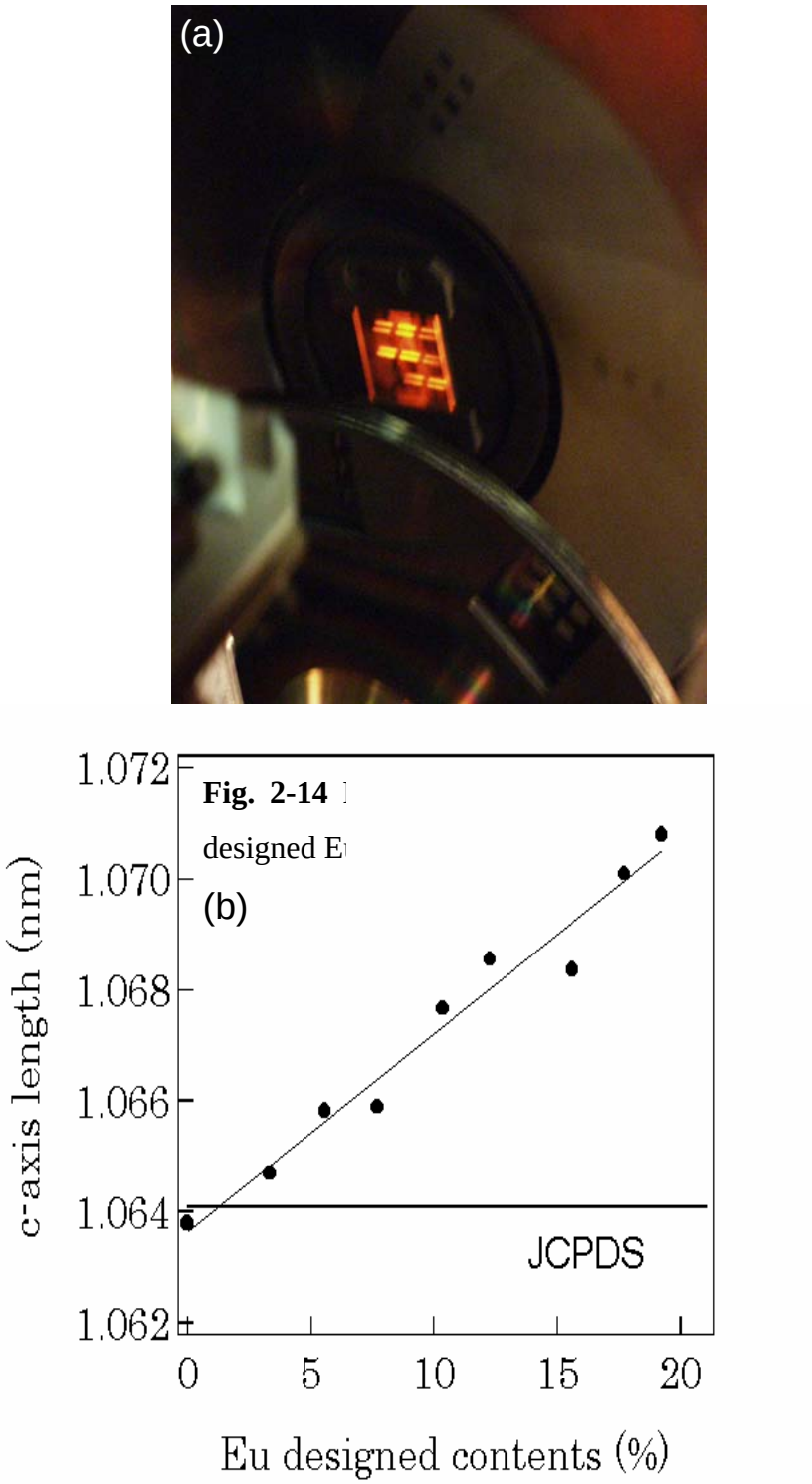

Fig. 2-13 In-situ observation of fluorescence (a) and *c*-axis length changing (b) in Y_2O_3: Eu combinatorial thin films fabricated on $SrTiO_3$.

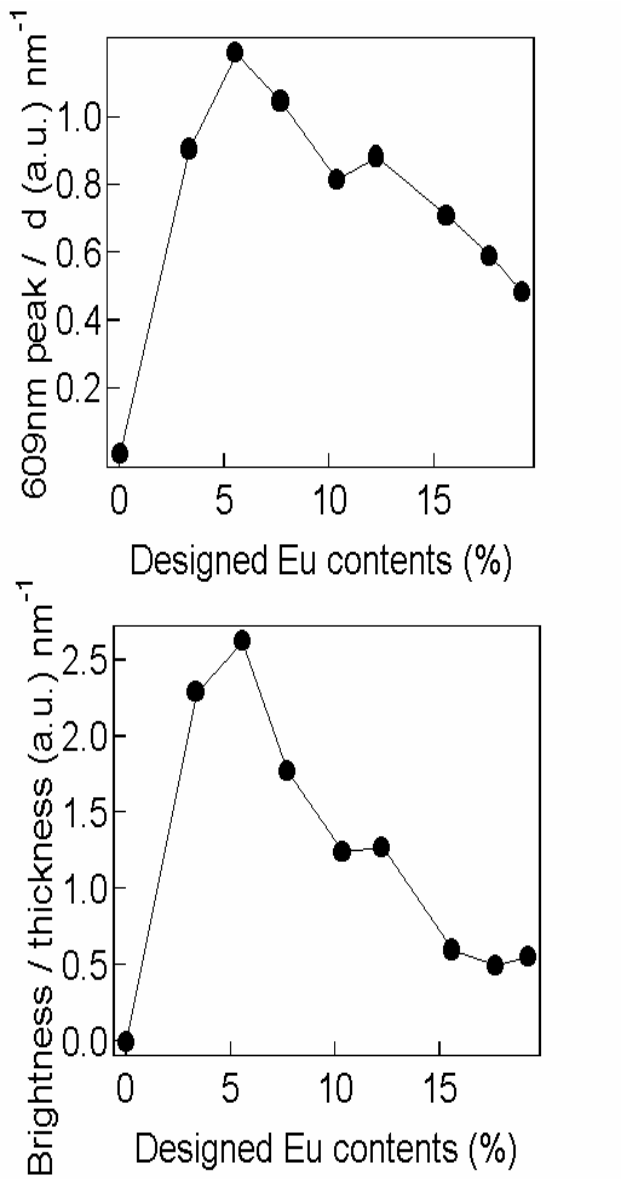

Fig. 2-14 Peak intensity at 609nm (a), Brightness (b) calibrated by film thickness vs. designed Eu contents of Y_2O_3: Eu thin films

(b)

2-5 Conclusion

Development of CLMBE apparatus was carried out with Mg doped ZnO and Eu doped Y_2O_3 systems. First, ZnO combinatorial samples doped with Mg were discussed. The bandgap is increasing and *c* - axis length is shortening quite linearly with increasing Mg content in the films. It can be concluded that the CLMBE technique provides not only high-throughput synthesis and screening, but can also be used to reduce statistical errors in experiments when the dependence of material properties on film composition or deposition conditions is studied. Eu doped Y_2O_3 combinatorial thin films are also fabricated for the demonstration of CLMEB apparatus. It was clearly obtained that luminescence intensity calibrated by film thickness from Y_2O_3: Eu has a maximum peak around designed 5 mol% of Eu concentration. Brightness calibrated by film thickness has also a maximum peak around 5 mol%. These results agree with previous reports. These results were obtained by one fabrication run and one observation run. Through these results we succeeded in proofing that CLMBE technique is an excellent methods to development material science.

And another combinatorial techniques and combinatorial characterizations were discussed. These techniques are expected to improve material science faster.

Reference

[1] X. D. Xiang, X. Sun, G. Briceno, Y. Lou, K. -A. Wang, H. Chang, W. G. Wallace-Freedman, S. -W. Chen and P. G. Schltz: Science **268** (1995) 1738

[2] Y. Matsumoto, Makoto Murakami, Z.W. Jin, A. Ohtomo, M. Lippmaa, M. Kawasaki, H. Koinuma; Jpn. J. Appl. Phys. **38** L603-L605 (1999)

[3] H. Koinuma, T. Koida, T. Ohnishi, D. Komiyama, M. Lippmaa, M. Kawasaki: Appl. Phys. A **69**, S29-S31 (1999)

[4] T. Fukumura, Y. Okimoto, M. Ohtani, T. Kageyama, T. Koida, M. Kawasaki, T. Hasegawa, Y. Tokura, H. Koinuma: Appl. Surf. Sci. **189** (2002) 339-343

[5] T. Fukumura, M. Ohtani, M. Kawasaki, Y. Okimoto, Y. Tokura, H. Koinuma: Appl. Phys. Lett. **77** 3426-3428 (2000)

[6] T. Koida, D. Komiyama, H. Koinuma, M. Ohtani, M. Lippmaa, M. Kawasaki: Appl Phys. Lett. **80** 565-567 (2002)

[7] Y. Matsumoto, M. Murakami, Z.W. Jin, A. Nakayama, T. Yamaguchi, T. Ohmori, E. Suzuki, S. Nomura, M. Kawasaki, H. Koinuma; Proc. SPIE **3941** 19-27 (2000)

[8] A. Nakayama, E. Suzuki, T. Ohmori; Appl. Surf. Sci. **189** (2002) 260-264

[9] Y. Martin, D. Rugar, H.K. Wickramasinghe, Appl. Phys. Lett. 52 (1988) 244.

[10] A.M. Chang, H.D. Hallen, L. Harriot, H.F. Hess, H.L Loa, J. Kao, R.E. Miller, T.Y. Chang, Appl. Phys. Lett. 61 (1992) 1974.

[11] L.N. Vu, M.S. Wistrom, D.J. Van Harlingen, Appl. Phys. Lett. 63 (1993) 1693.

[12] M. Ohtani, T. Fukumura, M. Kawasaki, K. Omote, T. Kikuchi, J. Harada, A. Ohtomo, M. Lippmaa, T. Ohnishi, D. Komiyama, R. Takahashi, Y. Matsumoto and H. Koinuma; Appl. Phys. Lett. **79** 3594-3596 (2001)

[13] M. Ohtani, T. Fukumura, M. Kawasaki, K. Omote, T. Kikuchi, J. Harada and H. Koinuma; Appl. Phys. Lett. **80** 2066-2068 (2002)

[14] Y. Segawa, A. Ohtomo, M. Kawasaki, H. Koinuma, Z. K. Tang, P. Yu and G. K. L. Wong: Phys. Status Solidi **202** (1997) 669.

[15] G. A. Hirata, J. Mckittrick, M. Avalos-Borja, J. M. Siqueiros, D. Delvin: Appl. Surface Sci. **113/114** (1997) 509

Chapter 3 Structural Control of Titanium Dioxide, and Optical Characterization of High Quality Anatase Thin Films

3-1 Introduction

Titanium dioxide, TiO_2, attracts much attention in recent years because of its unique physical and chemical properties, such as high refractive index, excellent optical transmittance in the visible and near-infrared regions, high dielectric constant and photo catalysis for water cleavage[1]. Particularly, a lot of studies about as a photo-catalyst have been done. And also have been studied about single TiO_2 crystal for applying such as optical-isolator. However, there are a few researches as a semiconductor. In ZnO case, ZnO has been widely studied as white pigments, catalyst, varistor and phosphor. Recently, our group tried to fabricate high-quality ZnO by laser molecular beam epitaxy (MBE), room temperature lasing was demonstrated upon optical pumping from ZnO thin films grown on sapphire substrate Fine system, by using single crystal and so on, is useful way to study about photo-catalytic properties as succeeded in metal catalyst. There were few studies about TiO2 as a semiconductor. From these points of view, I tried to fabricate single crystal TiO_2 thin films, as succeeded in ZnO, with combinatorial laser MBE as discussed in Chapter 2.

Crystal structure control of TiO_2 is shown in section 3-2, and further studies about fabrication of rutile/anatase bilayer films, which have different thermo-dynamical stability, with this technique shown in section 3-3. Lastly, structural characterization and optical properties of anatase thin films with high-crystallinity on $LaAlO_3$ (001) single crystal, which has closed lattice matching with anatase structure are discussing in section 3-4.

Table 3-1 Typical property of TiO_2

crystal structure	Rutile	Anatase	brookite
crystal sytem	tetragonal	tetragonal	orthorhombic
space group	P42/mnm (no.136)	I41/amd (no.141)	Pcab (no.61)
Lattice constant			
a （Å）	4.5933	3.7852	5.4558
b （Å）			9.1819
c （Å）	2.9592	9.5139	5.1429
refractive index	nw=2.6124	nw=2.5612	na=2.5831
(at 589.3nm, 25℃)	ne=2.8993	ne=2.4880	nb=2.5843
			nr=2.7004
dielectric constant	e=110～117	e=48	e=78
density (g/ml)	4.27	3.9	4.13
melting point (℃)	1855	trans to rutile structure	trans to rutile structure
Band gap (eV)	3.05 (indirect)	3.20 (indirect)	

Table 3-2 Lattice matching between TiO_2 thin films and various oxide substrates

Anatase type

Crystal structure Tetragonal (I41/amd no.141)

Lattice constant a = 3.7852 Å c = 9.5139Å

Substrate	Lattice Constant	Mismatch with anatase
$SrTiO_3$	3.91Å	3.2%
$LaAlO_3$	3.79 Å	-0.2%
$LaSrAlO_4$	3.76 Å	-0.8%

Rutile type

Crystal structure Tetragonal (P42/mmm no. 136)

Lattice constant a = 4.5933 Å c = 2.9592 Å

Substrate	Lattice constant	Orientation	Lattice constant	Lattice mismatch
Al_2O_3 $(1\bar{1}02)$		Rutile(101)		
$[\bar{1}\bar{1}20]$	4.76 (Å)	[010]	4.59 (Å)	-3.57%
$[\bar{1}101]$	5.13 (Å)	$[10\bar{1}]$	5.46 (Å)	6.43%
Al_2O_3 (0001)		Rutile (100)		
$[10\bar{1}0]$	2.74 (Å)	[001]	2.96 (Å)	8.03%
$[\bar{1}\bar{2}10]$	4.76 (Å)	$[0\bar{1}0]$	4.59 (Å)	-3.59%

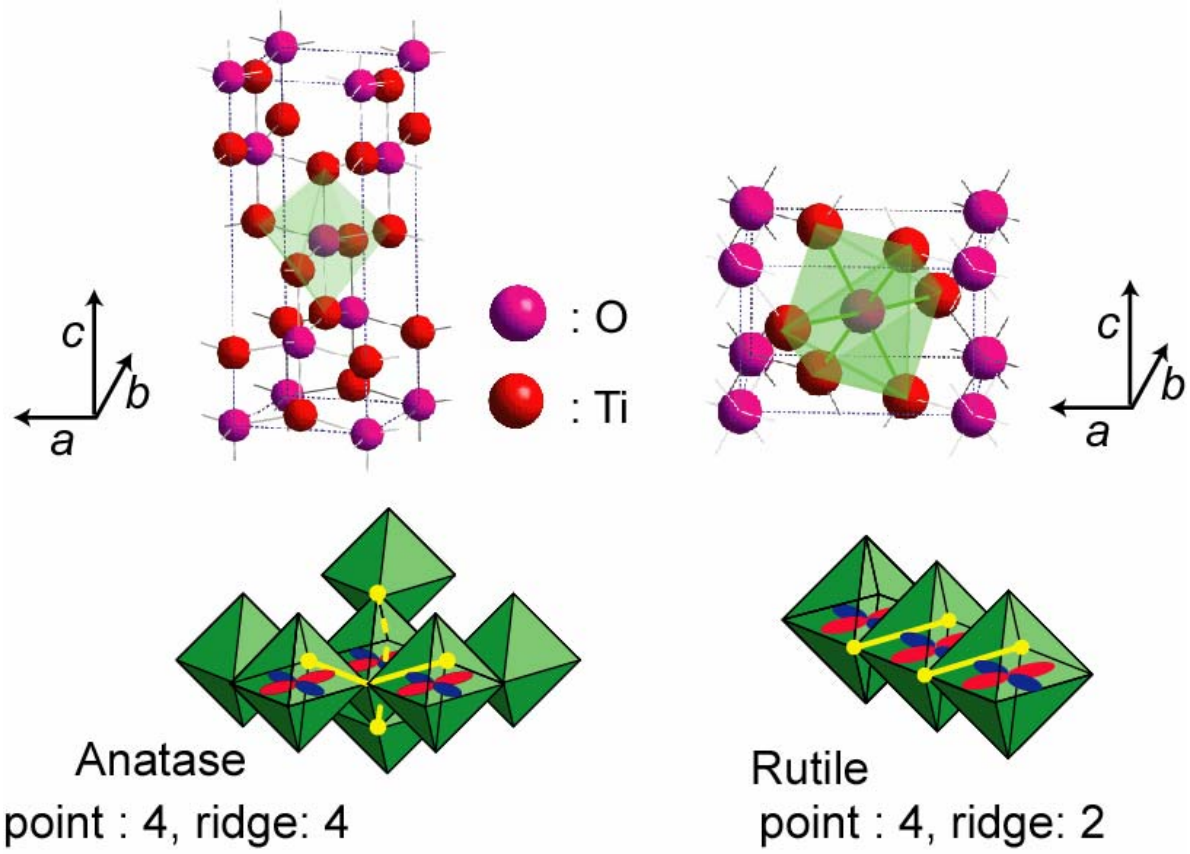

Fig. 3-1 (a) Anatase and (b) Rutile crystal structures. Local structures are very similar in each other. Octahedral bonding of anatase is 4 point and 4 ridge, and that of rutile is 4 point and 2 ridge.

3-2 Structural Control of Titanium Dioxide

TiO_2 has three crystal structures, rutile, anatase and brookite. Rutile has been the subject of many experimental and theoretical investigations, because it is the most thermodynamically stable, well-defined, and commercially available crystal phase. However anatase is more attractive as a photocatalyst,[2] and extensive studies have been made to obtain thin film anatase single crystals.[3,4,5,6] Some physical properties, such as refractive index, dielectric constant and optical band gap are different [table 3-1]. From these points of view, structural control of TiO_2 is one of the most important technologies for investigation of TiO_2. Actually, there have been reported about structural control of TiO_2[7,8].

Structural control of titanium dioxide, TiO_2, thin films was achieved by the selection of appropriate substrates. The crystal structures of anatase and rutile are shown in Fig. 3-1. Ti ions have octahedral coordination in these structures. The both phases have structural similarity that TiO_6 octahedrons share the edges. The lattice match between TiO_2 thin films and various substrates are

shown in table 3-2.

Fabrication of TiO_2 thin films was achieved by the CLMBE method shown in chapter 2. TiO_2 ceramics targets (99.99% purity) were ablated by KrF excimer laser (λ = 248 nm). *r*- and *c*-Al_2O_3 substrates were used to fabricate rutile thin films. And $SrTiO_3$ (STO) (001), $LaAlO_3$(LAO) (001), $LaSrAlO_4$ (LSAO) (001), $YAlO_3$ (YAO) (001) substrates were selected to fabricate anatase thin films.

3-2-1 (100) oriented rutile type TiO_2 thin films on Al_2O_3 (0001) (*c*- Al_2O_3) substrate

Fabrication of (100) oriented rutile films were used CLMBE method. Laser fluence and repetition rate were 3 J/cm^2 and 5 Hz, respectively. Oxygen partial pressure (P_{O2}) and substrate temperature (T_S) were kept at P_{O2} = 1 x 10^{-6} Torr and T_S = 550°C - 750°C during the deposition, and typical deposition rate was 0.002 nm/pulse (0.01 nm/s). The typical XRD pattern and RHEED pattern deposited at Ts = 750°C are shown in Fig. 3-2. It is found that (100) oriented TiO_2 (R) thin films were grown on *c*-Al_2O_3 at 750°C. On the other hand, when temperature is lower than 650°C, orientation of thin films was (210), not (100) direction.

Hetero-epitaxy of TiO_2 on *c*-Al_2O_3 becomes understandable by examining the atomic arrangement of the relevant epitaxy surfaces. The *c*-Al_2O_3 surface contains oxygen atoms that exhibit three fold symmetry (Fig. 3-3 (b)), and represent the template onto which the rutile phase is deposited. In the projection of $(100)_{rutile}$ [Fig. 3-3 (a)], one unit cell is marked out by a solid line. If rutile grows as single crystal over Al_2O_3 (0001), then the best structural match is $[001]_{rutile} \parallel [10\bar{1}0]Al_2O_3$, resulting in a directional mismatch of +8.03% along the $[001]_{rutile}$ and -3.59% along the $[010]_{rutile}$. The rutile film takes on a mosaic structure consisting of three equivalent domains and it would be consistent with an epitaxy structure in which TiO_2 unit cells are described on the Al_2O_3 (0001) surface such that the match along $[010]_{rutile}$ is maximized, while that along $[001]_{rutile}$ is minimized. Schematically, this relationship is

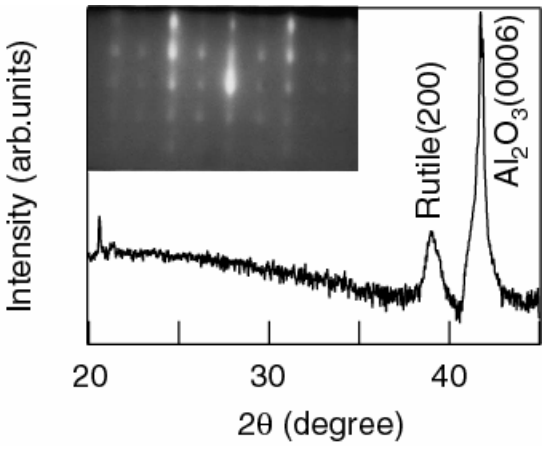

Fig. 3-2 Typical XRD pattern of (100) oriented rutile thin films fabricated on Al_2O_3 (0001) substrate. RHEED image of after deposited is also shown in the inset.

illustrated by the three equivalent TiO_2 unit cells rotating 120° from each other, as marked in dotted lines by the middle of Fig. 3-3 (b). In short, [$10\bar{1}0$] Al_2O_3 is collinear with < [001], [$0\bar{1}$ 1] and [011] > rutile.

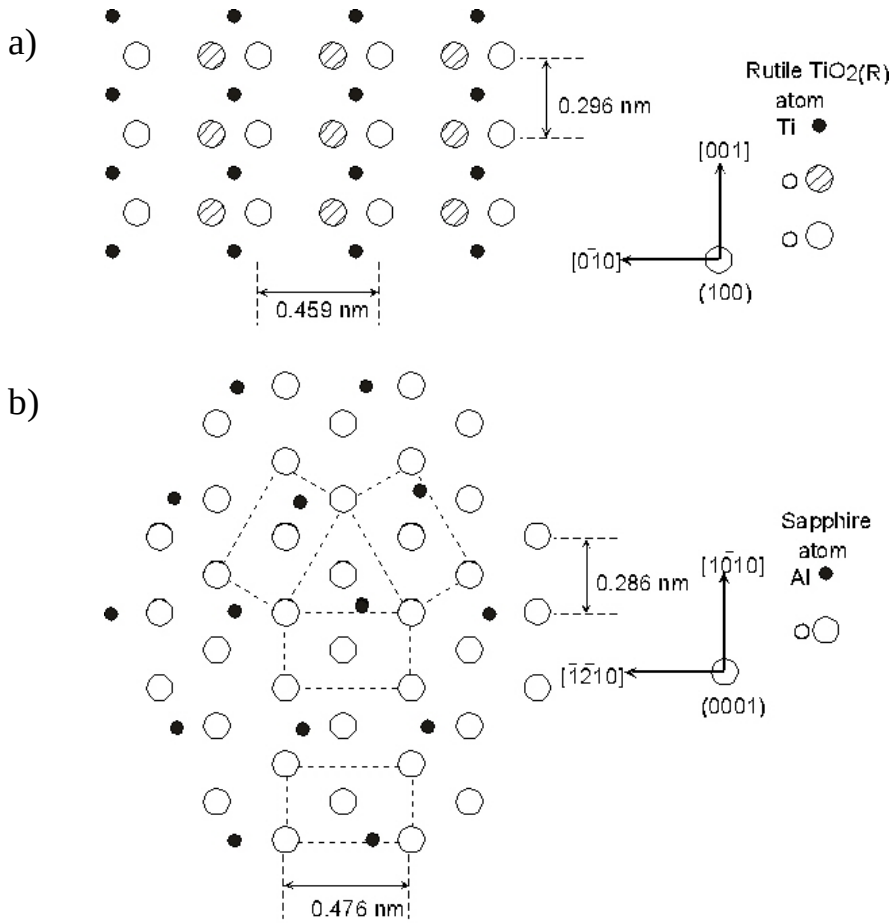

Fig. 3-3 Schematic drawing of the film and substrate planar atomic arrangements to illustrate the threefold symmetric mosaic structure of rutile (100) on Al_2O_3 (0001).

3-2-2 (101) oriented rutile type TiO_2 thin films on Al_2O_3 ($10\bar{1}2$) (*r*- Al_2O_3) substrate.

Fabrication of (101) oriented rutile thin films was achieved by CLMBE method. Laser fluence and repetition rate were 3 J/cm^2 and 5 Hz, respectively. Oxygen partial pressure (P_{O2}) and substrate temperature (Ts) were kept at $P_{O2} = 1\times10^{-6}$ Torr and Ts = 750°C during the deposition, and typical deposition rate was 0.002 nm/pulse(0.01 nm/s). The typical XRD pattern and RHEED pattern are shown in Fig. 3-4. It is found that (101) oriented TiO_2 (R) thin films were grown on Al_2O_3 ($10\bar{1}2$) (*r*- Al_2O_3) at 750°C.

An understanding of this heteroepitaxy is obtained by examining the atomic arrangement of the $(101)_{rutile}$ and ($1\bar{1}02$) Al_2O_3 planes (Fig. 3-5)[6]. When hexagonally indexed, $A1_2O_3$ has a unit cell with *a* = 4.758 and *c* = 12.991 Å, while rutile is of tetragonal symmetry with *a* = 4.593 and *c* = 2.959 Å. In the $A1_2O_3$ corundum structure the oxygen atoms are arranged approximately in a close-packed arrangement with two-thirds of the octahedral holes filled by Al atoms. The ($1\bar{1}02$) Al_2O_3 surface contains oxygen atoms that exhibit twofold symmetry [Fig. 3-5(b)] and represent the "template" structure for the deposition of the twofold symmetrical $(101)_{rutile}$. In the projection of $(10l)_{rutile}$ [Fig. 3-5(a)],

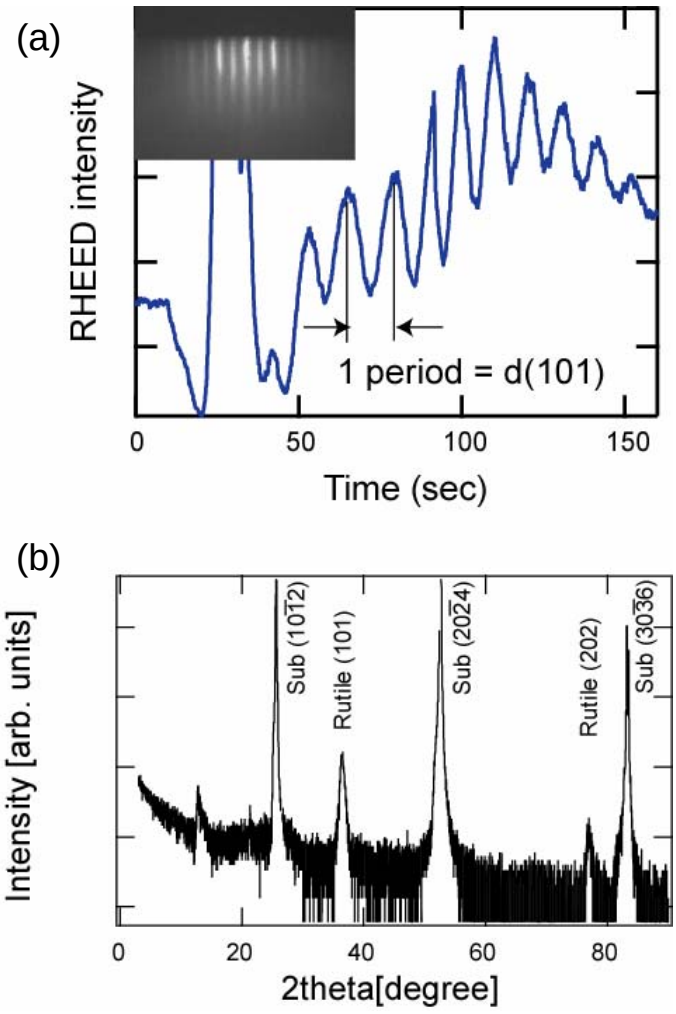

Fig. 3-4 (a) The specular beam intensity in the RHEED pattern vs time during the deposition of TiO_2. Inset image is the RHEED pattern in the film. (b) XRD pattern of 5 mol% Co doped TiO_2 thin film deposited on *a*-Al_2O_3 ($1\bar{1}02$) single crystal substrate.

a reduced unit cell bound by [010] and [101] is indicated by a solid line. For rutile to grow laterally as a collection of this unit cell over $(1\bar{1}02)Al_2O_3$, the best structural match would be to position the TiO_2 structure such that $[010]_{rutile} \parallel [\bar{1}\bar{1}02]Al_2O_3$, in which the directional mismatch becomes -3.57% along $[010]_{rutile}$, and 6.43% along $[10l]_{rutile}$. Schematically, this is indicated by the dashed outline of the reduced TiO_2 unit cell on the $A1_2O_3$ plane.

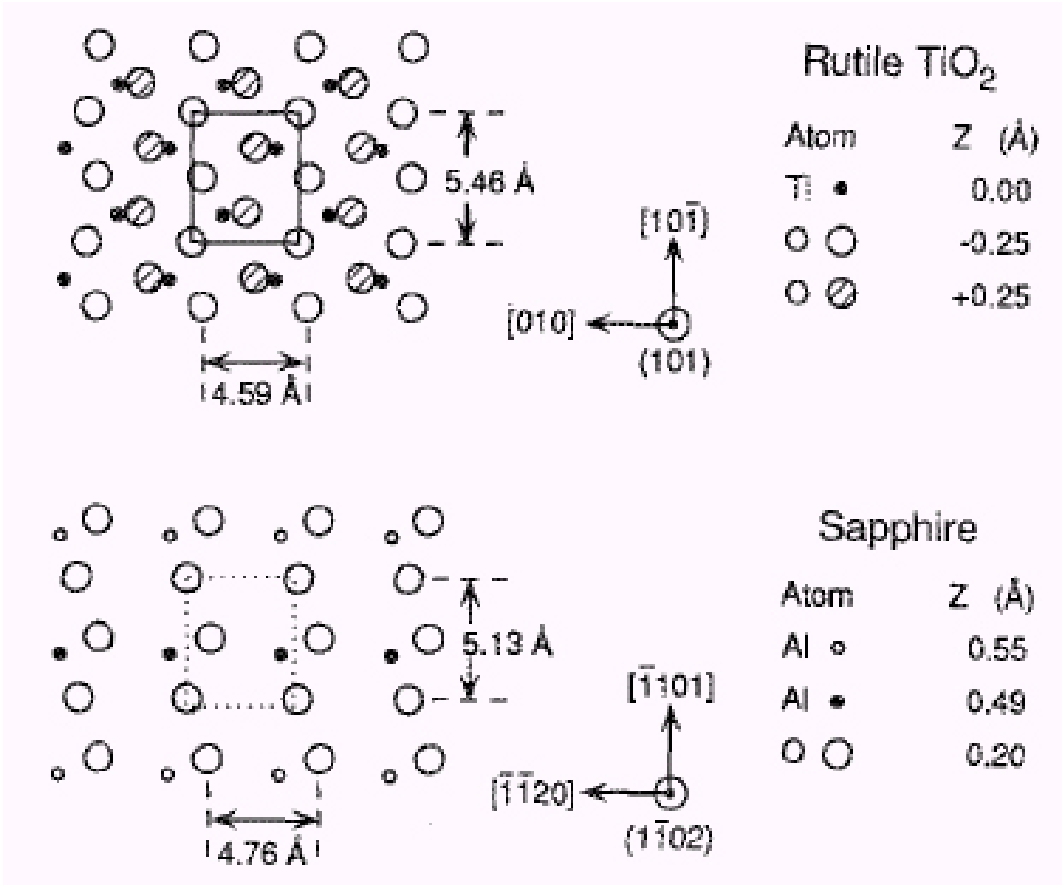

Fig. 3-5 Schematic draing of the atomic arrangements, scaled to ionic radii, showing the heteroepitaxy of rutile (101) on *a*-Al_2O_3 (1$\bar{1}$02). A TiO_2 reduced unit cell is overlaid on the sapphire plane to illustrate the close structural match between their oxide sublattices.

3-2-3 (001) oriented anatase type TiO_2 epitaxial thin films on perovskite type oxide single crystal substrate

Thin films fabrication was achieved by CLMBE method. Some perovskite type oxide single crystals, which are $SrTiO_3$ (STO) (001) and $LaAlO_3$ (LAO) (001), $LaSrAlO_4$ (LSAO) (001) and $YAlO_3$ (YAO) (001) were used as substrate. A TiO_2 ceramics target (99.99% purity) was ablated by KrF excimer laser (λ= 248 nm) with a typical laser fluence of 1.5 J/cm^2. The oxygen partial pressure and substrate temperature during the deposition were Po_2 = 1x10^{-6} Torr and T_S = 650°C, respectively. Typical deposition rates were 0.002 nm/pulse. A RHEED intensity monitoring system was employed to control the growth of the anatase films. The crystal structure, crystallinity and orientation of films were characterized by XRD.

The typical RHEED and XRD patterns of anatase thin films were shown in that fabricated on STO [Fig.3-6(a) and (b)], LAO [Fig. 3-6(c) and (d)], LSAO [Fig. 3-6(e) and (f)] and YAlO [Fig. 3-6(g) and (h)].

Epitaxial c-axis oriented anatase films could get on STO, LAO and LSAO not get on YAO substrate. The full width at half maximum (FWHM) of anatase (004) peak rocking curves are 0.6° on STO, 0.1° on LAO, 0.6° on LSAO. The FWHM value of anatase (004) peak rocking curve fabricated on LAO is the smallest. It can be concluded that these value differences are considered as the effect of lattice mismatch is clearly reflected in the crystal quality of the film as shown in table 3-2. Detailed discussion will be discussed in section 3-4.

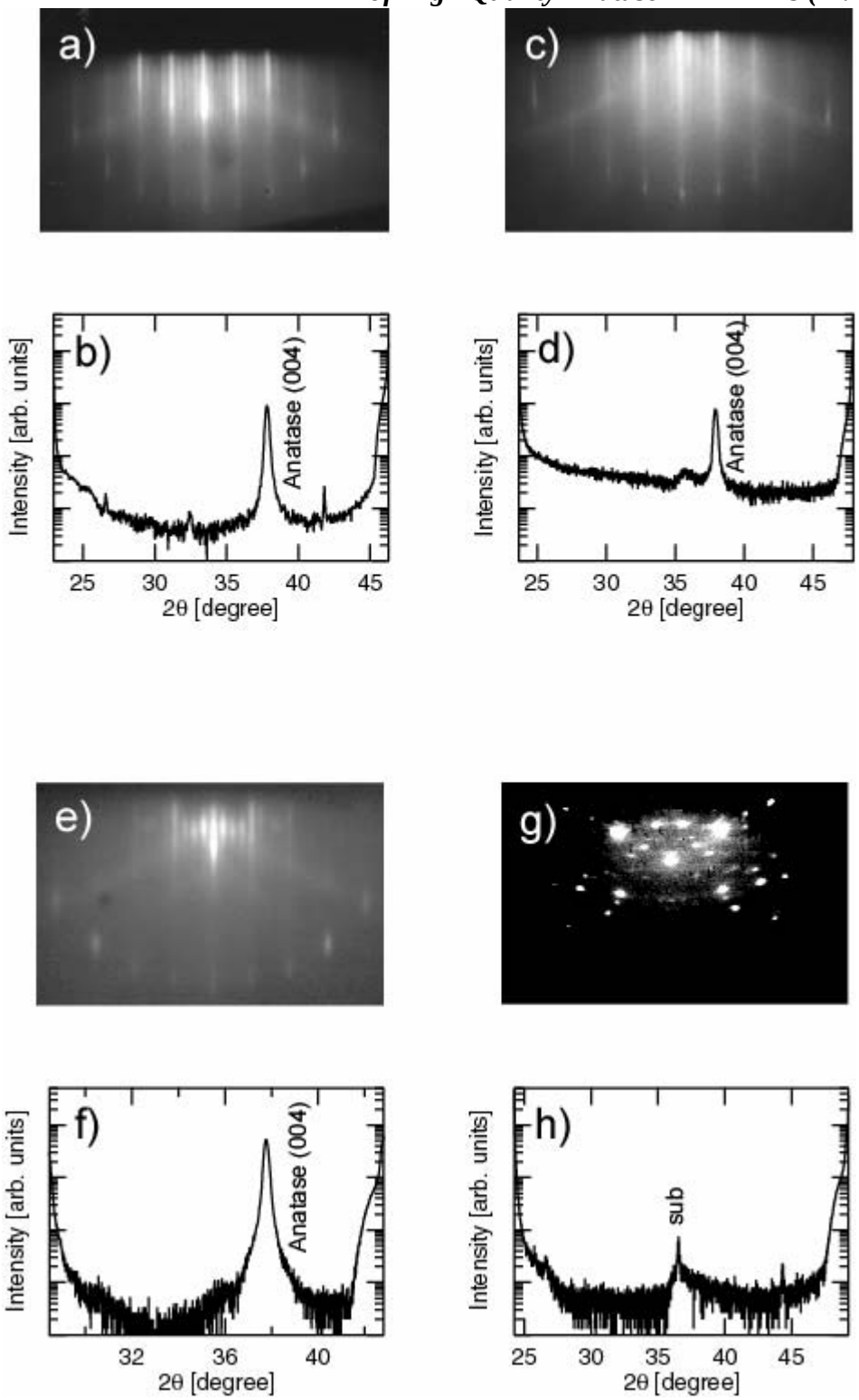

Fig. 3-6 RHEED patterns (upper one) and XRD patterns (lower one) of TiO_2 thin films deposited on various oxide single substrates. (a),(b) on $SrTiO_3$ (001), (c),(d) on $LaAlO_3$ (001) (e),(f) on $LaSrAlO_4$ (g),(h) on $YAlO_3$. Anatase thin films with *c* - axis oriented can grow on $SrTiO_3$ (001), $LaAlO_3$ (001) and $LaSrAlO_4$ (001) not on $YAlO_3$ (001).

3-3 Fabrication of epitaxial rutile / anatase bilayer thin films

It was difficult to fabricate [rutile/anatase] bilayer thin films because of thermal stability between anatase and rutile. Generally, bulk TiO_2 (A) is transformed into TiO_2 (R) at 800°C. So it is difficult to fabricate high crystallinity TiO_2 (A). Exploiting the interaction between epitaxial film and the underlying substrate by which films are more or less stabilized is one promising method to control the crystal structure. By using this template technique, [rutile/anatase] epitaxial bilayer thin film was obtained on STO (001).

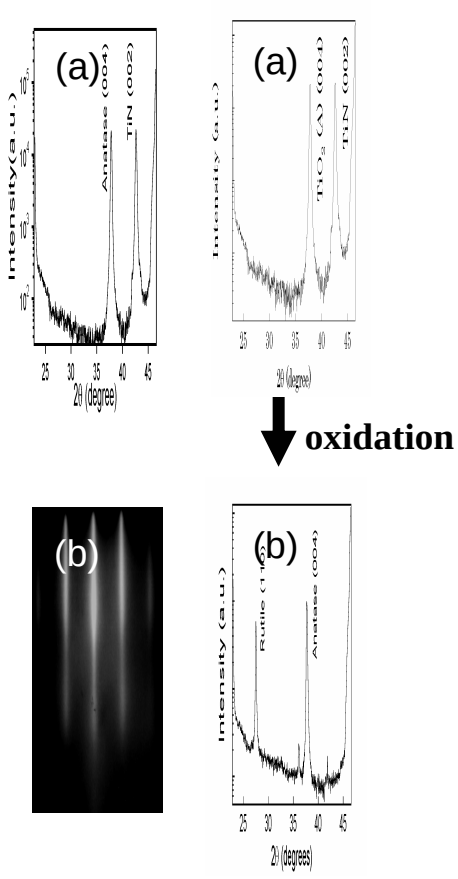

Fig. 3-7 (a) XRD pattern of [TiN (30 nm) / TiO_2 (A) (001)] deposited on STO (001) and (b) RHEED pattern of [TiN / TiO_2 (A) (001)] deposited on STO (001) in ultra-high vacuum at T_S = 650°C.

Fig. 3-8 XRD pattern of [TiN / TiO_2 (A) (001)] bilayer thin film ((a) and [TiO_2 (R) / TiO_2 (A) (001)] bilayer thin film by oxidized in P_{O2}=70 mTorr at T_S = 800°C.

Preparation of TiN thin films for acquiring oxidized TiO_2 (R) (110) thin films

I found that TiN thin films were epitaxially grown on STO (001) and TiO_2 (A) (001) is pre-deposited on STO (001). Fabrication of TiN thin films was achieved by the CLMBE method. TiN ceramic targets (99% purity) were ablated by KrF excimer laser (λ = 248 nm). Fabrication condition was chosen in ultra high-vacuum (UHV) at 650°C, and laser fluence and repetition rate was 5 J/cm^2 and 5 Hz.

XRD pattern and RHEED pattern of the TiN thin film fabricated on *c*-axis oriented anatase thin film are shown in Fig. 3-7. TiN thin films were epitaxialy grown on TiO_2 (A)(001).

Oxidation of TiN thin films, which fabricated on *c*-axis oriented anatase thin films, were carried out in 70 mTorr at 800°C. Based on the fact that TiN (A) was oxidized into rutile (110) oriented films, epitaxial rutile / anatase bilayer structure was fabricated confirmed by XRD results as shown in Fig. 3-8. Fig. 3-9 shows the cross sectional view of the bilayer film examined by scanning electron microscopy (SEM). The interface between TiO_2(R) and TiO_2 (A) layers is clearly observed. In addition, epitaxial relationship was confirmed by four-circles XRD measurements as shown in Fig. 3-10. From these results, [TiO_2 (R) /TiO_2 (A)] thin films were obtained with an epitaxial relationship. Mechanism of epitaxial orientational relationships can be understood in previous paper[9].

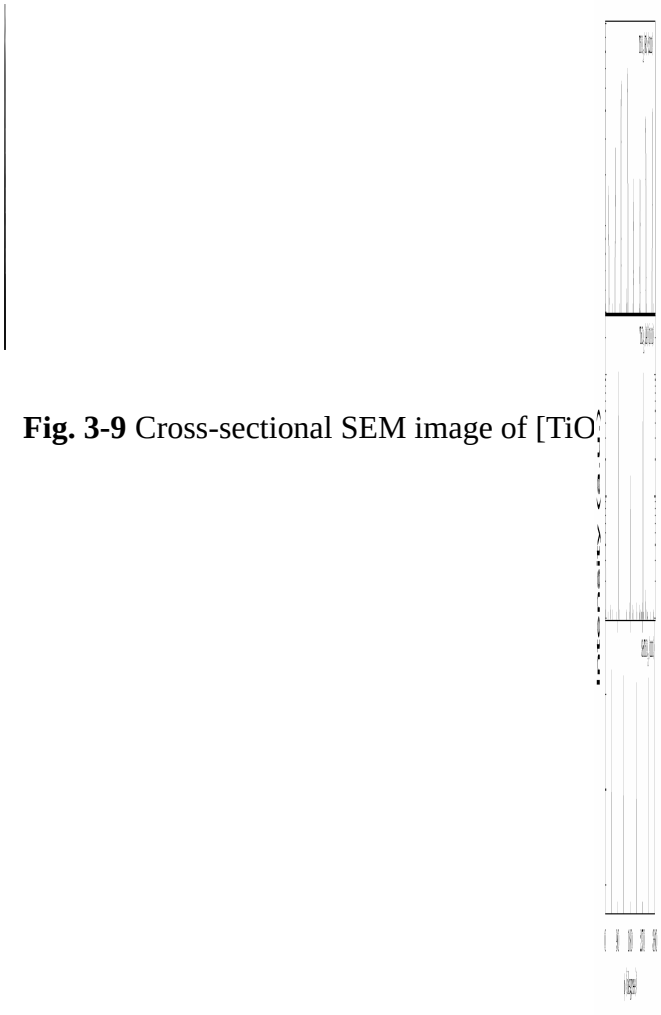

Fig. 3-9 Cross-sectional SEM image of [TiO / TiO_2 (A)] bilayer thin film.

Fig. 3-10 ϕ scan of [TiO_2 (R) (110) / TiO_2 (A) (001)] bilay
TiO_2 (A) (001)] bilayer thin film has epitaxial relationship be

3-4 Structural and Optical Characterization of Anatase Thin Films with High Crystallinity Fabricated on $LaAlO_3$ Substrate[10]

The differences of structural and optical properties of anatase thin films between fabricated on $SrTiO_3$ (STO) and $LaAlO_3$ (LAO) substrates are discussed in this section.

The oscillatory behavior of the specular beam spot intensity in the RHEED pattern was observed as shown in Fig. 3-11 during the deposition of TiO_2 on LAO substrate. Under the conditions of Po_2 = 1x10^{-6} Torr and *Ts* = 650 °C the TiO_2 film grew in a layer-by-layer fashion as noted by the streaky RHEED pattern. The periodicity of the intensity oscillation corresponds to the growth of 1/4 unit cell, i.e. one atomic-layer of TiO_2 along the *c*-axis, which is the minimum TiO_2 layer to satisfy charge neutrality. Likewise films grown at the above conditions on sapphire substrates possess the rutile crystal structure[11]. Furthermore, a clear (4x1) surface reconstruction was observed in the RHEED pattern as depicted in the inset of Fig. 3-11. In our scanning tunneling microscopy (STM) experiment shown in Fig. 3-12, one-dimensional (103) microfacets running along the [100] and [010] directions were observed on the anatase film surface. These results were in good agreement with those

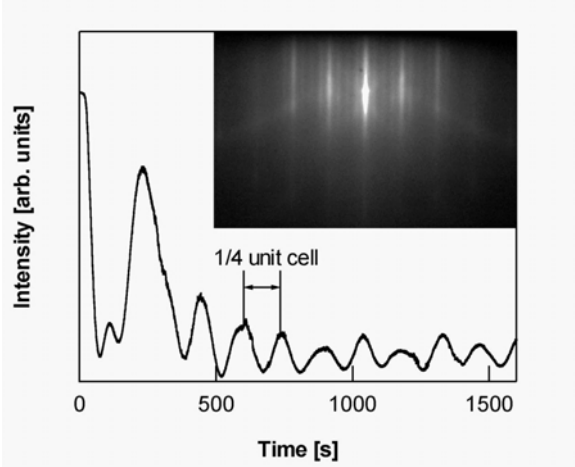

Fig. 3-11 The specular beam intensity in the RHEED pattern versus time during the deposition of TiO_2. The RHEED pattern for anatase thin films shows a (4x1) surface

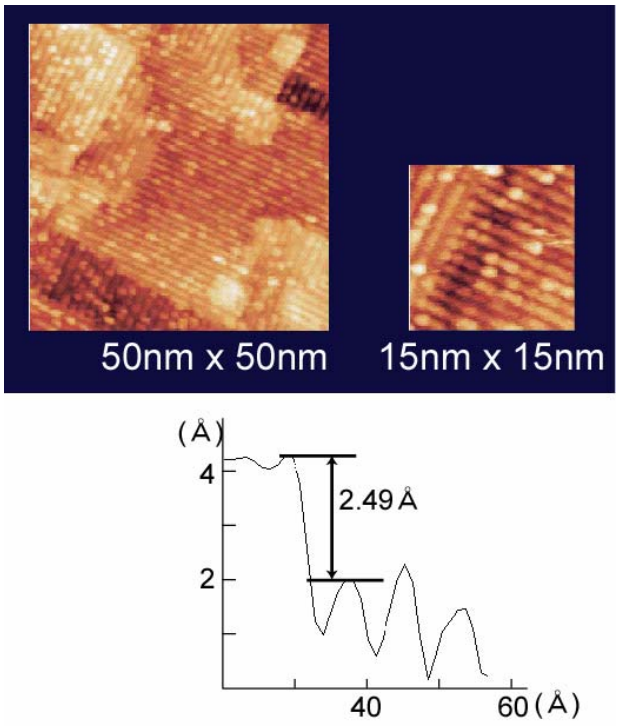

Fig. 3-12 STM image of anatase surface fabricated on $SrTiO_3$ (001) substrate. The one-dimensional (103) microfacets running along the [100] and [010] directions were observed on the anatase film surface.

reported by Chambers.[12] The detail STM results will be described elsewhere.

FWHM of the (004) peak rocking curve is 0.1° on LAO, while that of anatase film fabricated on $SrTiO_3$ (001) substrates under the same condition is larger than 0.6° discussed previous section (section 3-2). The differences of crystallinity between fabricated on these substrates are understandable to be compared with TEM images. Fig. 3-13 shows the cross-sectional TEM images of anatase thin films on a LAO (001) and a STO (001). The anatase film on the STO (001) has many defects and rough interface between the film and substrate induced by stress, while defects are much reduced and the sharp interface is observed in the film on LAO (001).

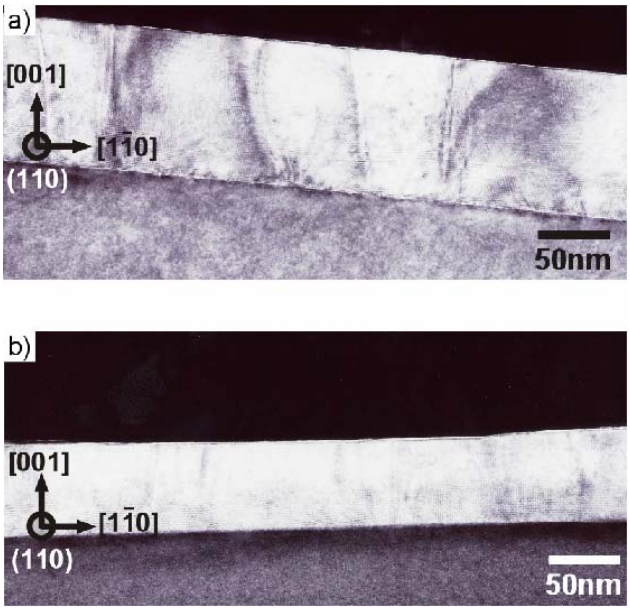

Fig. 3-13 The comparison of TEM images for anatase films grown on: (a) $SrTiO_3$ (001) and (b) $LaAlO_3$ (001) single crystal substrates. Some defects were observed in the film on $SrTiO_3$ (001) but less defects were observed that on $LaAlO_3$ (001).

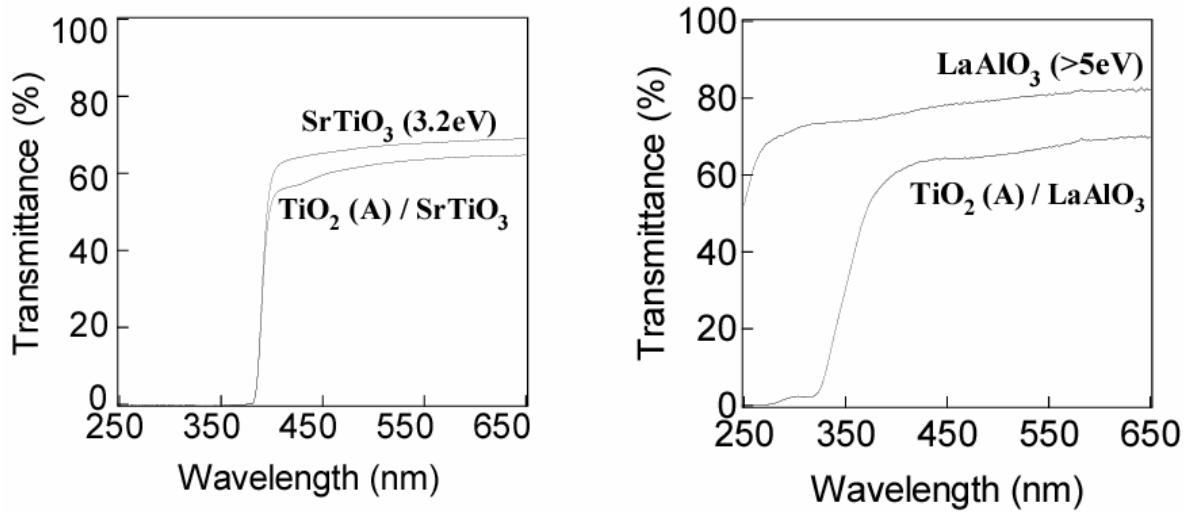

Fig. 3-14 The comparison of transmittance spectra for anatase films grown on: (a) $SrTiO_3$ (001) and (b) $LaAlO_3$ (001) single crystal substrates. Optical badedge, which of anatase film fabricated on $LaAlO_3$ (001), were clearey obserevd.

Another advantage of $LaAlO_3$ substrates is the possibility to evaluate the optical properties of the anatase thin film by virtue of $LaAlO_3$ large band-gap energy of ~5 eV. Fig. 3-14 shows transmittance spectra of anatase thin films fabricated on STO and LAO. The band-gap of STO is 3.2 eV, which band-gap is close to anatase, so it couldn't be observed optical band-gap from transmittance measurements as shown in Fig. 3-14(a). On the other hand, the absorption edge is clearly observed as shown in Fig. 3-14(b).

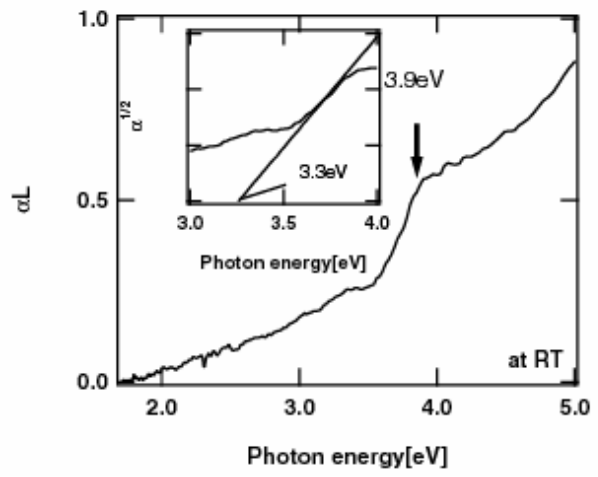

Fig. 3-15 Absorption spectrum of anatase thin film taken at room temperature. Band gap energy was determined to be 3.3 eV by plotting $\alpha^{1/2}$ against photon energy (inset), where α is absorption coefficient.

Fig. 3-15 shows the absorption spectrum of the anatase film. Assuming that the anatase's lowest inter-band transition corresponds to the indirect transition type, the band edge energy is evaluated by plotting $\alpha^{1/2}$ against photon energy where α represents the absorption coefficient in the inset of Fig. 3-15. The evaluated band gaps of 3.3 eV at room temperature and 3.4 eV at 5 K, were larger than those (3.2 eV and 3.3 eV, respectively) determined for bulk crystals.[13] In bulk single crystals, samples were so thick that the band-gap energy was determined either indirectly by analyzing its Urback tail, or by slicing and filing the sample to measure the transmittance spectrum. This difference in the evaluation methods is likely responsible for the minor discrepancy between the film and bulk band-gap energy values. The photoluminescence spectrum at 5 K (Fig. 3-16) exhibits a green broad emission band, with a peak energy located at 2.2 eV. This PL peak with 1.2 eV Stokes shift is presumed to originate from the recombination of self-trapped excitons[13]. The luminescence quenches at temperatures higher than 200 K. The imaginary part of the dielectric function, ε_2, evaluated

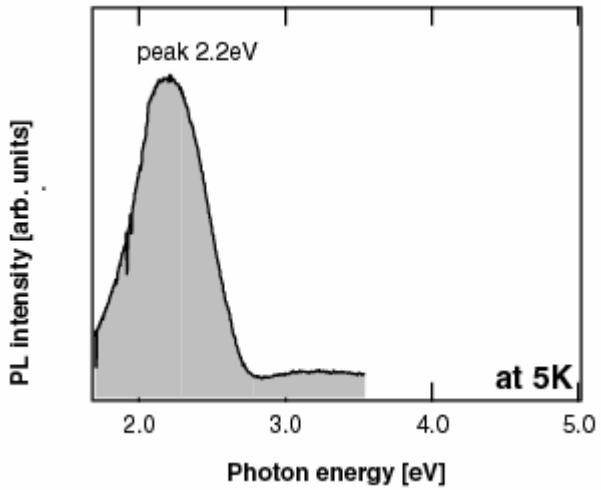

Fig. 3-16 PL spectrum taken at 5 K with its peak energy located at 2.2 eV.

for polarization vectors perpendicular to the *c*-axis (E ⊥ c) to show good agreement with the theoretical anisotropic spectrum reported by Asahi *et al.*[14]

This result clearly indicates that the anatase thin films fabricated on $LaAlO_3$ (001) by laser MBE have crystal quality equivalent to bulk single crystals, and therefore provide good specimens for elucidating their optical properties.

3-5 Conclusion

In conclusion, structural control of TiO_2 thin films was achieved by lattice matching between films and substrates. Take advantage of this technology, I succeeded in fabricating the rutile / anatase bilayer films with completing orientations.

Furthermore, the crystallinity of epitaxial anatase thin films has been remarkably improved by using $LaAlO_3$ (001) substrates as well as by the optimization of the laser MBE conditions. Atomically-controlled layer-by-layer growth was verified for the first time on anatase thin films by the observation of clear RHEED intensity oscillation, thus enabling the further fabrication of anatase epitaxial nano-films and their superlattices with other molecular layers. Optical properties of strain free anatase epitaxial films were precisely determined by virtue of the lattice-matched transparent $LaAlO_3$ substrate. The high-quality anatase thin films are advantageous not only for practical application to optical devices but also for basic studies on electric, optical, and photocatalytic properties of TiO_2.

Reference

[1] A. Fujishima, K. Honda, Nature 238 (1972) 37.

[2] S. Sato, Shokubai (catalyst) **31**, 469 (1989).

[3] Jaan Aarik, Aleks Aidala, Väino Sammelselg, Hele Siimon, and Teet Ustare, J. Cryst. Growth **169**, 496 (1996).

[4] H. Tang, K. Prasad, R. Sanjinès, P. E. Schmid, and F. Lévy, J. Appl. Phys. **75**, 2042 (1994).

[5] H. Berger, H. Tang, and F. Lévy, J. Cryst. Growth **130**, 108 (1993).

[6] H. Tang, H. Berger, P. Schmid, and F. Lévy, Solid State Commun. **92**, 267 (1994).

[7] Samuel Chen, M. G. Mason, H. J. Gysling, G. R. Paz-Pujalt, T. N. Blanton, T. Castro, K. M. Chen, C. P. Fictorie, W. L. Gladfelter, A. Franciosi, P. I. Cohen, and J. F. Evans: J. Vac. Sci. Technol. A **11** (5) (1993) 2419

[8] H. L. M. Chang, H. You, J. Guo and D. J. Lam: Applied Surface Science **48/49** (1991) 12

[9] M. B. Lee, M. Kawasaki, M. Yoshimoto, B. K. Moon, H. Ishiwara, H. Koinuma: Jpn. J. Appl. Phys. **34** 2B (1995) 808

[10] M. Murakami, Y. Matsumoto, and K. Nakjima, T. Makino and Y. Segawa, T. Chikyow and P. Ahmet, M. Kawasaki and H. Koinuma, Applied Physics Letters 78 16 2664-2666 (2001)

[11] Y. Matsumoto, M. Murakami, Z.W. Jin, A. Nakayama, T. Yamaguchi, T. Ohmori, E. Suzuki, S. Nomura, M. Kawasaki, H. Koinuma; Proc. SPIE **3941** 19-27 (2000)

[12] Scott A. Chambers, Surf. Sci. Rep. **39**, 105 (2000).

[13] H. Tang, H. Berger, P. E. Schmid, F. Lévy, and G. Burri, Solid State Commun. **87**, 847 (1993).

[14] R. Asahi, Y. Taga, W. Mannstadt, and A. J. Freeman, Phys. Rev. B **61**, 7459 (2000).

Chapter 4 Combinatorial Screening of 3d Transition Metals Doped Titanium Dioxide: Photocatalytic Characterization by pH Imaging Apparatus

4-1 Introduction

The catalyst activity can be drastically modulated by changing the mixing ratio of corresponding compounds, particle size and treatment procedures which generate the so-called active sites on the surface. Development of catalytic activity has much been predominantly a process of trial and error. TiO_2 has widely been used as a catalyst of water cleavage[1] and NO_X and SO_X decomposition. TiO_2 has excellent efficiency in conversion of photon to electron-hole pair in UV light region. However, TiO_2 has large bandgap, rutile type is 3.0eV and that of anatase type is 3.2eV. So, only UV-light region was available. Surface derivatization of TiO_2 with numbers of organic dyes extends the sensitivity of TiO_2 into the visible region by injection of electrons from an excited level of dye into semiconductor conduction band. Gratzel and co-workers made a breakthrough in preparing a low-cost, high-efficiency dye-sensitized photoelectrochemical solar cell using nano-crystalline porous TiO_2 thin film, where light harvesting efficiency was increased to almost 100% because of high surface area of the porous TiO_2 film[2]. However, commercialization of this cell could not be realized because of some practical difficulties, such as stability. Hence, it is necessary to control the band structure of TiO_2 to use not only visible-light region but also use UV-light region. Indeed, photo-catalytic properties of TMs doped TiO_2 were reported elsewhere[3,4], it has been said that photo-catalytic activity was reduced by increasing TMs content in TiO_2. There are two main steps in a photocatalytic reaction, namely the generation of electron hole pairs by illumination and their consumption on the surfaces. The use of epitaxial TiO_2 thin films allows us to focus on the first process i.e., the generation of electron hole pairs since there will be much smaller contribution from effects of surface area or particle size in the highly crystalline TiO_2 film. Reported TMs doped TiO_2 is considered that TMs will form trap-center, and lifetime of electron-hole pair will be shortened by this trap-center. With this motivation, CLMEB method was employed to fabricate epitaxial TiO_2 films doped systemically with TMs.

4-2 Preparation of transition metal doped TiO_2 thin films

4-2-1 Fabrication of Transition Metal Doped TiO_2 Thin Films

TMs doped TiO_2 thin films were systemically fabricated. All 3d TMs, Nb, Zr, Sn, and Er were chosen as doping elements. TiO_2 (R) on Al_2O_3 (0001) and TiO_2 (A) on STO (001) thin films doped with TMs were prepared. This combinatorial doping experiment yielded 234 distinct samples as shown in Fig. 4-1. Ion charge listed in Fig. 4-1 was estimated from Ellingham diagrams[5,6]. To our knowledge, epitaxial TiO_2 thin films systemically doped with TMs were first report. Fabrication procedure was described in Chapter 2 Fig. 2-3 (b), and calibration of doping concentration in TiO_2 thin films was determined by electron probe micro analyzer (EPMA) measurements (S-4000 HITACHI and EPMA-1400 SHIMADZU). Discussion about enrichment factor is shown in section 4-2-2. The enrichment factor of TMs doped TiO_2 (R) is close to 1 (f=1). It is difficult to determine doped concentration in TiO_2 (A) because titanium also exists in STO substrate. However, anatase type TiO_2 thin films were fabricated by the same design and the same day as for the rutile type, so that enrichment factor of anatase combinatorial libraries were regarded as almost the same.

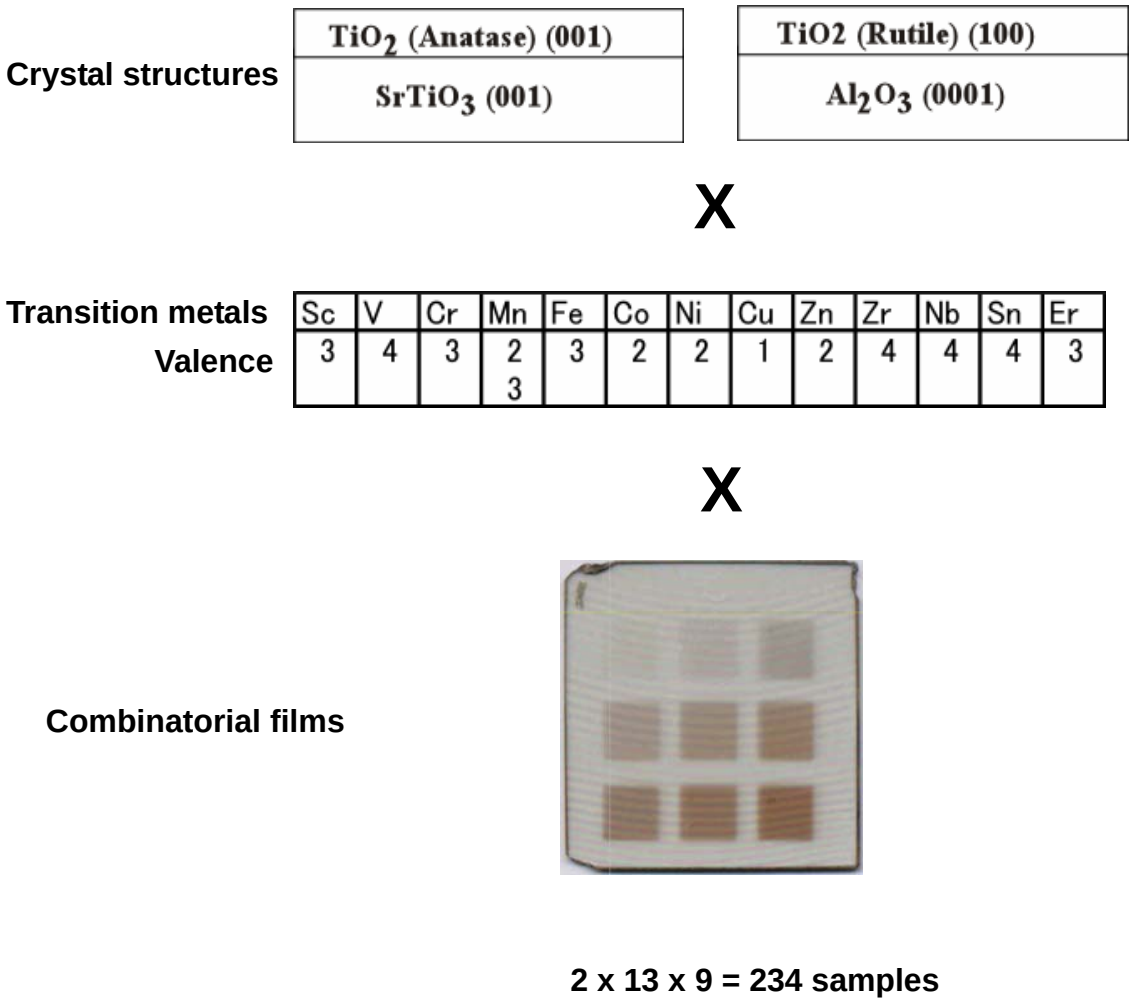

Fig. 4-1 Combinatorial experiments for TiO_2 doped with transition metals.

4-2-2 Enrichment factor

If designed and experimental concentration were defined respectively as C_d and C_e, enrichment factor *f* is then defined as $f = C_e/C_d$. Fig. 4-2 and Fig. 4-3 show enrichment factor of Mg doped ZnO (as shown in section 2-4-1) and transition metals (TMs) doped TiO_2, respectively. It can be said that enrichment factor of Mg doped ZnO was close to 2 (*f*=2) [Fig. 4-2] while enrichment factor of 3d TMs doped TiO_2 thin films were close to 1 (*f*=1) [Fig. 4-3]. It is attribute to the difference of vapor pressure between doped materials and mother matrix, and scattering of ablated materials. Enrichment factor was well studied for oxide complexes fabricated by pulsed laser deposition (PLD) technique[7]. In high-pressure atmosphere, light species with a high collisional cross section suffer significant deviations during the plasma expansion whereas heavy species suffer little deviation.

Fig. 4-2 Calibrated Mg contents in ZnO films compared with designed Mg contents

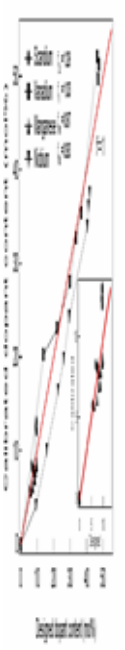

Fig. 4-3 Calibrated TMs contents in TiO_2 (R) films compared with designed TMs contents.

However, since 3d-ions were chosen as dopants for TiO_2, the scattering effect is not so distinct. Because, in our conditions, the oxygen pressure was chosen 1×10^{-6} Torr and the mass of materials were not so different from each other. For Mg doped ZnO thin films, one of the possible reasons for such large enrichment factor may be the preferential re-evaporation of ZnO due to the difference of vapor pressures between ZnO and MgO.

4-3 Characterization of combinatorial libraries

4-3-1 Solubility limits

Solubility limit of TMs were systemically obtained from XRD measurements. Solubility limit of each TMs dopant in TiO_2 thin films are presented in Fig. 4-4. Secondary phase precipitated in the films having higher concentration of dopant than the solubility limit. In spite of excess TMs doping in TiO_2, some of TMs doped TiO_2 samples were found to be single phase. It is noteworthy that the solubility limit of the dopants varies significantly depending on the 3d ion species as well as on the involved crystal structure of TiO_2 (anatase or rutile). For example, V and Fe dopants, which are well known to form bulk solid solution alloys in high concentrations in the rutile than in anatase phase, Ni is not soluble in both the phases. Due to more non-equilibrium state in thin film process, the tendency of solubility limits is different from that of bulk and it is possible to make highly doped films that are not obtainable under equilibrium condition. In addition, to our knowledge, there has been no report on the solubility limits of TM in anatase.

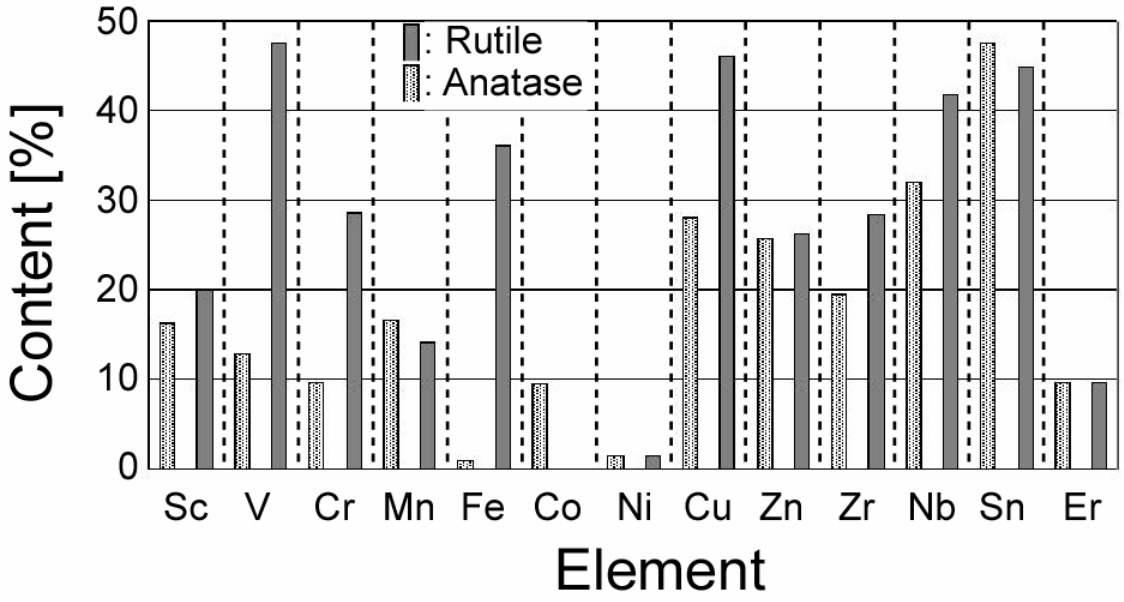

Fig. 4-4 Solubility limit of TMs in TiO_2 matrix.

4-3-2 Photo-catalytic Properties Screening by pH Imaging Apparatus

Fig. 4-5 (a) shows electrochemical cell and measurement setup of pH imaging apparatus as discussed in section 2-3-1. Fig. 4-5(b) shows pH distribution generated by water photo-decomposition on the Co doped TiO_2 (R) thin films integrated in the deposited combinatorial library. This shows that the difference of activity among TiO_2 films with different Co doping can be clearly detected by the pH imaging technique developed by us. Thus the pH imaging technique is a valuable tool for the high-throughput evaluation of photo-catalytic activity in combinatorial libraries. Besides, this method can find prospective applications for the parallel evaluation of other electrochemical functions, which can be translated into the equivalent pH changes.

We have tried to get excellent photo-catalyst through a combinatorial screening of 3d TMs doped titanium oxide by combinatorial Photo-catalytic characterization apparatus. However we couldn't get systemically results. It was difficult to evaluate quantitatively and reproducibly by this pH imaging apparatus. But now, collaborators, Mr. T. Ohsawa and Ms. K. Nakajima, are working in photo-catalytic properties of TiO_2 thin films from another point of view, such as photo-catalytic properties at atomic scale by scanning tunneling microscope (STM).

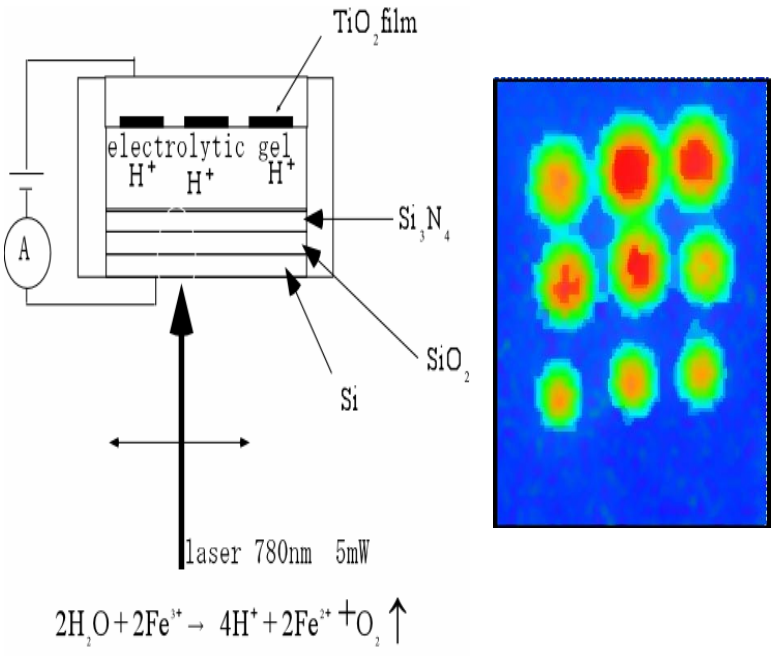

Fig. 4-5 (a) Electrochemical cell and measurement setup (b) pH distribution on the Co doped TiO_2 (R) thin films integrated in the combinatorial library.

4-4 Conclusions

Fabrication and structural characterization of transition metals (TMs) doped TiO_2 were discussed. More than 200 TiO_2 samples doped TMs were fabricated only in a few weeks. Solubility limit of TMs into anatase and rutile structures were systemically obtained. Furthermore, photo-catalytic screening was achieved by two-dimensional pH imaging apparatus. Photo-catalytic activity differences of Co doped rutile on *c*-Al_2O_3 were clearly obtained with this method, but it was difficult to evaluate photo-catalytic activities of another combinatorial libraries quantitatively and reproducibly comparing.

Reference

[1] Fujishima and K. Honda: Nature **238**, (1972) 37

[2] Brian O'Regan and Michael Grätzel: nature **353** (1991) 737

[3] K. E. Karakitsou and X. E. Verykios: J. Phys. Chem., **97**, 1993, 1184

[4] Nick Serpone, Darren Lawless, Jean Disdier and Jean-Marie Herrmann : Langmuir 1994, **10**, 643

[5] Iron and Steel Society of Japan, Handbook of Iron and Steel (Maruzen Joint Stock Corporation, Tokyo 1981), 3rd edition, p.7.

[6] Electrochemistry Society of Japan, Handbook of Electrochemistry (Maruzen Joint Stock Corporation, Tokyo 1985), 4th edition, p.129

[7] C. N. Afonso, J. Gonzalo: Nuclear Instruments and Methods in Physics Research B **116** (1996) 404

Chapter 5 Discovery of Room Temperature Ferromagnetic Materials: Titanium Dioxide Thin Films Doped with Cobalt

5-1 Introduction

Improvement of photo-catalytic properties of TiO_2 was interrupted because of imperfection of photo-catalytic evaluation system for combinatorial libraries. However, can I use TMs doped combinatorial libraries for another purpose? TiO_2 is one of the semiconductors that have wide optical band-gap. Diluted magnetic semiconductors (DMSs), which non-magnetic semiconductors doped with magnetic ion, are one of the most active categories in semiconductors and magnetisms. TMs doped TiO_2 can be seen as one of the DMSs.

Spins can be controlled by carrier, photon and photon-carrier spin interactions. DMSs have been attracted for the new device application with these special features. The concentration works as a DMS have been interested in II-VI, III-V semiconductors. The highest curie temperature was 110K of (Ga,Mn)As. However, the materials, which ferromagnetic magnetism remains above room temperature, are critically important in the development of spintronics as spin injectors for semiconductor heterostructures that can operate without cryogenic cooling. The backgrounds about DMS are discussing follows.

In this chapter, discovery of transparent ferromagnetic materials Co doped titanium dioxide (TiO_2) even above room temperature through the combinatorial screening. High-throughput screening of TMs doped TiO_2 combinatorial libraries by scanning superconducting quantum interference device microscope (SSQM) are discussing in Section 5-2. Structural characterizations and magnetic properties of anatase thin films doped with Co are discussing in Section 5-3-1, and rutile thin films doped with Co are discussing in Section 5-3-2.

5-2 Magnetic Characterization of 3d Transition Metals (TMs) Doped TiO_2 Combinatorial Libraries

Magnetic characterization screening of 3d transition metals (TMs) doped TiO_2 combinatorial libraries ware achieved by SSQM. Using a SSQM technique, as shown in section 2-3-2, magnetic properties of 3d-doped TiO_2 film libraries were screened quickly. Fig. 5-1 shows the

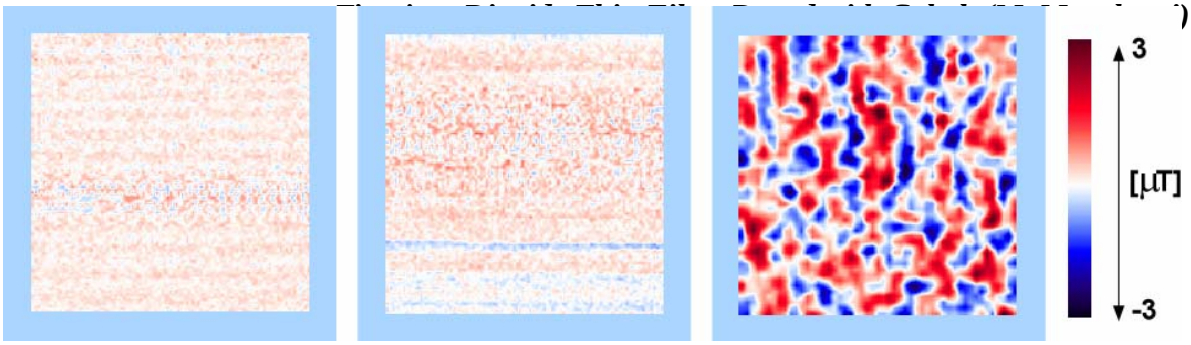

Fig. 5-1 Scanning SQUID images (200 μm x 200 μm) for: (a) Cr doped rutile film (x=0.52), (b) Mn doped anatase film (x=0.53), (c) Co doped anatase film (x=0.06).

SSQM images taken at 3 K for anatase films doped with Co (x = 0.06) and with Mn (x = 0.53) as well as for rutile film doped with Cr (x = 0.53) on the combinatorial chips. The magnetic domain structures of ca. 20 μm size can be clearly seen in the Co-doped anatase film, while the non-doped and Cr- and Mn-doped TiO_2 do not exhibit any magnetic structure.

5-3 Room Temperature Ferromagnetism in Transparent Transition Metal Doped Titanium Dioxide

5-3-1 Ferromagnetism in Anatase Thin Films

$LaAlO_3$ (001) and $SrTiO_3$ (001) single crystals were used as substrates[1]. To observe systematic changes of film properties as a function of doping level, we fabricated a combinatorial library integrating nine $Ti_{1-x}Co_xO_2$ films with different x values on a single substrate by the combinatorial laser molecular beam epitaxy technique[2] as shown in chapter 2 in 1 x 10^{-5} to 1 x 10^{-6} Torr of oxygen at 950 to 1000 K. TiO_2 and Co-doped $Ti_{0.5}Co_{0.5}O_2$ ceramic targets were ablated with KrF excimer laser pulses (248 nm) that were synchronized with the rotational motion of combinatorial masks. The details of the combinatorial procedure have been described Section 2-2-1[3]. The Co contents in a series of $Co_xTi_{1-x}O_2$ films were determined by electron probe microanalysis. In the x-ray diffraction (XRD) pattern of a Co-doped TiO_2 film with x = 0.08 (Fig. 5-2 A), only the (004) and (008) peaks of the anatase phase were observed, and the change of the lattice constant followed Vegard's law, as shown in the inset. Moreover, transmission electron microscope (TEM) observations (Fig. 5-2 B) indicate no sign of segregation of impurity phases in the Co/Ti compositional range of x = 0.08; the lattice image and diffraction pattern of Co-doped anatase are identical to those of

pure (x = 0) anatase. From these XRD and TEM results, it is concluded that a sizable amount of Co, at least up to x = 0.08, is soluble, i.e., homogeneously distributed in anatase. Probably because of the quasi-equilibrium nature of laser molecular beam epitaxy, the formation of $CoTiO_3$ and $CoTi_2O_5$, which are known to exist in the bulk Co-Ti-O phase diagram, was not observed. A series of magnetic images were taken by a SSQM at 3 K for anatase films with different Co contents (x = 0 to 0.06) on a combinatorial chip (Fig. 5-3). In all of the Co-doped films, magnetic domain structures of around 20 mm in size can be seen. The pure TiO_2 (x = 0) film and the $LaAlO_3$ substrate do not show any magnetic structure within an experimental error of 0.5 μT, consistent with the report by Chauvet *et al.*[3]. With increasing Co content in the film, the magnitude of the magnetic field is systematically enhanced as a

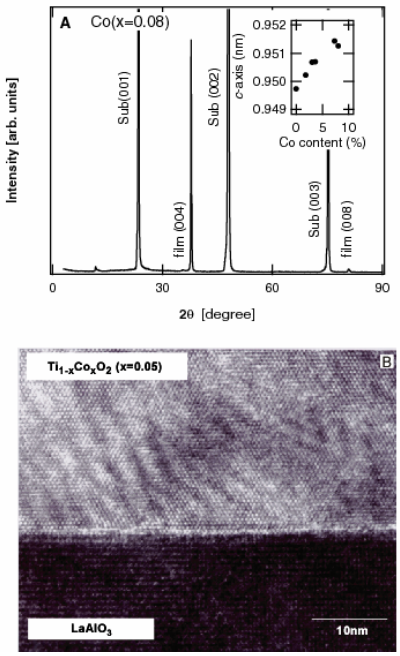

Fig. 5-2. (**A**) An XRD pattern of a Co-doped TiO_2 film (x = 0.08) showing (004) and (008) peaks of anatase without any impurity peaks. The c-axis length increased monotonously with increasing Co content following Vegard's low (inset). (**B**) Atomic resolution TEM image of a Co doped TiO_2 film. No segregation of impurity phases was observed in the film.

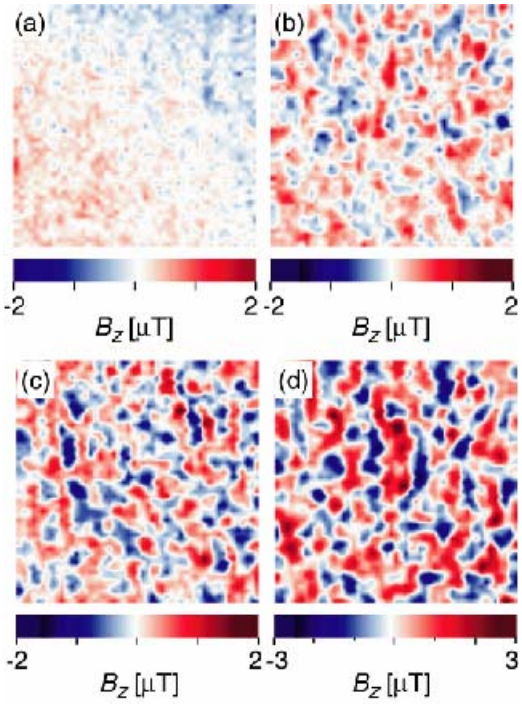

Fig. 5-3. A series of scanning SQUID microscope images (200 μm x 200 μm) taken at 3 K for anatase thin films with different Co contents on a combinatorial chip. (**A**) x = 0, (**B**) x = 0.02, (**C**) x = 0.03, and (**D**) x = 0.06. Magnetic domain structures were observed in all doped films, suggesting the presence of long-range ordering of magnetic moments induced by Co doping in the anatase thin film.

result of the increased spontaneous magnetization. These observations show that ferromagnetic long-range order emerges in the Co-doped TiO_2 anatase phase. We observed no sign of such ferromagnetic behavior in any other combinatorial TiO_2 film chips, either in the anatase or rutile phase, in which transition metals were solid soluted. The magnetic response was measured as a function of magnetic field strength (H) (Fig. 5-4) for the x = 0.07 film on $SrTiO_3$ (001) at room temperature, where the magnetic field was applied parallel to the film surface. Hysteresis is observed (Fig. 5-4 A), indicating that the Co doped anatase film is ferromagnetic even at room temperature. Spontaneous magnetic moment per Co atom was deduced from the saturated magnetization (M) value to be 0.32 μB. From the M-temperature (T) curve in a field of 20 mT applied parallel to the surface (Fig. 5-4 B), T_C is estimated to be higher than 400 K, substantially higher than the values (~100 K) reported so far for other 3d-doped ferromagnetic semiconductor[4]. The optical properties of $Ti_{1-x}Co_xO_2$ anatase film are good, with the film remaining transparent in the visible and near-infrared regions and exhibiting a band gap at 400 nm (3.1 eV). The transparency is demonstrated by the clear image of letter A, which is placed beneath a $Ti_{1-x}Co_xO_2$ (x = 0.06) film on $LaAlO_3$ substrate (inset of Fig. 5-4 A). Different from two ferromagnetic materials, $FeBO_3$ and FeF_3, that were reported to be transparent but green in color[5], the Co-doped anatase is colorless and has appreciable conductivity. The resistivity and carrier concentration of the $Co_xTi_{1-x}O_2$ film are about 0.1 to 1 ohm/cm and 10^{18}/cm^3, respectively, at room temperature, being scarcely dependent on the Co doping level. The ferromagnetic $Co_xTi_{1-x}O_2$ film (x = 0.07) on $LaAlO_3$ exhibits a positive magnetoresistance (MR) of as much as 60% at 2 K in a field of 8 T applied normal to the surface (Fig. 5-5) and represents an observation of MR in anatase films. The mixing of granular precipitates of magnetic materials, Co clusters for instance, can be a reason for the observed spontaneous magnetism[6,7]. Although the possibility cannot be

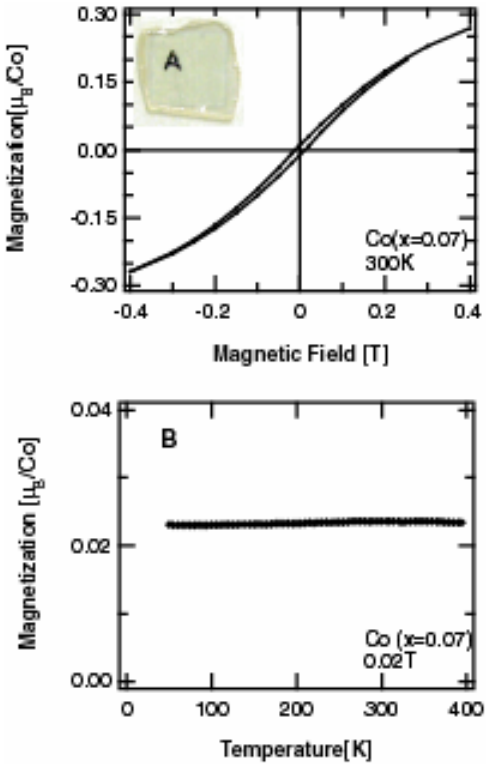

Fig. 5-4 (**A**) An M-H curve of an x = 0.07 film on $SrTiO_3$ taken at room temperature. Magnetic field was applied parallel to the film surface. Hysteresis is observed, indicating that the Co doped anatase film is ferromagnetic even at room temperature. The film is transparent enough in the visible and near-infrared region to make the background letter (A) visible (inset). (**B**) An M-T curve in a field of 20 μT parallel to the surface. T_C is estimated to be higher than 400 K.

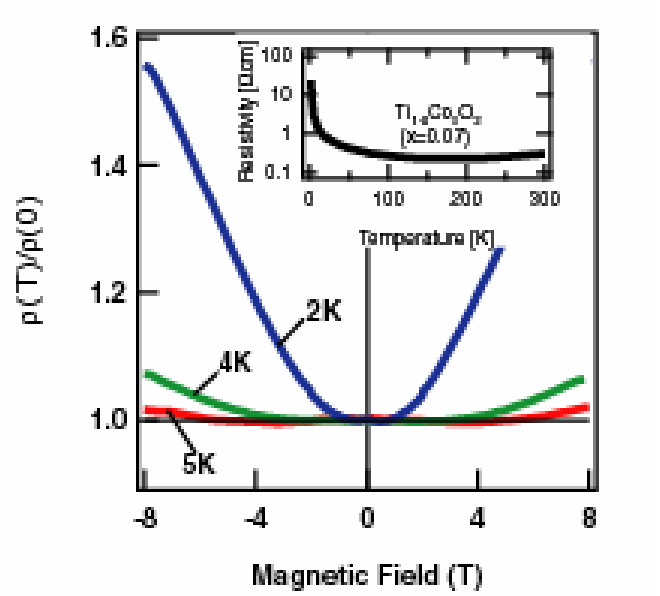

Fig. 5-5 The MR measurements of the x = 0.07 specimen in the temperature range of 2 to 5 K. A positive MR = 60% is observed at 2 K in a field of 8 T applied normal to the surface. The temperature dependence of the resistivity is also shown (inset).

completely ruled out at present, the XRD and TEM measurements show no sign of such metal granules as mentioned before. If the clustering of cobalt occurred, we should have observed such granules in TEM image as were reported by Mitani *et al.*[15]. Assuming that thermal equilibrium is reached in our growth conditions, the valence state of Co ions should be either Co^{2+} or Co^{3+}, in view of the facts that the films were deposited at 950 to 1000 K and cooled down to 500 K in 1 x 10^{-6} to 1 x 10^{-5} Torr of oxygen[8]. If Co ions are in high spin state, we expect S to vary from 3/2 to 4/2, depending on the mixing ratio of Co^{2+} and Co^{3+} in the film, giving a spontaneous magnetic moment m_{sp} between 3 and 4 μB/Co. Meanwhile, the low spin states of Co^{2+} and Co^{3+} yield at most S = 1/2 (m_{sp} = 1 μB/Co). The low spin configuration of Co ions is thus consistent with the observed magnetic moment in the *M-H* curve in Fig. 5-4 A.

5-3-2 Ferromagnetism in Rutile Thin Films

In this study, we used α-Al_2O_3 ($10\bar{1}2$) to obtain epitaxial films of rutile TiO_2 with (101) orientation. Alternate ablation of 5 mol% Co-doped and non-doped TiO_2 ceramics targets by KrF excimer laser (248 nm) was employed to control the Co content from x = 0 to 0.05 in the $Co_xTi_{1x}O_2$ films. Typical laser fluence and repetition rate were 0.7 J/cm^2 and 5 Hz, respectively. The partial pressure of oxygen in the chamber and substrate temperature were 1 x 10^{-6} Torr and 700°C, respectively. In our reflection high energy electron diffraction (RHEED) monitoring system, it is possible to monitor the intensity oscillation of the specular beam spot in the RHEED pattern during the growth. The crystal structure and Co content were determined, respectively, by conventional x-ray diffraction (XRD) and electron probe microanalysis (EPMA). The surface morphology was observed by using a scanning electron

microscope (SEM) and an atomic force microscope (AFM). The magnetic properties were examined by a SSQM (Seiko Instrument SSQ-7000) and conventional SQUID. During the film growth, we clearly observed the oscillatory behavior of the specular beam spot intensity in the RHEED pattern, as shown in Fig. 5-6, indicating the layer-by-layer growth of TiO_2 films on Al_2O_3 $(10\bar{1}2)$ substrate. The RHEED image (inset in Fig. 5-6) and (2θ–θ X-ray diffraction pattern of the film confirms the epitaxial growth of rutile phase with (101) orientation[9]. Consequently, the periodicity of the intensity oscillation corresponds to the *d* value (2.48 Å) of the (101) diffraction peak in rutile. Up to 5 mol% Co doping, no impurity phase was detected in the XRD patterns as shown in Fig. 5-7 (a) (x = 0.05). Figure 5-7 (b) shows a systematic decrease of the *d* (101) value evaluated with an increase of Co content. It is noteworthy that the full width at half-maximum (FWHM) of (101) peak for a rocking curve scans was also decreased from 2 to 0.6 with increasing Co content. These results suggest that a good solid-solution of Co–TiO_2 rutile alloy is formed accompanied by the improvement of crystallinity. From the AFM and SEM measurements, we could not see any trace of surface segregation of CoO_x and $CoTiO_x$, which are the major impurity phases in the bulk. Furthermore, the surface morphology of the Co-doped rutile films was quite smooth, and their morphology is almost identical to that of non-doped films (Fig. 5-8).

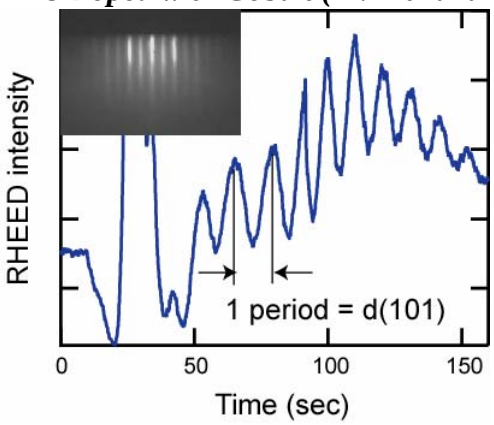

Fig. 5-6 The specular beam intensity in the RHEED pattern vs. time during the deposition of TiO_2. Inset image is the RHEED pattern in the film.

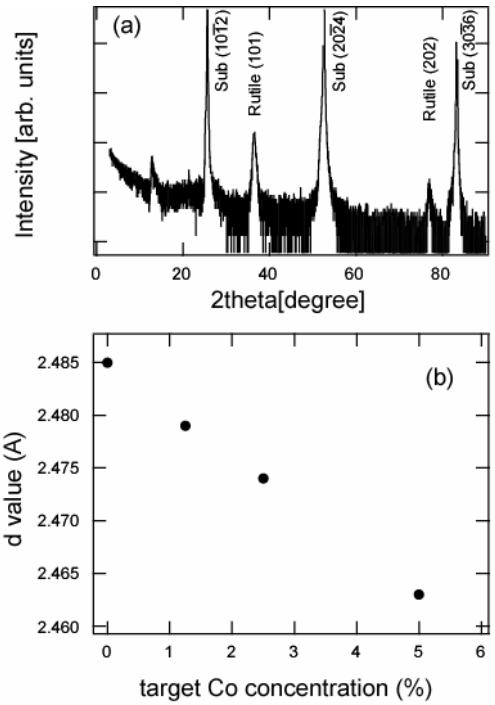

Fig. 5-7 (a) XRD pattern of 5 mol% Co doped TiO_2 thin film deposited on α-Al_2O_3 $(10\bar{1}2)$ single substrate. Co-doped rutile (101) film was epitaxialy grown with no impurity phase. (b) A systematic decrease of the evaluated d value for the (101) diffraction peak was observed with an increase of Co content.

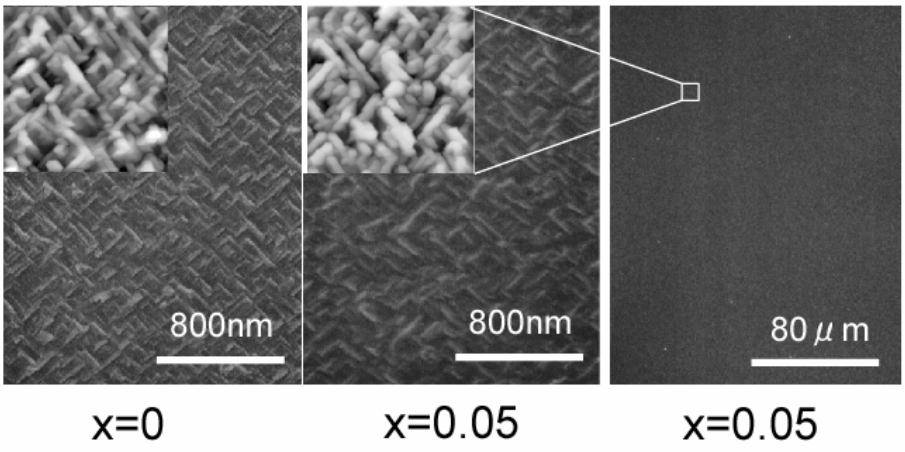

Fig. 5-8. SEM images for pure and 5 mol% Co doped TiO_2 rutile films. AFM images also inset in the SEM images.

The magnetic properties of Co-doped TiO_2 rutile films were examined with a SSQM. Figures 5-9 (a) and 5-9 (b) are SSQM images of non-doped and 5 mol% Co-doped TiO_2 rutile films, respectively, taken at 3K. Magnetic domain structures with sizes of ~10 μm can be clearly seen in the Co-doped TiO_2 rutile films, giving direct evidence for the presence of spontaneous magnetization. We have recognized that the domain structure is essentially unchanged with temperature below 90K. In contrast, no sign of such magnetic domain structure is observable in the non-doped TiO_2 rutile film.

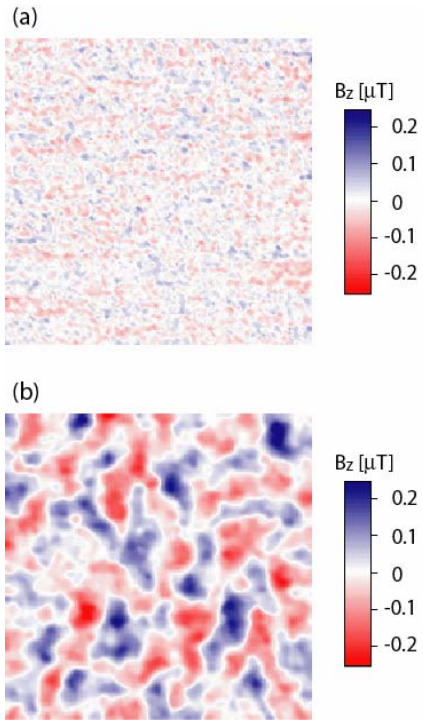

Fig. 5-9. Scanning SQUID images (200 μm × 200 μm) for (a) pure and (b) Co doped (x = 0.05) TiO_2 rutile films.

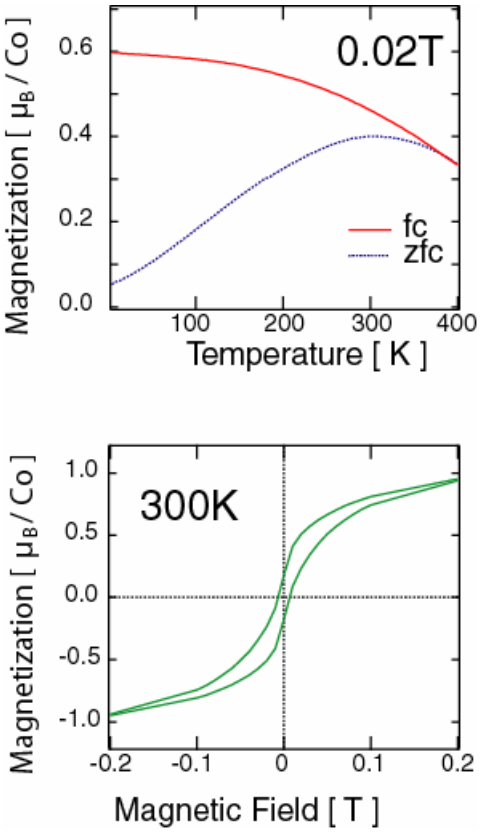

Fig. 5-10. (a) An *M-T* curve in a field of 20 mT parallel to the surface. *T*C is estimated to be higher than 400 K. (b) An *M-H* curve of a Co doped (x = 0.05) TiO_2 rutile films taken at room temperature. Magnetic field was applied parallel to the film surface. Hysteresis is observed, indicating that the Co doped rutile film is ferromagnetic even at room temperature.

Fig. 5-10 shows M-T curve in a filed of 20mT parallel to the surface, and M-H curve of a Co doped rutile films taken at room temperature. According to the M-H measurements using a conventional SQUID susceptometer, magnetic hysteresis survives, at temperatures up to 400K, which was the highest for measurement. The moment saturates at ca. 1.0μB/Co atom at room temperature. Taking the growth condition (P_{O2} = 10^{-6} Torr and substrate temp. T_S = 700°C) into account, the valence state of Co is expected to be 2+ from the viewpoint of thermodynamics. Thus, the magnetic moment is comparable to that expected for the low spin state of Co^{2+} (S = 1/2).

5-4 Conclusions

Discovery of transparent ferromagnetism in the Co doped anatase thin films by an intensive combinatorial screening with SSQM. Further investigations, we found that Co doped anatase was ferromagnetic above room temperature, and Co doped rutile also shows ferromagnetism above room temperature. Magnetization of Co doped anatase and rutile was 0.3 μB/Co and 1.0 μB/Co, respectively. Structural characterizations and magnetic characterizations in detail are discussing in next Chapter 6.

Reference

[1] M. Murakami, Y. Matsumoto, and K. Nakjima, T. Makino and Y. Segawa, T. Chikyow and P. Ahmet, M. Kawasaki and H. Koinuma; Appl. Phys. Lett. **78** 18 2664-2666 (2001).

[2] Y. Matsumoto, Makoto Murakami, Z.W. Jin, A. Ohtomo, M. Lippmaa, M. Kawasaki, H. Koinuma; Jpn. J. Appl. Phys. **38** L603-L605 (1999)

[3] O. Chauvet, L. Forro, I. Kos, M. Miljak, Solid State Commun. **93**, 667 (1995).

[4] H. Ohno, Science **281**, 951 (1998).

[5] R. Wolfe, A. J. Kurtzig, R. C. LeCraw, J. Appl. Phys. **41** (no. 3), 1218 (1970).

[6] J. Q. Xiao, J. S. Jiang, C. L. Chien, Phys. Rev. Lett. **68**, 3749 (1992).

[7] S. Mitani, H. Fujimori, S. Ohnuma, J. Magn. Magn. Mater. **165**, 141 (1997).

[8] M. W. Chase Jr. et al., J. Phys. Chem. Ref. Data **14**, suppl. no. 1 (1985).

[9] S. Chen, M. G. Mason, H. J. Gysling, G. R. Paz-Pujalt, T. N. Blanton, T. Castro, K. M. Chen, C. P. Fictorie, W. L. Gladfelter, A. Franciosi, P. I. Chohen and J. F. Evans: J. Vac. Sci. & Technol. A **11** (1993) 2419.

Chapter 6 Structural and Magnetic Characterization of Titanium Dioxide Thin Films Doped with Cobalt

6-1 Introduction

In previous chapter, discovery of room temperature magnetism in Co doped TiO_2 thin films. This serendipitous discovery was resulted from the coupling of combinatorial synthesis of Co doped anatase library and high throughput screening of its magnetic property by a scanning SQUID. Now the origin of this magnetism is in controversy. In this chapter, structural and magnetic characterization of Co doped TiO_2 carefully.

A lot of efforts have been spent to discover novel DMS. In our laboratory, collaborators tried to fabricate DMS based on ZnO, In_2O_3, and SnO_2. However, ferromagnetic property couldn't be observed in these host materials. Jin et al. fabricated ZnO doped with 3d transition metals with combinatorial methods[1]. These samples didn't show ferromagnetic property. Only large MCD spectrum was observed in Co doped ZnO at low temperature (< 100K)[2,3]. Kimura et al. studied about Mn[4] and Co doped SnO_2 thin films. SnO_2 also has rutile type structure, but these samples also didn't show any ferromagnetic property. It is interesting point that ferromagnetic property is shown in Co doped TiO_2 not in SnO_2. There is something differences between these host materials. But it has not been clear.

We first reposted on ferromagnetism in TiO_2 doped with Co. After that, many groups have reported on Co doped TiO_2 are listed in table 1. S.A.Chambers *et al.* first[5] reproduced our results about ferromagnetic properties of Co doped anatase thin films. They fabricate Co

Table 1 Recent works on ferromagnetic properties on Co doped TiO_2 system.

Author	Method	Reference	
N.J. Seong et al.	MOCVD	Appl. Phys. Lett. 81 (2002) 4209-4211	○
S.A. Chambers et al.	OPA-MBE	Thin Solid Films 418 (2002) 197	○
S.A. Chambers et al.	OPA-MBE	Cond. Matter 0208315	○
S.A. Chambers et al.	OPA-MBE	Appl. Phys. Lett. 79 (2001) 3467-3469	○
D.H. Kim et al.	PLD	Appl. Phys. Lett. 81 (2002) 2421-2423	×
J.R. Simpson et al.	PLD	Cond. Matter 0205626	×
P.A. Stampe et al.	PLD	J. Appl. Phys. 52 (2002) 7114-7121	×
S.R. Shinde et al.	PLD	Cond. Matter 0203576	×
W.K. Park et al.	r-sputtering	J. Appl. Phys. 91 (2002) 8093-8095	○
Y.L. Soo et al.	Sol-gel	Appl. Phys. Lett. 81 (2002) 655-657	○
I.B. Shim et al.	spin coat	J. Appl. Phys. 91 (2002) 7941-7916	○
J.M. Sullivan et al.	Theory	Cond. Matter 0211614	○
M.S. Park et al.	Theory	Cond. Matter 0209253	○
M.S. Park et al.	Theory	Phys. Rev. B 65 (2002) 161201(R)	○

○: Co doped TiO_2 ferromagnetism
×: Co cluster ferromagnetism

doped anatase thin films on $SrTiO_3$ (001) substrate with optical plasma assisted molecular beam epitaxy, and they confirmed Co valence is 2+ in the film by x-ray absorption (XAS) and X-ray photoelectron spectroscopy (XPS) measurements. They show that ferromagnetic origin of Co doped anatase films are not produced by Co metal cluster. M.S. Park *et al.* theoretically supported our results[6]. They show that Co^{2+} ion can substitute Ti site stably, and ferromagnetic state is stable under oxygen vacancy is exist. On the other hands, some groups reported on Co cluster was observed on Co doped anatase film surface fabricated by PLD methods, and they argued that ferromagnetic origin of anatase films are produced by Co metal cluster[7,8]. From these points of view, structure and ferromagnetic origin of Co doped TiO_2 are confused. Therefore, structural characterization and magnetic characterization are discussing in detail on this chapter as follows.

6-2 Experimental

Pure and Co doped TiO_2 thin films were prepared by laser molecular beam epitaxy (LMBE) as mentioned in Section 5-3. Structural characterization of Co-doped TiO_2 films was investigated by x-ray diffraction (XRD) and high-resolution transmission electron microscope (HRTEM). And surface morphology was confirmed by scanning electron microscope (SEM). In addition, the fluorescence x-ray absorption fine structure (XAFS) measurements using synchrotron radiation (SR) were carried out in order to determine the local geometric and electronic structures around the doped Co atoms. The XAFS measurements were performed using the SR from the 2.5 GeV storage ring at the beam line BL12C of the Photon Factory in Tsukuba[9]**.** The XAFS spectra were measured with a Si (111) double crystal monochromator and a bent cylindrical mirror in the fluorescence-detection mode at 100K. The intensity of incident x-ray beams was monitored by a nitrogen-filled ionization chamber, while the fluorescence x-ray signals were detected by an array of 19 elements of Ge solid-state detectors.

Magneto-circular dichrorism (MCD) spectra were measured in a wavelength range from 200 nm to 800 nm with applying magnetic field up to 1 T along the light propagation direction (i.e. Faraday configuration) under a temperature from 20K to room temperature. Detail MCD concept is discussing in Appendix *II* - 1.

6-3 Results and discussions of Co doped anatase thin films

6-3-1 Structural characterizations

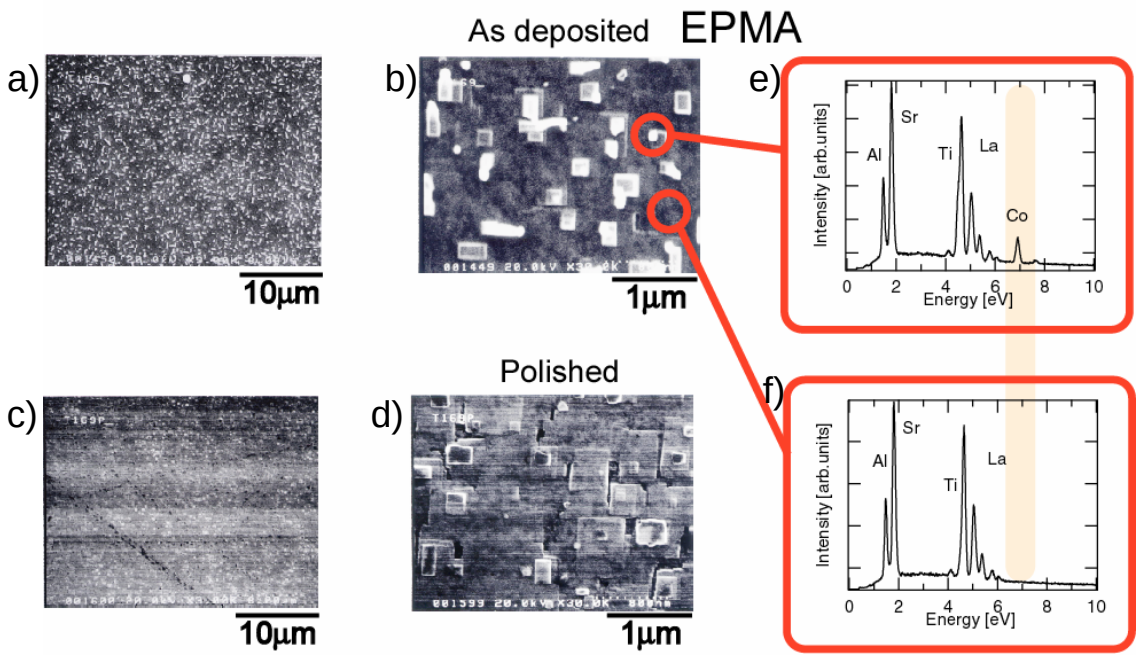

Fig. 6-1 SEM images of anatase thin films surface doped with Co 5% as deposited ((a) and (b)) and polished ((c) and (d)). Some particles with Co rich were observed on as deposited samples. Co contents were observed by EPMA. (e) and (f) shows EPMA results of as deposited samples with cluster and without cluster, respectively.

XRD results suggest that epitaxial (001) oriented anatase thin films doped with Co were grown on $SrTiO_3$, $LaAlO_3$ and $LaSrAlO_4$ single crystal oxide substrates without any second phases as shown in Fig. 3-6.

SEM images of Co 5% doped anatase thin films surface are shown in Fig. 6-1. With careful observation of surface structure of as deposited sample, I found out something cluster, which has rich Co content, on the film surface. The EPMA results show that high Co content was observed at the place with cluster shown in Fig. 6-1(e) and without cluster shown in Fig. 6-1(f). The cluster is easily removed by polishing the surface as clearly shown in Fig. 6-1(c) and Fig. 6-1(d). Comparing of MCD results between as deposited samples and removed sample are discussing in next section 6-3-2.

TEM images of Co doped anatase thin films fabricated on $LaSrAlO_4$ substrate are shown in Fig. 6-2. With careful observation, we also found that something cluster on the film surface. Two types of cluster were observed, one type is same structure of anatase film, and another one is different structure of anatase film. Diffraction pattern of different structure cluster are shown in inset of Fig. 6-2(b). Now we are trying to clear this structure, but now it

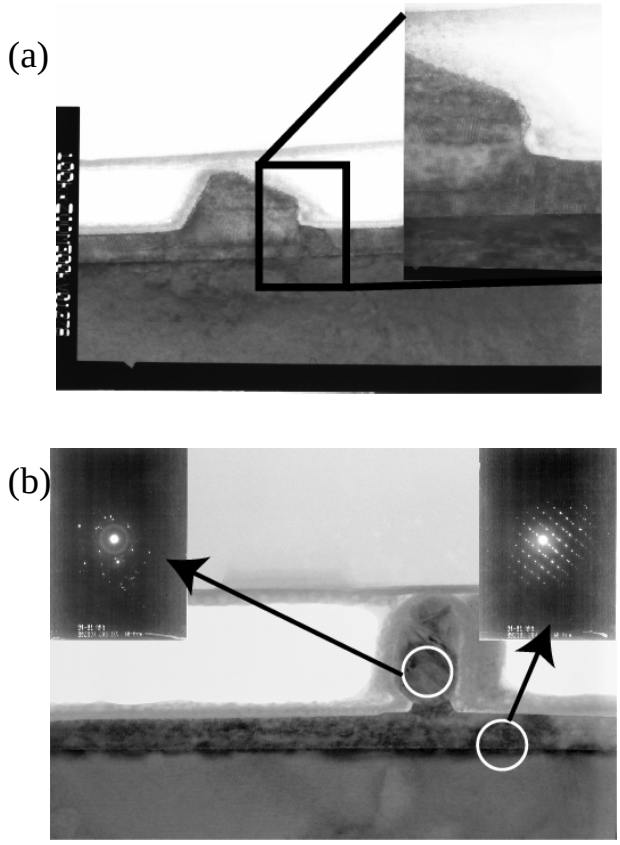

Fig. 6-2 TEM images of Co doped anatase thin films fabricated on $LaSrAlO_4$ substrate. Two types of cluster were observed, (a)same structure of anatase film and (b)different structure of anatase film. Diffraction pattern of different structure cluster are shown in inset of (b).

is not resolved.

To examine the local structure around the Co atoms in more detail, we measured Co *K*-edge x-ray absorption near edge structure (XANES) spectra. Figure 6-3 shows a typical XANES spectrum for Co doped anatase thin films of x = 0.06 and x = 0.08 on $LaAlO_3$, together with the spectra for several kinds of Co metal and Co oxides measured for comparison. Two types of spectra were observed in Co-doped anatase thin films. First one is x = 0.06 that the valence state of Co in the anatase film is not metallic. The result is consistent with the coexistence of divalent and trivalent Co ions in the film. Under the present film growth conditions (T_S = 650°C and P_{O2} = $1x10^{-6}$ Torr), Co should exist in divalent if the thermodynamic equilibrium is reached, whereas it should be trivalent after it is cooled to room temperature in oxygen. The divalent state could remain kinetically in the cooling process and be preserved at room temperature. On the other hands, second one is x = 0.08 that the valence state of Co in the anatase film is metallic. It is curious, if we think about film fabrication conditions.

Fig. 6-4 represents the Fourier transferred Co *K*-edge extended x-ray absorption fine structure (EXAFS) spectrum for the same Co doped anatase films (x = 0.06, 0.08). The spectra were curve fitted with the spectrum theoretically calculated using FEFF6[3]. From the comparison between the theoretical and experimental (x=0.06) spectra, Co ions substitute for

Ti sites and occupy the centers of distorted octahedrons with their coordination number of 6 ± 2. The nearest neighbor (NN) Co-O bond length was determined to be 2.07 ± 0.03 Å, which is slightly longer than the Ti-O bond length (1.91 A) in bulk anatase. No peak corresponding to the next nearest neighbor (NNN) Co-Ti bond length was observed. These results suggest that the Co ion substitution for Ti induces significant distortion in TiO_6 octahedron by the oxygen vacancies produced around Co ions to conserve the charge neutrality. On the other hands, Co segregated as metallic at x = 0.08. This metallic structure may consistent with cluster measured at film surface. We should study more about these structures.

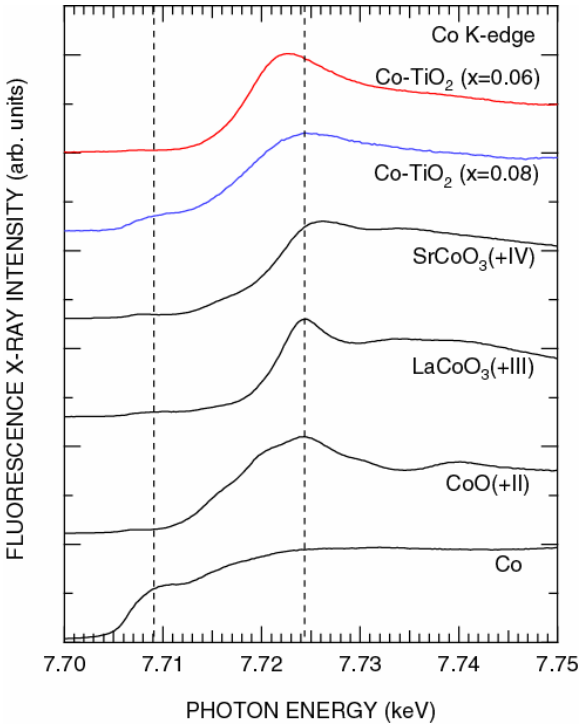

Fig. 6-3 Co *K*-edge XANES spectrum for Co doped anatase film (x=0.06, 0.08) with references for several kinds of Co metal and Co oxides.

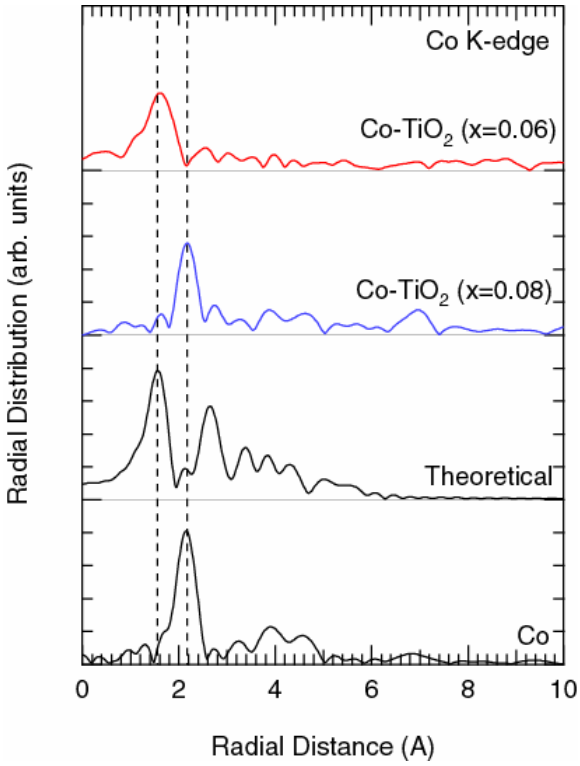

Fig. 6-4 Fourier transform of Co *K*-edge EXAFS oscillation function $k^2 \chi$ (k) spectrum for Co doped anatase film (x=0.06, 0.08) and Co with theoretical calculated spectrum, indicating the substitution of Co ions for Ti sites in the anatase film.

6-3-2 Magnetic Characterizations

Fig. 6-5 shows that MCD spectra of pure and Co 5% doped anatase thin films fabricated on $LaSrAlO_4$ (001) single crystal substrate. Blue line consistent with as deposited Co 5% doped anatase thin film, and red one consistent with polished sample after deposited Co 5% doped anatase thin film. MCD were measured at room temperature and magnetic field

H is 1T. The highest peaks of each spectrum are slightly different, but the small MCD position, which corresponding to band gap of anatase, is almost same. Temperature dependence of films couldn't be observed because the dir magnetic or paramagnetic component are increasing with decreasing of temperature. The magnetic filed dependence of MCD shows ferromagnetic as shown in fig. 6-5.

The MCD was decreased after polished surface of film. But MCD was also remained after polished sample. It may show that there were some ferromagnetic material on the surface, and after polished sample, some of them were removed. But the position observed MCD shows that MCD is related to film band structure. Further discussion are discussing in section 6-6 with the results of Co doped rutile films.

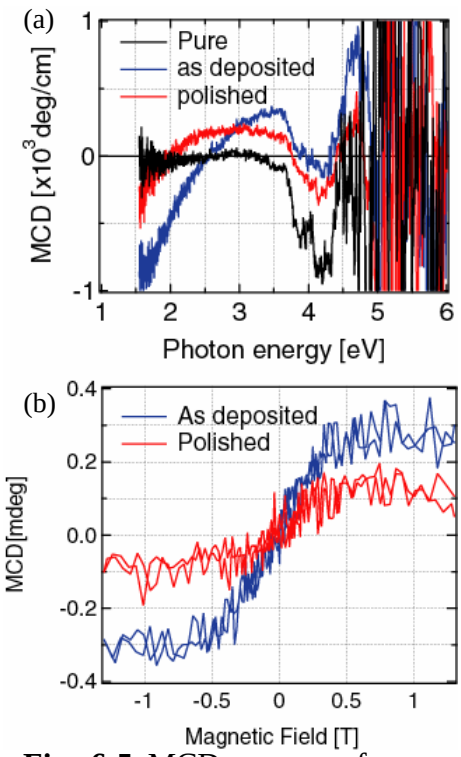

Fig. 6-5 MCD spectra of pure and Co doped anatase thin films on $LaSrAlO_4$ substrate. (a) MCD vs. photon energy. Pure anatase doesn't show any MCD but Co 5% doped anatase show clear MCD. (b) Magnetic field dependence of MCD spectra. Magnetic field dependence of MCD is ferromagnetic.

6-4 Co doped rutile thin films

6-4-1 Structural Characterizations

From the XRD measurements as mentioned in Section 5-3[10], epitaxial (101) oriented pure and Co 5% doped rutile thin films were grown on *a*-Al_2O_3 ($10\bar{1}2$) single substrate without second phase. Clear surface without segregation was also observed by SEM measurements.

Fig. 6-6 is a typical TEM image of $Co_xTi_{1-x}O_2$ film (x = 0.05) taken in a wide area (150 nm). No sign of segregation of impurity phase was confirmed on an atomic level. The inset is a lattice image of the film, indicating an excellent atomic arrangement identical to that of non-doped rutile film. And we also couldn't be observed any diffraction except film and

substrate diffraction.

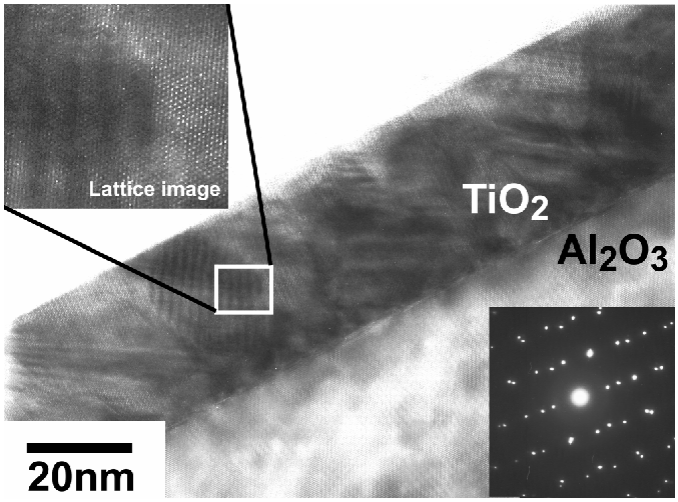

Fig. 6-6 Typical TEM image of $Co_xTi_{1-x}O_2$ film (x = 0.05) taken in a wide area (150 nm). No sign of segregation of impurity phase was confirmed on an atomic level. The inset is a lattice image of the film, indicating an excellent atomic arrangement identical to that of non-doped rutile film. And we also couldn't be observed any diffraction except film and substrate one.

To examine the local structure around the Co atoms in more detail, we measured Co *K*-edge x-ray absorption near edge structure (XANES) spectra. Fig. 6-7 shows a typical XANES spectrum for Co in the rutile films (a), together with the spectra of Co metal foil (b) and $CoTiO_3$ powder (c) measured for comparison. It is seen that the valence state of Co in the rutile film is metallic. The result isn't consistent with the thermodynamic equilibrium, which should be Co^{2+} or Co^{3+} in this growth condition (Ts = 700°C and P_{O2} = 1 x 10^{-6} Torr).

Fig. 6-8 represents the Fourier transferred Co *K*-edge extended x-ray absorption fine structure (EXAFS) spectrum for the same Co doped rutile film (x=0.05) (a) together with the spectra Co metal foil (b) and $CoTiO_3$ powder (c) measured for comparison. The spectrum was curve fitted with the spectrum theoretically calculated using FEFF6[11]. From the comparison between these experimental spectra, it is concluded that Co metal like spectra was observed. And also be observed small contribution from Co-O bond. From the XANES and EXAFS spectra, local structure around Co can be concluded that mixing of Co clustering and oxidative Co are existing in the film.

However, we couldn't be observed Co clustering from XRD, SEM and TEM measurements. It can be concluded that if something clustering is exist, the cluster size is enough small not to be observed from XRD, SEM, TEM measurements.

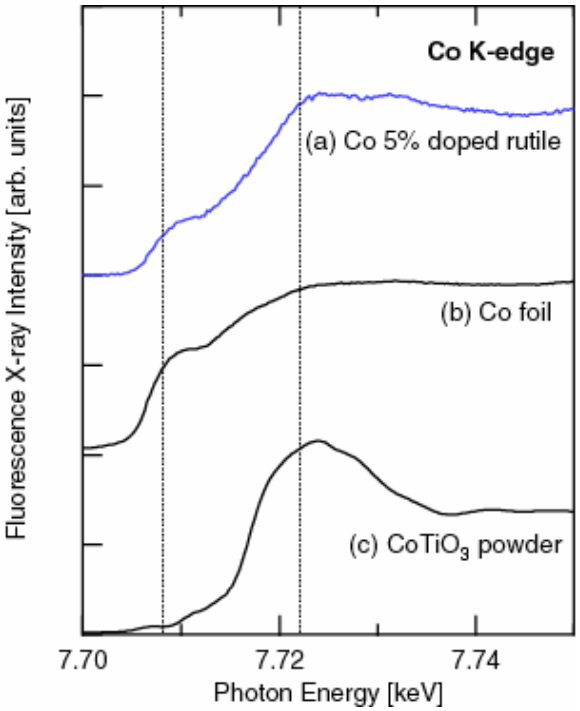

Fig. 6-7 Co *K*-edge XANES spectrum for Co doped rutile film (x=0.05) with references for several kinds of Co metal and Co oxides. Co foil like spectrum was observed.

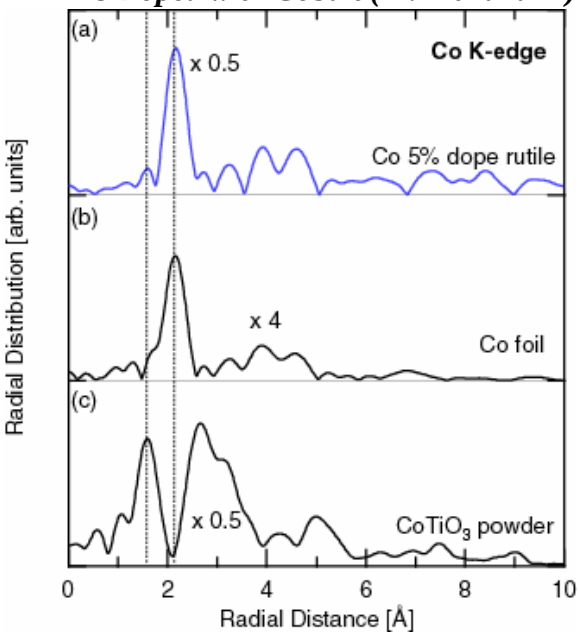

Fig. 6-8 Fourier transform of Co *K*-edge EXAFS oscillation function $k^2 \chi$ (k) spectrum for Co doped rutile film (x=0.05) with $CoTiO_3$ powder and Co foil spectra.

6-4-2 Magnetic Optical Characterizations

Fig. 6-9 (a) shows that absorption spectrum in Co 5% doped rutile 35 nm thick films fabricated at Ts = 750 °C and Po_2 = 1 x 10^{-6} Torr. Optical band gap, which is corresponding with the direct dipole transition from the initial state composed of $P\pi$ orbital of O to the final state composed of t_{2g} orbital of Ti, are clearly observed at 3.5 eV. Fig. 6-9 (b) – (e) shows MCD spectra of some rutile films, which various conditions and Co contents are different, at room temperature and magnetic field H is 1T. The conditions are shown in shoulder of each spectrum. The highest peaks of each spectrum are slightly different, but the small MCD position, which corresponding to band gap of rutile, is almost same. Temperature dependence and magnetic field dependence of MCD spectra, which is Co 5% doped rutile 35 nm thick films fabricated at T_S = 750°C and P_{O2} = 1 x 10^{-6} Torr, are similar shape as shown in Fig. 6-10. If the film contains magneto-optically active precipitates, the shape of MCD spectrum should change with H because of the different magnetic properties and different spectral shapes of Co doped rutile film and the precipitates. From these results suggest that observed spectra come from a single material, i.e., Co doped rutile, and the film is free from the magneto-optically active precipitates.

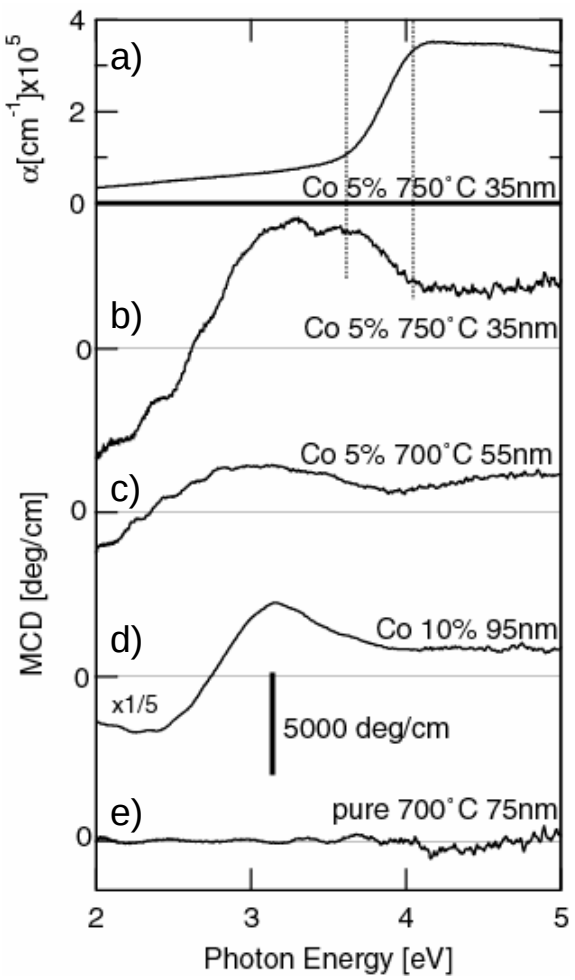

Fig. 6-9 (a) shows that absorption spectrum in Co 5% doped rutile 35 nm thick films fabricated at Ts = 750°C and P_{O2} = 1 x 10^{-6} Torr. Optical band gap, which is corresponding with the direct dipole transition from the initial state composed of *Pπ* orbital of O to the final state composed of t_{2g} orbital of Ti, are clearly observed at 3.5eV. (b) – (e) shows MCD spectra of some rutile films, which various conditions and Co contents are different, at room temperature and magnetic field *H* is 1T.

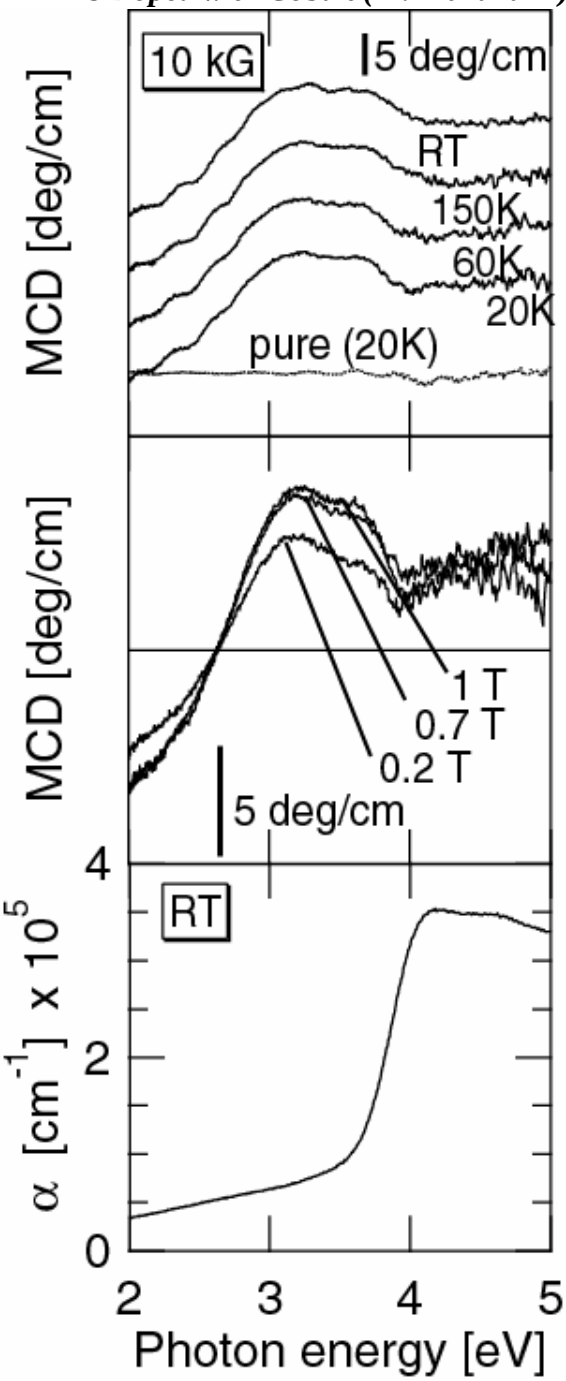

Fig. 6-10 Temperature dependence and magnetic field dependence of MCD spectra of Co 5% doped rutile 35 nm thick films fabricated at Ts = 750°C and P_{O2} = 1 x 10^{-6} Torr.

6-5 Combinatorial Fabrication and Characterization of Ti-Co-O Composition Spread System

$Ti_xCo_{1-x}O_{2-\delta}$ (x=0-1) compositional spread thin films with substrate temperature

gradient between 550°C and 750°C were grown on LSAO (001) single crystal substrate. The oxygen pressure was fixed at between 5×10^{-3} Torr and 5×10^{-7} Torr during the deposition. SSQM was used as a magnetic high throughput screening of magnetic properties of combinatorial libraries. Magnetization was increasing with decreasing of oxygen pressure. And the region, which magnetic domain structure could be observed, agrees with film conductive region. X-ray diffraction (XRD) was used as structural characterization. From the XRD measurements, *c*-axis oriented anatase thin films with undefined peak, which considered as rutile (210) or Co (111), were grown up to Co 50 %.

6-5-1 Experimental

We fabricated compositional spread $Ti_{1-x}Co_xO_2$ (x=0-1) thin films on a temperature gradient between 550°C and 750°C $LaSrAlO_4$ (LSAO) (001) substrate. The oxygen pressure was fixed at a pressure between 5×10^{-3} Torr and 5×10^{-7} Torr during the deposition. Two ceramics targets were switched synchronizing with the mask motion to deposit lower than one unit cell of the film during a period[12]. Ceramic targets TiO_2 and CoO were ablated by KrF excimer laser pulses alternately by switching the targets, while the moving masks were slid synchronously to give a linear gradient of x is $Ti_xCo_{1-x}O_{2-\delta}$ (as shown in section 2-2-2). Temperature gradient over the substrate were achieved by focusing Nd:YAG laser to the free standing end of the sample holder (as shown in section 2-2-3). By combination of the composition spread and temperature gradient along the two axes of the substrate, we also fabricated two-dimensional libraries as shown in Fig. 6-11 [13]. Structural characterization was achieved by conventional X-ray diffraction (XRD). Magnetic characterization was achieved by SSQM (as shown in section 2-3-2).

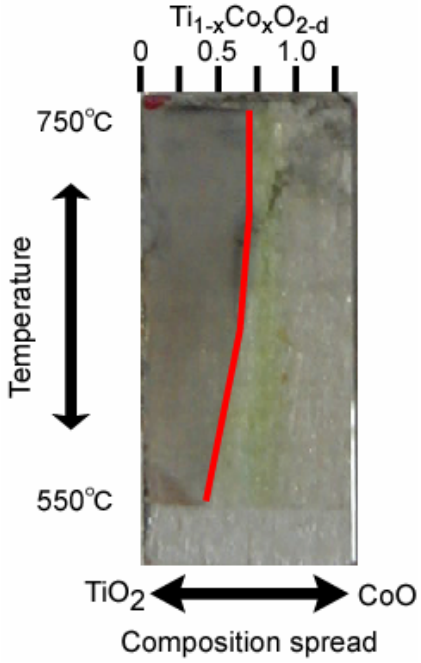

Fig. 6-11. $Ti_{1-x}Co_xO_{2-\delta}$ compositional spread libraries with temperature gradient between 550°C and 750°C. The red line shows line shows boundary between conductive (left side) and non-conductive (right side) film region.

6-5-2 Results and discussion

Fig. 6-11 shows the sample, which fabricated at 5×10^{-7} Torr. The red line indicates boundary between conductive and

non-conductive film region. The conductive region is increasing with fabrication temperature is higher.

Figure 6-12 shows line scans of magnetic domain structures measured by SSQM that that fabrication temperature versus sample positions as shown in fig. 6-11. The conditions were T_S = 550°C – 750°C and P_{O2} = 5×10^{-7} Torr. Blue dots line shows boundary between magnetic domains was observed and not observed. The line position shifted larger Co content when substrate temperature was increasing. And this blue dots line agreement with the red line as shown in fig. 6-11. The results suggest that ferromagnetism correspond to film conduction. It is clearly observed that magnetic signal appeared in wide range of Co contents, and we couldn't observe any magnetic signal at TiO_2 (x=0) and around CoO (x=1). These results suggest that the observed ferromagnetism is resulted from a cooperative interaction between Co and TiO_2.

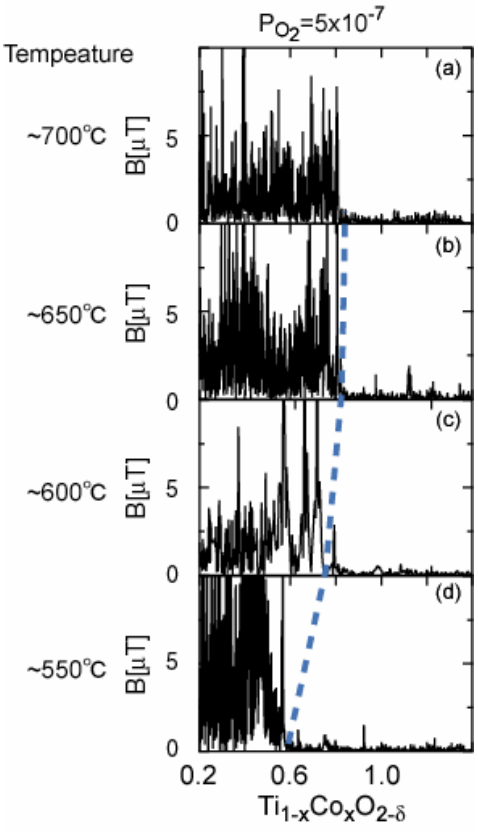

Fig. 6-12. Line scan of magnetic domain structures measured by SSQUID versus designed Co contents of $Ti_{1-x}Co_xO_{2-\delta}$ films fabricated at T_S = 550°C – 700°C and P_{O2} = 5 x 10^{-7} Torr.

Fig. 6-13 shows magnetic domain structures of combinatorial libraries fabricated at P_{O2} = 5×10^{-7} Torr measured by SSQM. Magnetic domain structures clearly observed up to Co contents about 50% at T_S = 750°C. Inset shows that magnetic domain structures of Co 10% (calculated) doped TiO_2 thin films fabricated at T_S = 750°C and P_{O2} = 5×10^{-7} Torr (a) and 5×10^{-5} Torr (b) during the deposition. We couldn't observe any magnetic domain structures in films fabricated at oxygen pressure higher than 5×10^{-5} Torr, and the magnetization was increasing with oxygen pressure was decreasing.

The *c*-axis oriented anatase thin film grown on LSAO substrate as same as on $SrTiO_3$ and $LaAlO_3$ substrates as shown in chapter 3. Fig. 6-14 shows the intensity plots of anatase (004), CoO (220), $CoTiO_3$ (012) and undefined phase, which has d = 2.04, per LSAO (009) measured by XRD. The exposed width was limited 1 mm by covering the film surface. The conditions were T_S ~ 650°C and P_{O2} = 5×10^{-7} Torr. The numbers of horizontal axis correspond to the number which shown in Fig. 1. We could observe anatase (004) peak up to around

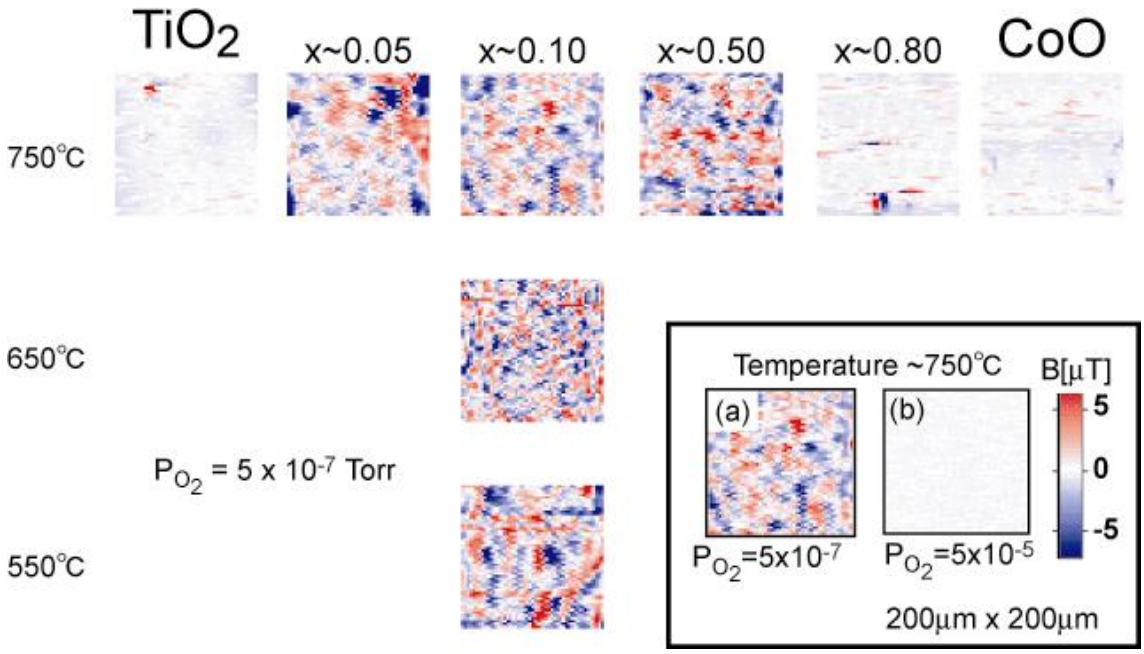

Fig. 6-13. Magnetic domain structures of $Ti_{1-x}Co_xO_{2-\delta}$ combinatorial libraries observed by SSQUID. Inset shows magnetic domain structures of Co 10 % (designed) doped TiO2 thin films fabricated at T_S = 750 °C and P_{O2} = 5 x 10^{-7} Torr (a) and 5 x 10^{-5} Torr (b).

x=0.5, and its intensity is decreasing with Co content is increasing. The position, which TiO_2 peak couldn't be observed and CoO peak could be observed, was the number 5. Around this region, the intensity of $CoTiO_3$ (012) was the strongest. The possibilities of undefined peak, which observed d=2.04, correspond to rutile (210) or Co (111). It seems that the magnetic property agree with this undefined peak. It is considered that undefined peak is rutile (210), because the tendency of intensity plots similar to anatase (004) peak and another observed rutile peak, and the peak was decreasing with Co content was increasing. To understand the magnetic origin of this system, we need to clear undefined phase.

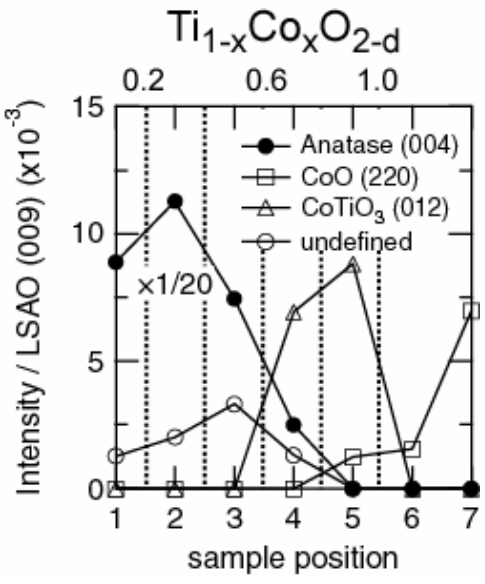

Fig. 6-14. The intensity plots of anatase (004) per LSAO (009) (left), and CoO (220), $CoTiO_3$ (012) and unknown phase, which has d = 2.04, per LSAO (009) (right) measured by XRD. The conditions were T_S ~ 650°C and P_{O2} = 5×10^{-7} Torr. The numbers of horizontal axis correspond with the number which shown in Fig. 6-11.

6-6 Total Discussion about Ferromagnetic Origin of Co Doped TiO_2

From these structural and magneto optical characterizations, we will discuss about ferromagnetic origin of Co doped TiO_2 thin films. In Co doped anatase thin films were observed Co rich contains cluster on the film surface. On the other hand, we couldn't observe any cluster in Co doped rutile thin films by SEM, XRD and TEM measurements.

However, Co has mixing valence in Co doped rutile thin films were measured from XANES and EXAFS spectra. The local structure of Co, measured by XANES and EXAFS, is similar to anatase of Co metal like sample. To clear magnetic origin of Co doped TiO_2 system, it seems that to clear magnetic origin of Co doped rutile is easier than that of Co doped anatase. Because Co doped rutile films were composed of single phase structurally. There are two possible structures in Co doped rutile, it means that Co metal like structure only or mixing of Co metal like structure and Co ions substitute for Ti sites and occupy the centers of distorted octahedrons with their coordination number of 6. In other words, Co doped TiO_2 systems are not single structure possibly indicated.

However, it was observed in previous paper that the crystallinity was improving and axis length was decreasing with doping Co contents were increasing in Co doped rutile. Can we say that Co was just segregated in the film? This data should suggest that Co ion existing with something special feature.

On the other hands, MCD data show that ferromagnetic properties are come from single component. And MCD spectra consistent with band structure of matrix material of rutile. From structural characterizations and MCD results, we propose 3 types of ferromagnetic mechanism in Co doped TiO_2 thin films. Possible mechanisms are that ferromagnetic property is produced by Co ions substitute for Ti sites (substitution type), Co metal cluster (cluster type), and relationships between ferromagnetic cluster such as Co metal and mother matrix of TiO_2 (relationships type). S. Chambers *et al.* were reported on about Co^{2+} ions substitute for Ti sites of anatase and ferromagnetic origin was produced by this substituted Co^{2+} ions. But, our Co doped anatase samples data, which MCD was decreasing after polished samples, suggest that ferromagnetism is small without cluster observed film surface, and these clusters posses rich Co. On the other hands, we couldn't observe any cluster in Co doped rutile thin films by XRD, SEM and TEM observations, but local structure measured by XAFS suggests that Co metal like material exist in films. To show ferromagnetic properties at room temperature, Co metal cluster size is needed larger than 10 nm. If such clusters exist in films we should find out these clusters by TEM measurements and so on.

That means that if something clusters exist in films, but these clusters size are smaller than that measured by TEM. Furthermore, considering with MCD results of Co doped rutile thin films, ferromagnetic properties are related to mother matrix of rutile. We suggested that ferromagnetic property of Co doped rutile is not simple cluster type ferromagnetism, is relationships type ferromagnetism.

6-7 Conclusion

Recent progressing of Co doped TiO_2 systems are discussed. Detail structural characterizations and magnetic characterizations of Co doped TiO_2 thin films were achieved by XRD, SEM, TEM, XAFS and MCD. In Co doped anatase thin films were observed Co rich contains cluster on the film surface. On the other hands, Co doped rutile thin films case, we couldn't observe any cluster in the film by XRD, SEM and TEM, but Co metal like spectra was observed by XAFS measurements. MCD spectra show that magnetic origin of the films come from single magnetic origin and correspond with TiO_2 band structure. Ferromagnetic origin of this system can be considered as three types, Co ions substitute for Ti sites (substitution type), Co metal cluster (cluster type), and relationships between ferromagnetic cluster such as Co metal and mother matrix of TiO_2 (relationships type). From our data suggest that ferromagnetic origin of Co doped rutile thin films are relationships type ferromagnetism. Furthermore, Co doped anatase case is also similar to Co doped rutile case because of similar magnetic properties and similar local structures of Co.

We also fabricated compositional spread $Ti_{1-x}Co_xO_2$ (x=0-1) thin films on a temperature gradient between 550°C and 750°C $LaSrAlO_4$ (001) substrate with the oxygen pressure was fixed at a pressure between 5×10^{-3} Torr and 5×10^{-7} Torr during the deposition. Based on structural and magnetic characterizations of $Ti_xCo_{1-x}O_{2-\delta}$ (x=0-1) wide range compositional spread and temperature gradient thin films, magnetic properties tendency of this system is being clear. It is considered that the magnetic property consistent with film conductivity and film structure. Magnetic domain structures were clearly observed in conductive film region not in non-conductive region. Through these combinatorial screenings, magnetic properties of $Ti_xCo_{1-x}O_{2-\delta}$ (x=0-1) was measured quickly.

Reference

[1] Z.W. Jin, T. Fukumura, M. Kawasaki, K. Ando and H. Saito, T. Sekiguchi, Y. Z. Yoo, M. Murakami, Y. Matsumoto, T. Hasegawa, H. Koinuma; Appl. Phys. Lett. **78** 24 3824-3826 (2001)

[2] K. Ando, H. Saito, Z.W. Jin, T. Fukumura, M. Kawasaki, Y. Matsumoto and H. Koinuma, J. Appl. Phys., 89 (2001) 7284-7286.

[3] K. Ando, H. Saito, Z.W. Jin, T. Fukumura, M. Kawasaki, Y. Matsumoto and H. Koinuma, Appl. Phys. Lett., 78 (2001) 2700-2702.

[4] H. Kimura, T. Fukumura, M. Kawasaki, K. Inaba, T. Hasegawa and H. Koinuma, Appl. Phys. Lett., 80 94-96

[5] S.A. Chambers, S. Thevuthasan, R.F.C. Farrow, R.F. Marks, J.U. Thiele, L. Folks, M.G. Samant, A.J. Kellock, N. Ruzycki, D.L. Ederer, U. Diebold, Appl. Phys. Lett. 79 (2001) 3467-3469.

[6] M.S. Park, S.K. Kwon and B.I. Min, Phys. Rev. B, 65, 161201(R)

[7] D.H. Kim, J.S. Yang, K.W. Lee, S.D. Bu, T.W. Noh, S.-J. Oh, Y.-W. Kim. J.-S. Chung, H. Tanaka, H.Y. Lee, and T. Kawai, Appl. Phys. Lett. 81 (2002) 2421-2423

[8] S.R. Shinde, S.B. Ogale, S. Das Sarma, S.E. Lofland, V.N. Kulkarni, J. Higgins, R.P. Sharma, R.L. Greene and T. Venkatesan, Cond. Matter 0203576

[9] S.I. Zabinsky, J.J. Rehr, A. Ankudinov, R.C. Albers and M.J. Eller, Phys. Rev. B 52 (1995) 2995

[10] Y. Matsumoto, R. Takahashi, M. Murakami, T. Koida, X. J. Fan, T. Hasegawa, T. Fukumura, M. Kawasaki, S. Koshihara, and H. Koinuma; Jpn. J. Appl. Phys. 40 pt2 11B L1204-L1206 (2001)

[11] FEFF6????

[12] T. Fukumura, Y. Okimoto, M. Ohtani, T. Kageyama, T. Koida, M. Kawasaki, T. Hasegawa, Y. Tokura, H. Koinuma, Appl. Surf. Sci. 189 (2002) 339.

[13] H. Minami, K. Itaka, P. Ahmet, D. Komiyama, T. Chikyow, M. Lippmaa, and H. Koinuma, Jpn. J. Appl. Phys. 41, (2002) L149.

Chapter 7 General Conclusion

Development of CLMBE apparatus was carried out with Mg doped ZnO and Eu doped Y_2O_3 systems. Then I succeeded in discover of room temperature ferromagnetism in Co doped titanium dioxide thin films with transparent in visible light region with combinatorial technique.

First, ZnO combinatorial samples doped with Mg were discussed. The bandgap is increasing and *c* - axis length is shortening quite linearly with increasing Mg content in the films. It can be concluded that the CLMBE technique provides not only high-throughput synthesis and screening, but can also be used to reduce statistical errors in experiments when the dependence of material properties on film composition or deposition conditions is studied.

Eu doped Y_2O_3 combinatorial thin films are also fabricated for the demonstration of CLMEB apparatus. It was clearly obtained that luminescence intensity calibrated by film thickness from Y_2O_3: Eu has a maximum peak around designed 5 mol% of Eu concentration. Brightness calibrated by film thickness has also a maximum peak around 5 mol%. These results agree with previous reports. These results were obtained by one fabrication run and one observation run. Through these results I succeeded in proofing that CLMBE technique is an excellent methods to development material science.

Then another combinatorial techniques and combinatorial characterizations were discussed. These techniques are expected to improve material science faster.

With these techniques, I investigated TiO_2. Structural control of TiO_2 thin films was achieved by lattice matching between films and substrates. Take advantage of this technology, I succeeded in fabricating the rutile / anatase bilayer films with completing orientations.

Furthermore, the crystallinity of epitaxial anatase thin films has been remarkably improved by using $LaAlO_3$ (001) substrates as well as by the optimization of the laser MBE conditions. Atomically-controlled layer-by-layer growth was verified for the first time on anatase thin films by the observation of clear RHEED intensity oscillation, thus enabling the further fabrication of anatase epitaxial nano films and their superlattices with other molecular layers.

Optical properties of strain free anatase epitaxial films were precisely determined by virtue of the lattice-matched transparent $LaAlO_3$ substrate. The high-quality anatase thin films are advantageous not only for practical application to optical devices but also for basic studies on electric, optical, and photocatalytic properties of TiO_2.

Fabrication and structural characterization of transition metals (TMs) doped TiO_2 were

discussed. More than 200 TiO_2 samples doped TMs were fabricated only in a few weeks. Solubility limit of TMs into anatase and rutile structures were systemically obtained.

Furthermore, photo-catalytic screening with two-dimensional pH imaging apparatus. Photo-catalytic activity differences of Co doped rutile on *c*-Al_2O_3 were clearly obtained with this method, but it was difficult to evaluate photo-catalytic activities of another combinatorial libraries quantitatively and reproducibly comparing.

Discovery of transparent ferromagnetism in the Co doped anatase thin films by an intensive combinatorial screening with scanning SQUID microscope. Further investigations, I found that Co doped anatase was ferromagnetic above room temperature, and Co doped rutile also shows ferromagnetism above room temperature. Magnetization of Co doped anatase and rutile was 0.3 μB/Co and 1.0 μB/Co, respectively.

Detail structural characterizations and magnetic characterizations of Co doped TiO_2 thin films were achieved by XRD, SEM, TEM, XAFS and MCD. In Co doped anatase thin films were observed Co rich contains cluster on the film surface. On the other hands, Co doped rutile thin films case, we couldn't observe any cluster in the film by XRD, SEM and TEM, but Co metal like spectra was observed by XAFS measurements. On the other hands, MCD spectra show that magnetic origin of the films came from single magnetic origin and correspond with TiO_2 band structure. Ferromagnetic origin of this system can be considered as three types, Co ions substitute for Ti sites (substitution type), Co metal cluster (cluster type), and relationships between ferromagnetic cluster such as Co metal and mother matrix of TiO_2 (relationships type). From our data suggest that ferromagnetic origin of Co doped rutile thin films are relationships type ferromagnetism. Furthermore, Co doped anatase case is also similar to Co doped rutile case because of similar magnetic properties and similar local structures of Co.

We also fabricated compositional spread $Ti_{1-x}Co_xO_2$ (x=0-1) thin films on a temperature gradient between 550°C and 750°C $LaSrAlO_4$ (001) substrate with the oxygen pressure was fixed at a pressure between 5×10^{-3} Torr and 5×10^{-7} Torr during the deposition. Based on structural and magnetic characterizations of $Ti_xCo_{1-x}O_{2-\delta}$ (x=0-1) wide range compositional spread and temperature gradient thin films, magnetic properties tendency of this system is being clear. It is considered that the magnetic property consistent with film conductivity and film structure. Magnetic domain structures were clearly observed in conductive film region not in non-conductive region. Through these combinatorial screenings, magnetic properties of $Ti_xCo_{1-x}O_{2-\delta}$ (x=0-1) was measured quickly.

Prospects

It is expected that material science will be more complex because of recent material science progress. Combinatorial technology will have a super power in material science field for the potential of this technology as discussed in this thesis. One of the good example for this reason is discovery of ferromagnetic oxide even above room temperature of Co doped TiO_2 through the combinatorial screening in this study. Through this study I could show that combinatorial chemistry is one of the excellent methods to discover novel material. This Co doped TiO_2 is also expected to be practical application which acts on also in room temperature, and more detail study will be needed for the application. Base technology to find out this Co doped TiO_2, structural control of TiO_2 with substrate template technique, will be important technology not only for studying Co doped TiO_2 but also studying about TiO_2 based condensed matter physics. Particularly, high quality anatase thin film fabricated on $LaAlO_3$ substrate has potential to study about anatase more detail in structure, optical property and so on because of it has been difficult to fabricate high quality anatase which has thermodynamically unstable phase.

Appendix *I* Fabrication of Epitaxial $Sr_xBa_{1-x}Nb_2O_6$ films

Appendix *I*–1 Introduction

Strontium barium niobate exhibits as a solid solution over a wide composition range [$Sr_xBa_{1-x}Nb_2O_6$ (SBN) $0.25<x<0.75$] (Fig. *I*-1). SBN shows tungsten-bronze type structure (Fig. *I*-2) in this composition region and has important ferroelectric properties. SBN has been studied because of the reason that has attracted properties, electro-optic, photo-refractive, pyro-electric and piezoelectric. There have been reported that these properties can be controlled by Sr/Ba ratio (Fig. *I*-3)[1]. Particularly, spontaneous polarization is along the *c*-axis, and largest electro-optical and dielectric coefficient at composition x=0.75. But these properties have been investigated mainly for single-crystal and polycrystaline ceramics. To make use of this profit, we tried to make *c*-axis oriented epitaxial SBN films on various oxide substrates, particularly on conductive Nb:$SrTiO_3$ (Nb=0.5%) substrate.

In this Appendix *I*, phase diagram of SBN system are discussing section *I*-2. Experimental are discussing in Section *I*-3. Single phase SBN fabrication on $SrTiO_3$ step substrate is discussing in section *I*-3-1, and compositional spread thin films on MgO are discussing is section *I*-3-2.

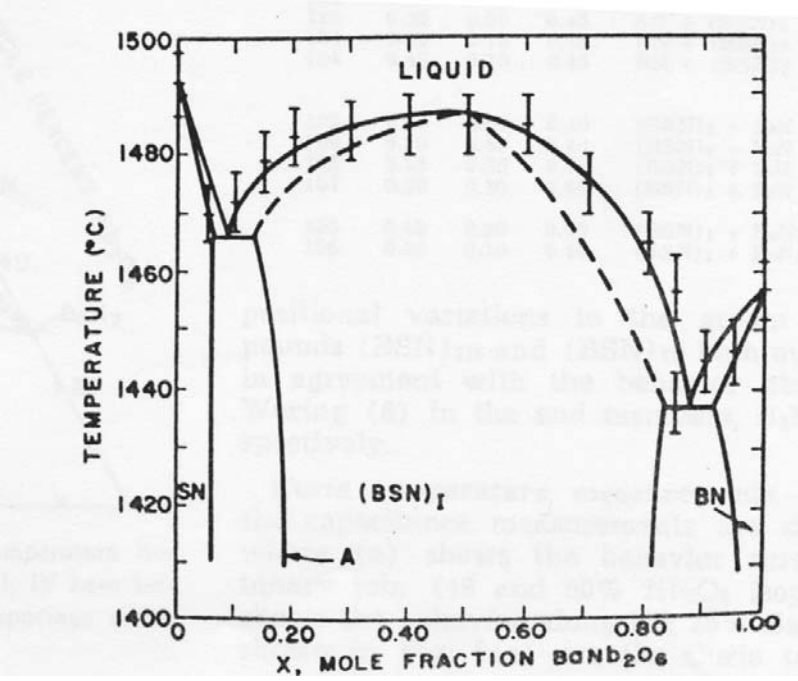

Fig. *I*-1 Pseudobinary phase equilibrium diagram for the system $SrNb_2O_6$ – $BaNb_2O_6$

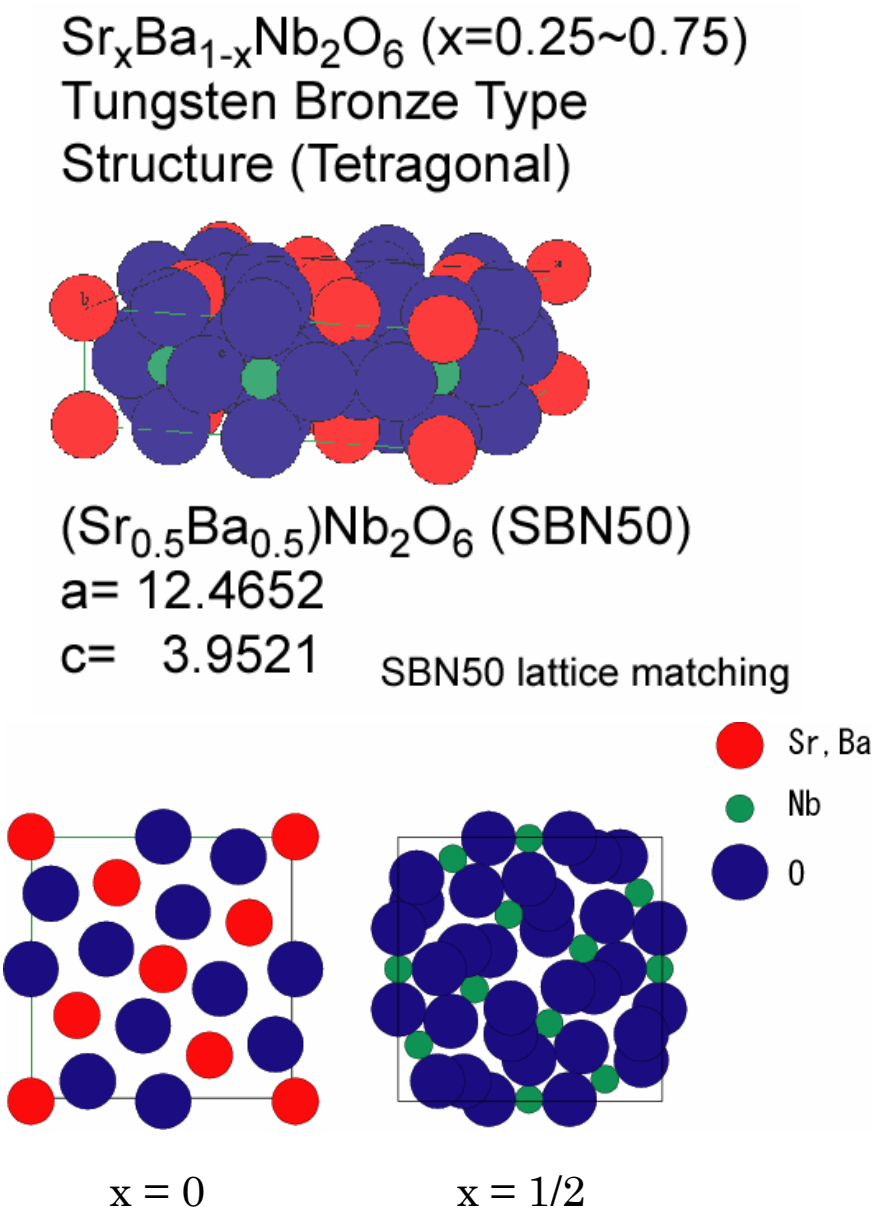

Fig. *I*-2 Crystal structure of tungsten bronze type $Sr_{0.5}Ba_{0.5}Nb_2O_6$ structure (tetragonal).

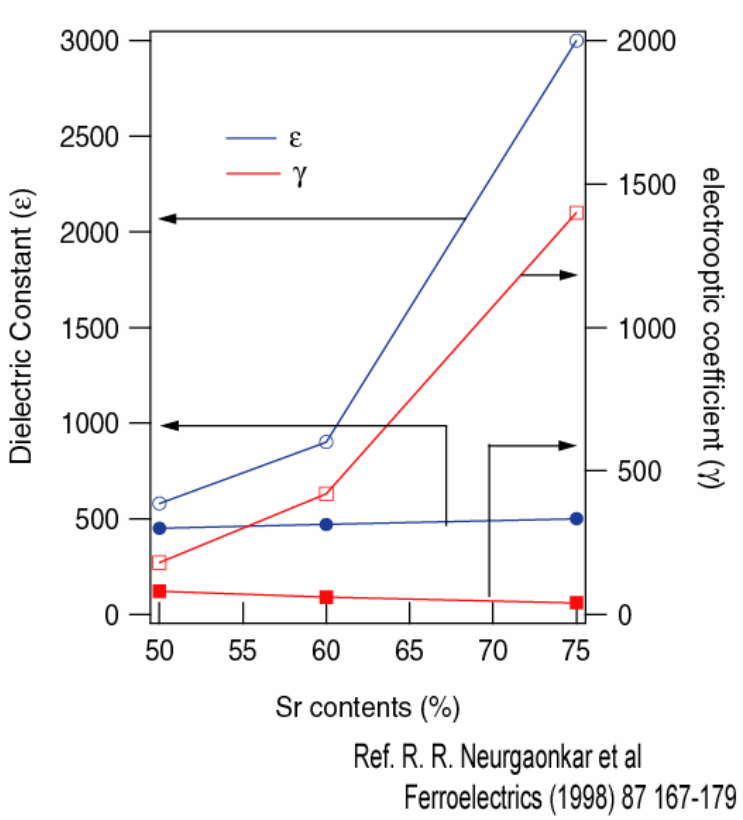

Fig. *I*-3 Dielectric constant (ε) and electric coefficient (γ) versus Sr contents (%). ε and γ are increasing with Sr contents are higher.

Appendix *I*–2 Phase diagram $SrNb_2O_6$ (SN)-$BaNb_2O_6$ (BN) pseudobinary system[2].

The differential thermal analysis (DTA) and x-ray results for the SN-BN binary join are shown in Fig. *I*-1. The structure of SBN is of the tetragonal tungsten bronze type. It is of some interest here to mention the reactivity problem encountered in this system. Attempts to produce a single-phase SBN by sintering at 1000°C failed completely. As the sintering temperature was progressively raised by 100°C increments to 1400°C, the single-phase field opened up starting with the BN-rich end. The solves line, A, in Fig. *I*-1 moved to the left and was located at 35% BN after sintering at 1400°C. The final location of solves line A at 20% BN was determined by melting these specimens on a platinum strip heater, slowly freezing under a microscope, and looking for second-phase SN lines with the Nonius-Guinier camera.

The liquid shown in Fig. *I*-1 is flat within experimental error over the composition range

20-60% BN. The location of the liquid maximum and associated congruently melting composition was determined with the aid of T_C measurements described later. The solid lines (shown as dashed lines) were located approximately using the composition shifts reported by Ballman and Brown[3] as guidelines and also the end-points of the eutectic arrest lines (which are observable by DTA).

Appendix *I*–3 Experimental

Thin films deposited in an oxygen pressure of ranged between 1 x 10^{-6} Torr and 1 x 10^{-2} Torr by impinging KrF excimer laser (λ=248 nm) pulses on a ceramic $Sr_xBa_{1-x}Nb_2O_6$ （x=0~1) target placed 5cm away from the substrate. Typical laser fluence and repetion rate were 0.5 J/cm^2 and 10Hz, respectively. The substrate temperature (*Ts*) was varied from 600 to 800°C. MgO, $SrTiO_3$, $LaAlO_3$ (001) cut oxide single crystal were used as a substrate.

Fabrication of combinatorial $Sr_xBa_{1-x}Nb_2O_6$ (x=0-0.75) films is used compositional spread technique mentioned in **section 2-2-2**. The conditions are used follows: Oxygen pressure and substrate temperature were P_{O2} = 10 mTorr and T_S = 680°C, respectively. The laser fluence and repetion rate were 0.5 J/cm^2 and 10 Hz, respectively.

Refraction high-energy electron diffraction (RHEED), X-ray diffraction (XRD), atomic force microscope (AFM), scanning electron microscope (SEM) are used as structural characterization. The current-voltage (I-V) characteristic of the SBN films was measured on the structure written in Figure *I*-4 using (apparatus). The capacitance measurements were done using (apparatus C-V). Dielectric properties of $Sr_xBa_{1-x}Nb_2O_6$ (x = 0 - 0.75) composition spread films were characterized by frequency shift by microwave microscope as shown in section 2.3.3.

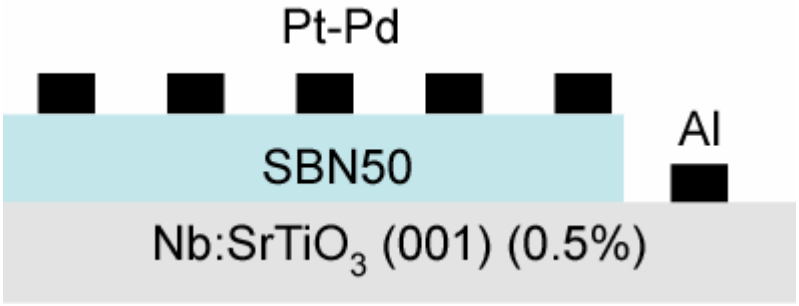

Fig. *I*-4 Schematic drawing of setting for current (I) – voltage (V) measurements and capacitance measurements. Al electrodes were used for Nb:STO (Nb=0.5%) contact and Pt-Pd electrodes were used for SBN 50 films contact.

Appendix *I*–4 Experimental results and discussion

Appendix *I*–4-1 Fabrication of $Sr_{0.5}Ba_{0.5}Nb_2O_6$ films on $SrTiO_3$ substrate

$Sr_{0.5}Ba_{0.5}Nb_2O_6$ (SBN 50) films were fabricated by temperature gradient combinatorial technique as discussed in Section 2-2-3. TiO_2 terminated step $SrTiO_3$ single crystal was used as a substrate[4]. Now, we call this substrate "step STO substrate".

Fig. *I*-5 shows XRD patterns of SBN 50 films at oxygen pressure P_{O2} = 10 mTorr and substrate temperature form 625 °C to 820 °C on step STO substrate. Objective (002) oriented SBN50 peak couldn't be observed at the temperature is lower than 620°C. And SBN (002) peak was clearly observed at the temperature is higher than 660°C, however, the peak was reduced at the temperature higher than 720°C. On the other hand, SBN (410) second phase peak could be observed at the temperature higher than 660°C, and the peak grown when temperature is higher. The full width at half maximum (FWHM) of the SBN (002) peak rocking curve were plotted against temperature shown in Fig. *I*-6 (a). The FWHM of rocking curve reduced when substrate temperature went higher. The ratio of SBN50 (002) and STO (002) peak [SBN (002) / STO (002)], SBN50 (002) and SBN50 (410) peak [SBN50 (002) / SBN50 (410)] were plotted against temperature as shown in Fig. *I*-6(b). SBN (002) / STO (002) ratio has a peak maximum around 680°C, and decreasing when temperature is higher. On the other hands, SBN (002) / SBN (410) ratio was decreasing when temperature is higher.

From these results, it can be concluded that fabrication of only *c*-axis oriented SBN50 films on step $SrTiO_3$ substrate is difficult.

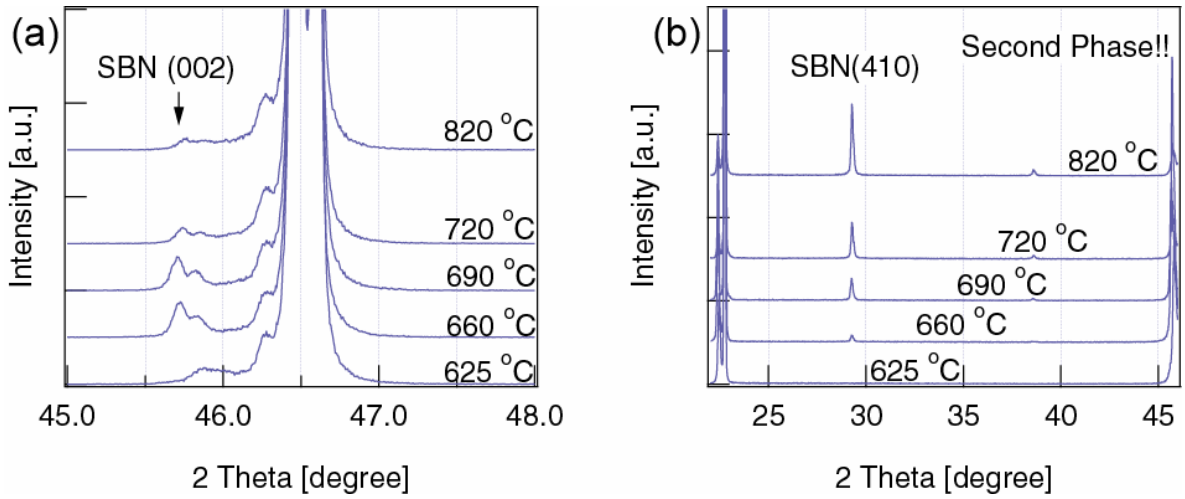

Fig. *I*-5 XRD patterns of $Sr_{0.5}Ba_{0.5}Nb_2O_6$ films on step $SrTiO_3$ (001) at substrate temperature between 625°C and 820°C around $SrTiO_3$ (002) peak (a) and between $SrTiO_3$ (001) and $SrTiO_3$ (002) peaks.

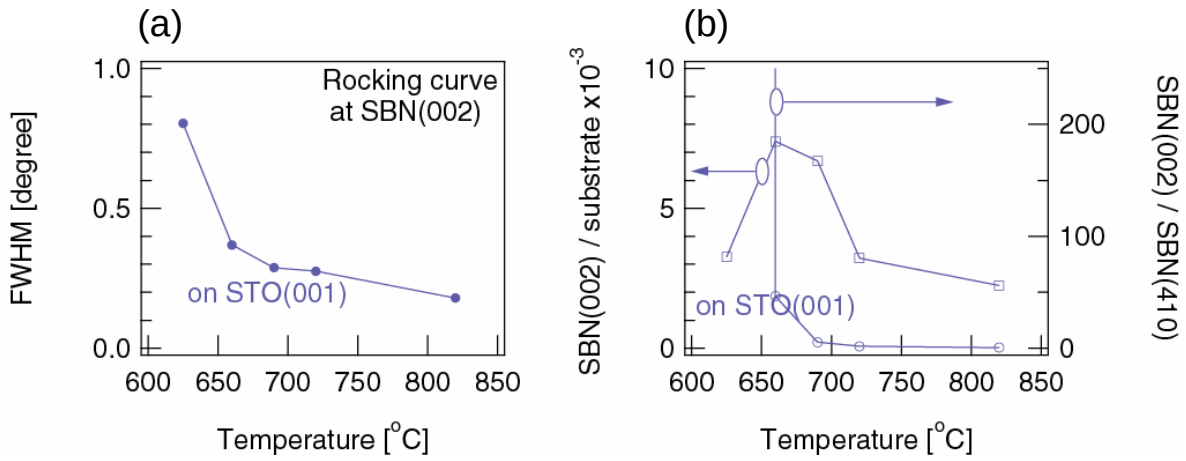

Fig. *I*-6 (a) The differences of FWHM rocking curve at $Sr_{0.5}Ba_{0.5}Nb_2O_6$ (002) peak against substrate temperature. (b) The ratio of peak intensity of $Sr_{0.5}Ba_{0.5}Nb_2O_6$ (002) against that of SrTiO3 (002) (left) and $Sr_{0.5}Ba_{0.5}Nb_2O_6$ (410) (right) are plotted with substrate temperature.

Fig. *I*-7 shows that AFM images and RHEED patterns which after deposited SBN50 films on step STO substrate at oxygen pressure was P_{O2} = 10 mTorr and temperature between 625°C and 820°C, respectively. Needle like structure, growing (100) and (010) direction of STO, were observed by AFM in the sample fabricated at higher temperature. However, flat surface was observed in the sample fabricated at lower temperature. Together with XRD results, it is considered that the structures, which were observed at high temperature, were consistent with SBN (410) phase, and the structures, which were observed lower temperature, were consistent with objective SBN (002) phase. Likewise, observed structure observed at 720°C, SBN (410) phase were grown at initial stage of SBN growing. That is, controlling of initial growth of SBN made us to fabricate epitaxial SBN (002) thin films without SBN (410) second phase. So we tried to fabricate SBN 50 films on A-site terminated STO substrate.

The oscillatory behavior of the specular beam spot intensity in the RHEED pattern was observed as shown in Fig. *I*-8 during the deposition of SrO_2 and BaO_2 on step STO substrate. Under the conditions of Po_2 = 1x10^{-5} Torr and *Ts* = 650 °C the SrO_2 and BaO_2 film grew in a layer-by-layer fashion as noted by the streaky RHEED pattern. Through this procedure, A-site terminated STO substrate was prepared. Now, we call this substrate "A-site terminated STO substrate".

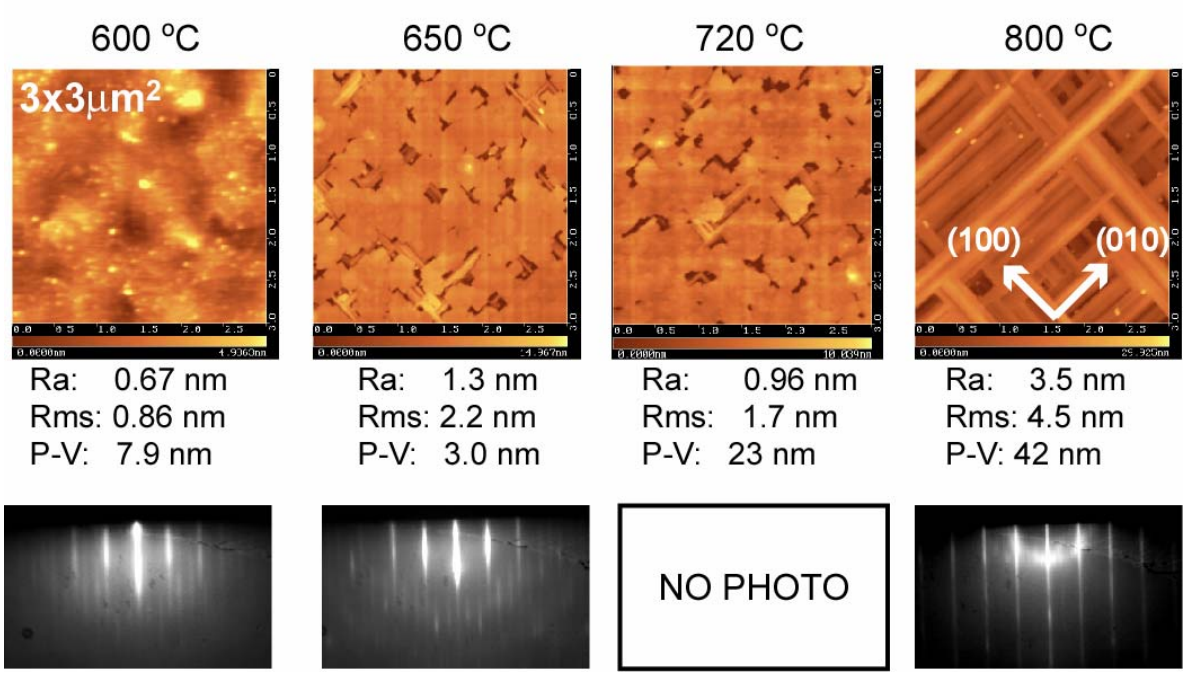

Fig. *I*-7 AFM images and RHEED images of $Sr_{0.5}Ba_{0.5}Nb_2O_6$ films on step $SrTiO_3$ (001) at substrate temperature between 600 °C and 800 °C.

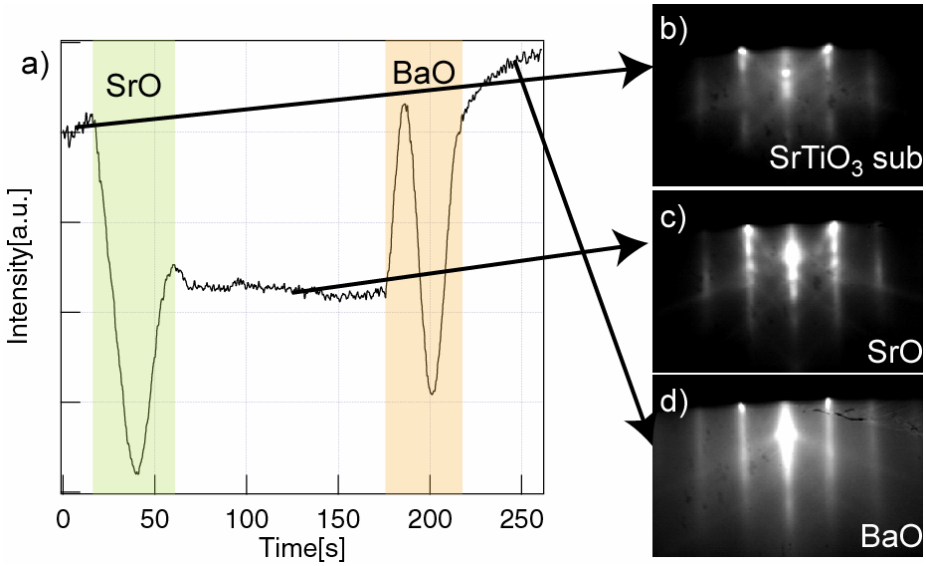

Fig. *I*-8 The oscillatory behavior of the specular beam spot intensity in the RHEED pattern. RHEED images of $SrTiO_3$ substrate (b), after deposited SrO (c) and after deposited BaO (d) are shown.

Fig. *I*-9 shows XRD patterns of SBN 50 films at substrate temperature form 625 °C to 820 °C on A-site terminated STO substrate. Objective (002) oriented SBN50 peak could be observed at every temperature region. And, SBN (410) second phase peak could be observed at the temperature higher than 750°C, and the peak grown when temperature is higher. The FWHM of the SBN (002) peak rocking curve were plotted against temperature shown in Fig. *I*-10(a). The FWHM of rocking curve reduced when substrate temperature went higher. The ratio of SBN50 (002) and STO (002) peak [SBN (002) / STO (002)], SBN50 (002) and SBN50 (410) peak [SBN50 (002) / SBN50 (410)] were plotted against temperature as shown in Fig. *I*-10 (b). SBN (002) / STO (002) ratio was decreasing when temperature is higher. On the other hands, SBN (002) / SBN (410) ratio was decreasing when temperature is higher.

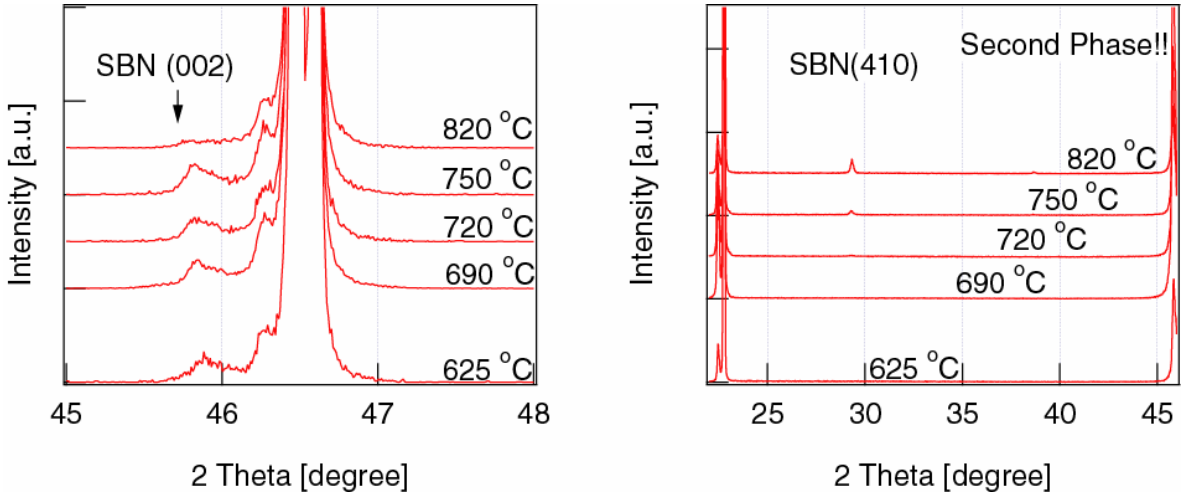

Fig. *I*-9 XRD patterns of $Sr_{0.5}Ba_{0.5}Nb_2O_6$ films on BaO/SrO/$SrTiO_3$ (001) at substrate temperature between 625°C and 820°C around $SrTiO_3$ (002) peak (a) and between $SrTiO_3$ (001) and $SrTiO_3$ (002) peaks.

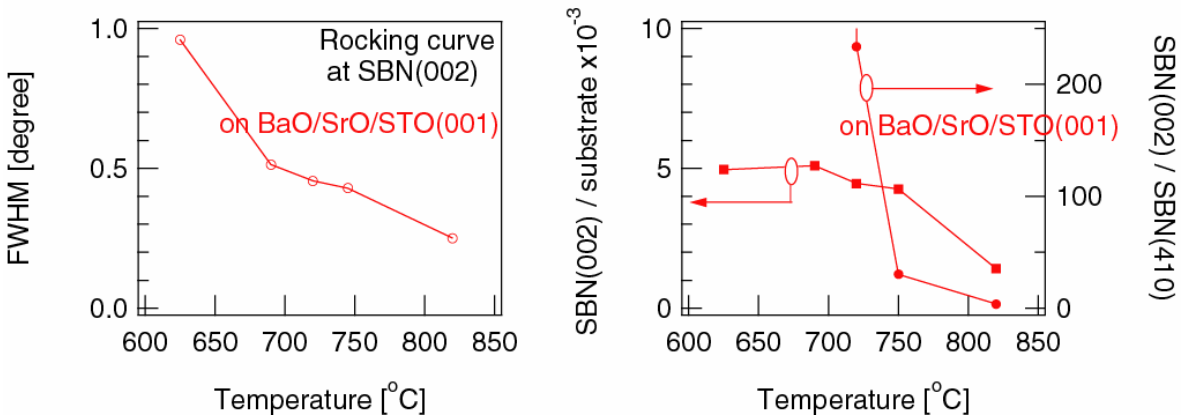

Fig. *I*-10 (a) The differences of FWHM rocking curve at $Sr_{0.5}Ba_{0.5}Nb_2O_6$ (002) peak against substrate temperature. (b) The ratio of peak intensity of $Sr_{0.5}Ba_{0.5}Nb_2O_6$ (002) against that of $SrTiO_3$ (002) (left) and $Sr_{0.5}Ba_{0.5}Nb_2O_6$ (410) (right) are plotted with substrate temperature. BaO/SrO/$SrTiO_3$ (001) was used as a substrate.

Comparison between on step STO and A-site terminated STO substrate of FWHM of SBN (002) peak and peak ratio of [SBN (002) / STO (002)] and [SBN50 (002) / SBN50 (410)] are shown in Fig. *I*-11. There were trend that FWHM value of on step STO substrate was smaller than that of on A-site terminated STO. The peak ratios of [SBN (002) / STO (002)] were almost same on these substrates, and that of [SBN50 (002) / SBN50 (410)] on step STO substrate was smaller than that on A-site terminated substrate. From these XRD results, it can be concluded that epitaxial SBN (002) thin films were grown on A-site terminated on STO substrate. AFM images, which are shown in Fig. *I*-12, were also supported this result.

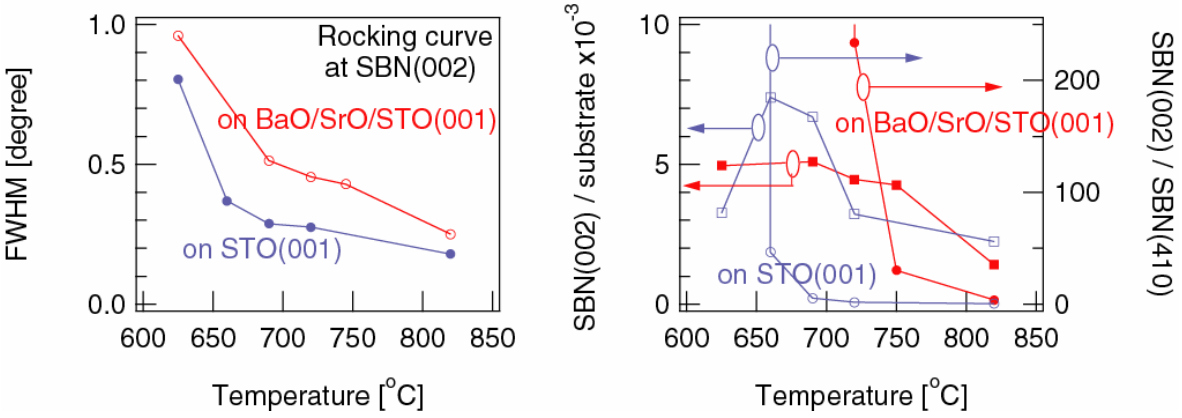

Fig. *I*-11 (a) The differences of FWHM rocking curve at $Sr_{0.5}Ba_{0.5}Nb_2O_6$ (002) peak against substrate temperature. (b) The ratio of peak intensity of $Sr_{0.5}Ba_{0.5}Nb_2O_6$ (002) against that of $SrTiO_3$ (002) (left) and $Sr_{0.5}Ba_{0.5}Nb_2O_6$ (410) (right) are plotted with substrate temperature. BaO/SrO/$SrTiO_3$(001) was used as a substrate.

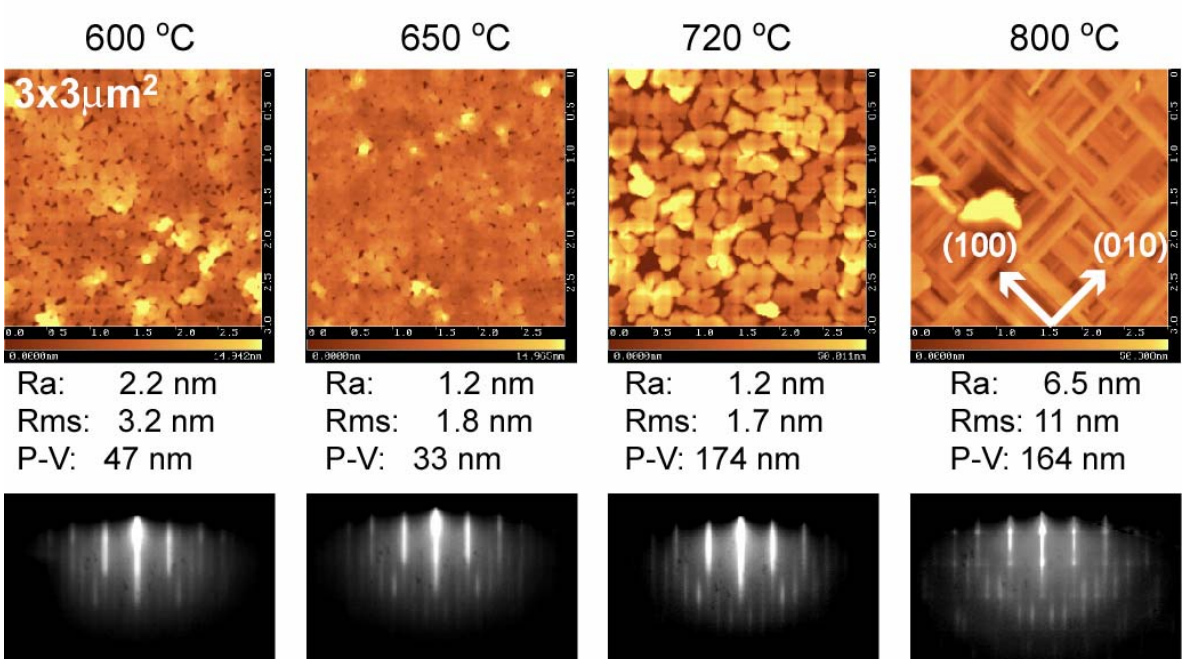

Fig. *I*-12 AFM images and RHEED images of $Sr_{0.5}Ba_{0.5}Nb_2O_6$ films on step $SrTiO_3$ (001) at substrate temperature between 600°C and 800°C.

Appendix *I*-4-2 Fabrication of SBN 50 films on various oxide substrates

$SrxBa_{1-x}Nb_2O_6$ (x = 0 - 0.75) films are fabricated on MgO (001), $SrTiO_3$ (STO) (001) and $LaAlO_3$ (LAO) (001) substrates, which lattice constants are 4.211, 3.905 and 3.792. The XRD patterns of SBN50 films fabricated on MgO (001), STO (001) and LAO (001) fabricated at P_{O2} = 10 mTorr and Ts = 680°C are shown in Fig. *I*-13 (a). The temperature range between 650°C and 700°C *c*-axis oriented SBN50 films were grown on these substrates. However, we couldn't observe any peak when the substrate temperature was lower than 600 °C, and SBN (410) phase were strongly observed when the substrate temperature was higher than 750°C.

The FWHM of the SBN (002) peak rocking curve fabricated on MgO, STO, LAO are shown in Fig. *I*-13 (b). The lowest value of STO is 0.46, and the value of MgO and LAO are 0.80 and 0.75, respectively. These differences between these values are considered as the difference of lattice matching between films and substrates as shown in table *I*-1.

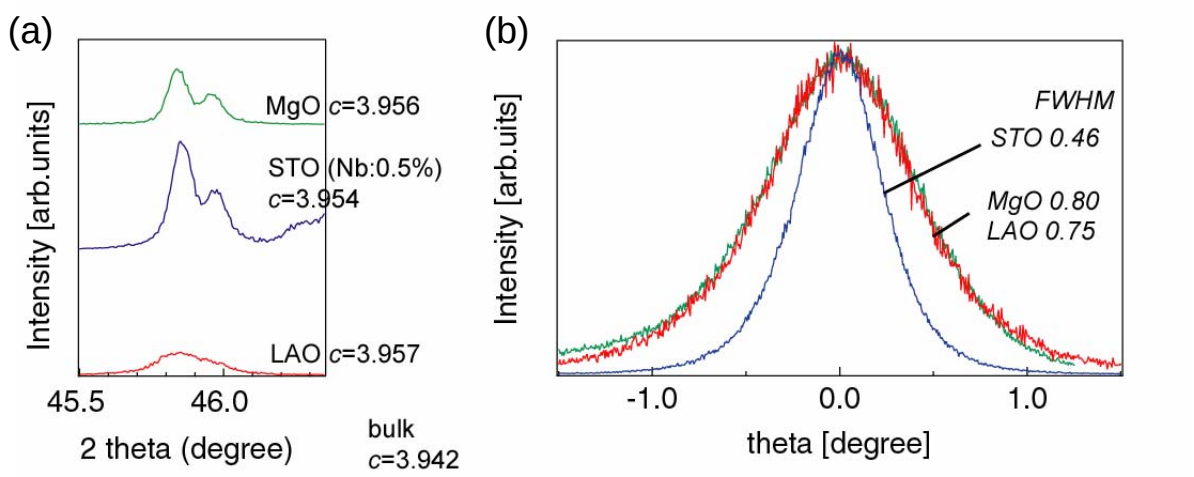

Fig. *I*-13 (a) The XRD patterns of SBN50 films fabricated on MgO (001), $SrTiO_3$ (001) and $LaAlO_3$ (001) fabricated at P_{O2} = 10 mTorr and Ts = 680°C. (b) The FWHM of the SBN (002) peak rocking curve fabricated on MgO, $SrTiO_3$, $LaAlO_3$

Table *I*-1 Lattice matching between substrates and SBN 50 film

	a	$\sqrt{10}$a	matching (%)
STO	3.905	12.349	+0.947
LaO	3.792	11.991	+3.95
MgO	4.211	13.316	−6.38

To confirm the epitaxial relationships between films and substrates, four circles XRD are employed shown in Fig. *I*-14. The SBN thin film exhibits antiphase domains in the *c*-plane, aligned at same direction and at 36.8° and 36.4° with respect to the reflections from the STO (100) and LAO (100) planes, respectively. From these data, the epitaxial relationship between SBN and substrates can be described as SBN <100> // STO <310> and SBN <100> // LAO <310> (Fig. *I*-15). On the other hands, SBN films on MgO have another two domains measured at STO and LAO substrates.

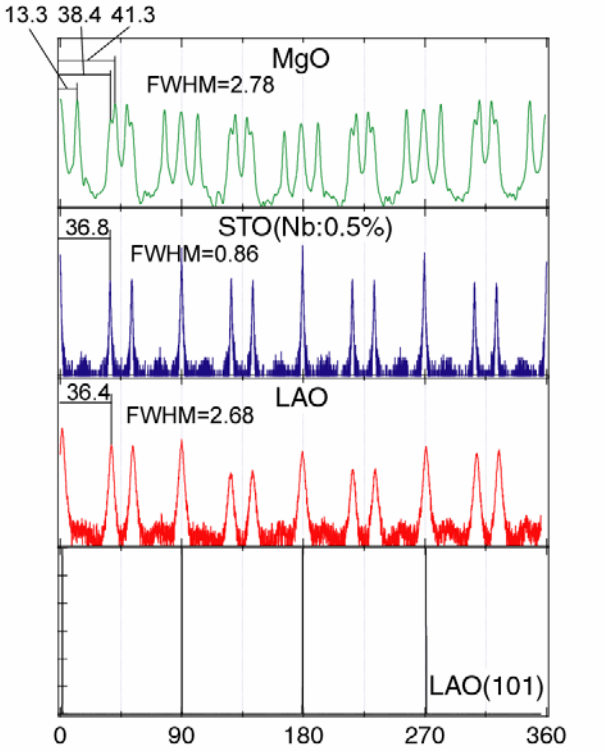

Fig. *I*-14 Phi scans of SBN (310) and LaAlO3 (101). SBN films were fabricated on MgO, $SrTiO_3$ and $LaAlO_3$.

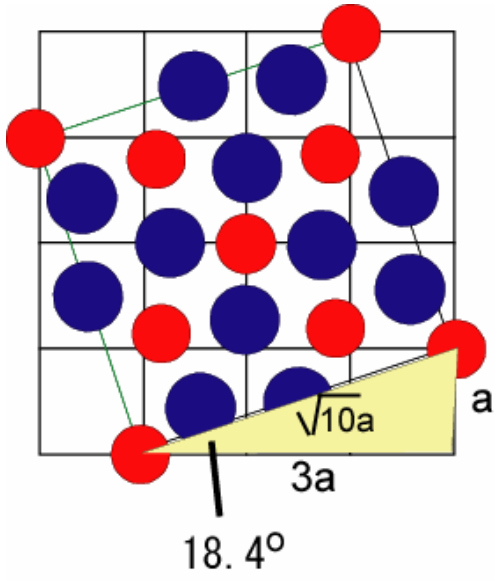

Fig. *I*-15 Schematic unit cell configurations of SBN and substrates.

Appendix *I*-4-3 Fabrication $Sr_xBa_{1-x}Nb_2O_6$ (x = 0.25–1.0) composition spread films and characterization of dielectric properties by scanning microwave prove apparatus.

Furthermore, $Sr_xBa_{1-x}Nb_2O_6$ (x = 0.25 – 1.0) composition thin films were fabricated on MgO substrate. Fabrication procedure of composition thin films were discussed in section 2-2-2. The reasons why $Sr_xBa_{1-x}Nb_2O_6$ (x = 0.25 – 1.0) composition thin films were fabricated on MgO substrate are to confirm the composition of SBN and to measure frequency shift of films with microwave microscope as mentioned in section 2-3-2. Fig. *I*-16 (a) shows the XRD results of compositional spread thin films of $Sr_xBa_{1-x}Nb_2O_6$ (x = 0.25 – 1.0) by combinatorial XRD apparatus as mentioned in section 2-3-4. The 2θ values of SBN (002) peaks are shifted larger with Sr contents are higher. This data suggests that $Sr_xBa_{1-x}Nb_2O_6$ (x = 0.25 – 1.0) composition films are epitaxialy grown on MgO substrates. Fig. *I*-16 (b) shows the relative frequency shift measured by microwave microscope. The peak maximum of value is observed around x = 0.65 little difference from reported maximum. But we succeeded in characterize dielectric properties of compositional spread $Sr_xBa_{1-x}Nb_2O_6$ (x = 0.25 – 1.0) films in a one

run.

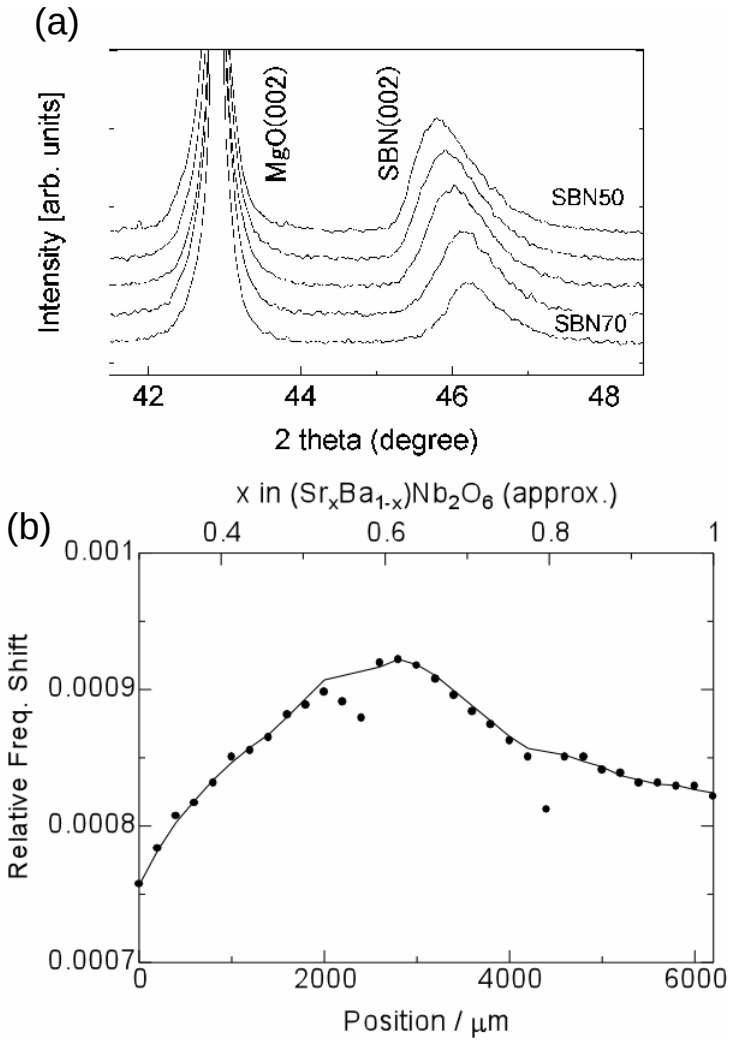

Fig. *I*-16 (a) XRD results of compositional spread thin films of $Sr_xBa_{1-x}Nb_2O_6$ (x = 0.25 – 1.0). The 2θ values of SBN (002) peaks are shifted larger with Sr contents are higher. (b) The relative frequency shift measured by microwave microscope. The peak maximum of value is observed around x = 0.65 little difference

Appendix *I*-4-4 Electrical properties characterization with I-V and C-V measurements

The current-voltage (I - V) characteristic and the capacitance measurements (C - V) were achieved by the configuration as mentioned in Fig. *I*-4 of appendix section *I*-3. The SBN 50 films were fabricated on SrO and BaO buffered Nb:STO (Nb = 0.5%) (BaO/SrO/Nb:STO) substrate at Po_2 = 10 mTorr, Ts = 720 °C.

Fig. *I*-17 shows electrical properties of SBN 50 films by I-V and C-V measurements. Fig. *I*-17 (a) shows dielectric constant versus Bias voltage (V), and Fig. *I*-17 (b) shows tangent δ (tan δ) versus bias voltage (V) measured by C-V measurements. From the characteristic of tan δ is too high for a dielectric material, and larger ε was observed reported one. These results can be easily understood from the data of I – V characteristic as shown in Fig. *I*-17 (c). Fig. *I*-17 (c) shows leak current [A/cm^2] versus applied voltage [MV/cm]. Large leak current, from 10^{-5} to 10^{-2} A/cm^2, was observed. Two reasons are can be considered as such a large leak current character. One thing is that leak pass through the film defect such as domain boundary. Another one is that intrinsic properties of film or stoichiometric defects. First one is ruled out from the observations of surface and cross-sectional structures of films as shown in Fig. *I*-18. Fig. *I*-18 (a) shows AFM image of SBN 50 film fabricated on Nb:STO (Nb:0.5%), and Fig. *I*-18 (b) and Fig. *I*-18(c) show the cross-sectional SEM image of SBN film. Clear surface and dense columnar were clearly observed. Furthermore, we tried to anneal the film in high oxygen pressure (5×10^5 Pa) at 500°C. The leak current was decreasing little, but not so much improvement was observed. Fabrication of SBN films at higher oxygen pressure or doping some elements to compensate the defects will be needed to improve the dielectric properties of SBN films.

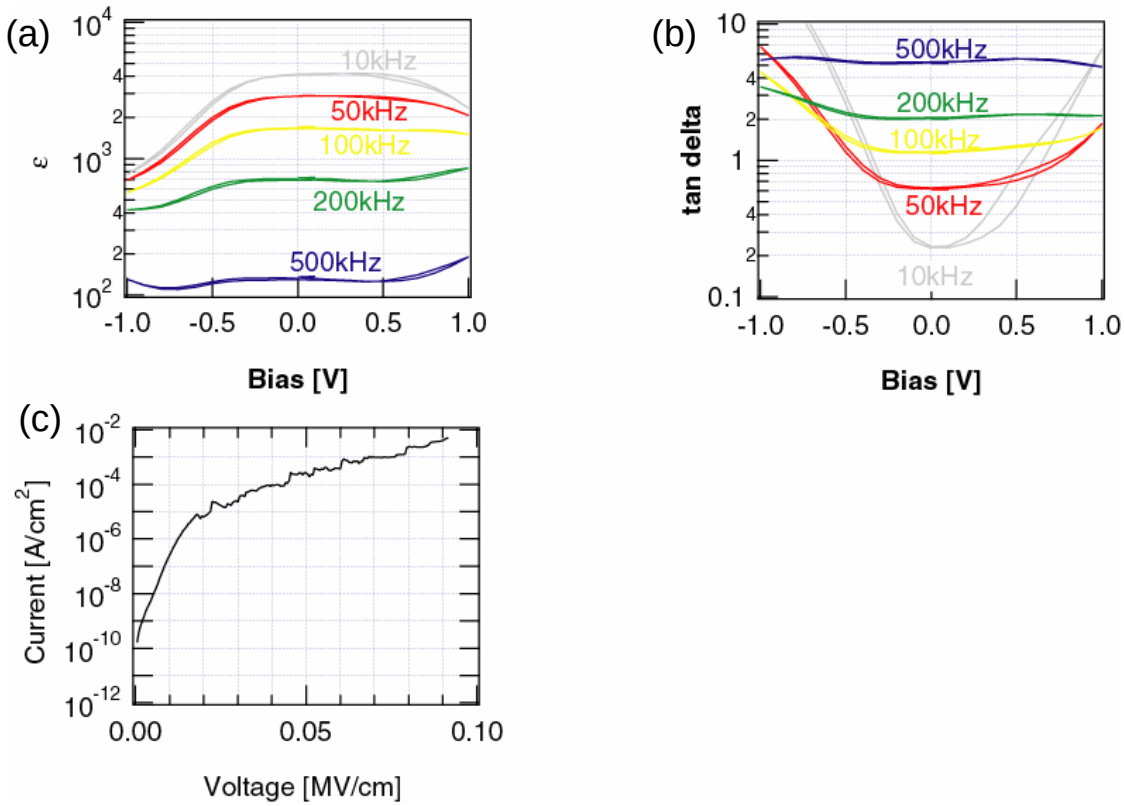

Fig. *I*-17 Electrical properties of SBN 50 films by I-V and C-V measurements. (a) dielectric constant versus Bias voltage (V) and (b) tangent δ (tan δ) versus bias voltage (V) measured by C-V measurements. (c) Leak current [A / cm²] versus applied voltage

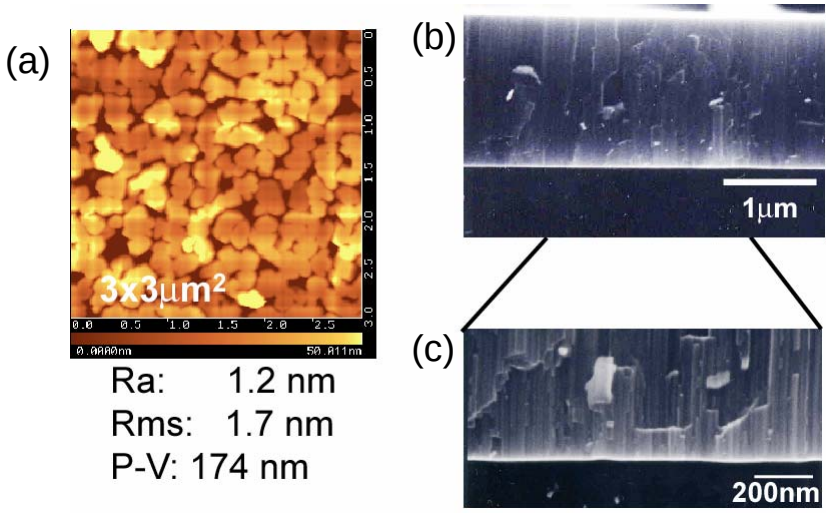

Fig. *I*-18 AFM image of SBN 50 film fabricated on Nb:STO (Nb:0.5%) (a), cross-sectional SEM image of SBN film (a) and (b). Clear surface and dense columnar were clearly observed.

Appendix *I*-5 Conclusions

It has been difficult that fabrication of only *c*-axis oriented SBN50 films on step $SrTiO_3$. However, we succeeded in fabricating only *c*-axis oriented SBN 50 films of SrO and BaO buffered step STO substrate (A-site terminated substrate).

SBN 50 films were epitaxially grown on MgO (001), STO (001) and LAO(001) substrates. $Sr_xBa_{1-x}Nb_2O_6$ (x = 0.25 – 1.0) composition thin films were fabricated on MgO substrate. The relative frequency shift was measured by microwave microscope. The peak maximum of value is observed around x = 0.65 little difference from reported maximum. Furthermore, we tried to characterize electrical properties of SBN 50 films. But large leak current was observed.

Reference

[1] R. R. Neurgaonkar et al., Ferroelectrics (1988) **87** 167-179

[2] J. R. Carruthers et al., J. Electrochem. Soc. Solid State Science (1970) 1426-1430

[3] A.A. Ballman and H. Brown, J. Cryst. Growth 1 (1966) 311.

[4] M. Kawasaki, K. Takahashi, M. Maeda, R. Tsuchiya, M. Shinohara, O. Ishiyama, T. Yonezawa, M. Yoshimoto and H. Koinuma, Science 266 (1994) 1549.

Appendix *II* Related Magnetic Theory

We discussed ferromagnetic properties of Co doped TiO2 thin films, but the magnetic origin is conversable. There have been studied some ferromagnetic interaction theories such as RKKY interaction, double exchange interaction, super exchange interaction and so on. From our transport results, it is difficult to be explained by ferromagnetic theory so far of ferromagnetic origin of Co doped TiO_2. But former ferromagnetic interaction theory will help us to understand ferromagnetic origin of Co doped TiO_2. And also show magnetic circular dichrorism theory, which important technique for diluted magnetic semiconductor.

Appendix *II*-1 Magnetic Circular Dichroism (MCD)[1]

The Zeeman splitting causes polarization dependent optical anisotropies, i.e., magneto-optic effects. The anisotropy of optical absorption causes magnetic circular dichroism (MCD). The anisotropy of the refractive index causes the Faraday effect, i.e., rotation of the polarization plane of linear-polarized light. The Faraday effect and MCD are closely related effects, and they contain identical information about the electronic structure of the material.

Measurement of the Zeeman splitting directly probes the modification of the band structure induced by the external magnetic field. The magnitude of the Zeeman splitting can be tens of meV in typical DMS[2], hence the measurement is not difficult usually. However, when the concentration of magnetic ions is low, or the optical transition spectrum is broadened by the highly concentrated magnetic ions, or poor quality of samples, or heavy doping of carriers, the precise measurement of the splitting becomes difficult. The field-induced modification of the band structure can be detected more precisely and more rapidly by measuring MCD by using the polarization modulation technique. Here we primarily use the MCD data to discuss the electronic structures of DMS.

When no magnetic field is applied, the transmitted light intensity through a sample can be expressed as

$$I = I_0 \exp\left(-k(E)L\right) \quad (1)$$

where $k(E)$ is the optical absorption coefficient at energy E without a applied magnetic field, L is the sample thickness, and I_0 is the input light intensity. We assume that a magnetic field shifts the optical absorption spectrum without changing the spectral shape. The absorption coefficients k^+ and k^- for the σ^+ and σ^- polarizations can be expressed by

$$k^{+}(E) = k\left(E + \frac{\Delta E}{2}\right) \quad (2\text{-a})$$

$$k^{-}(E) = k\left(E - \frac{\Delta E}{2}\right) \quad (2\text{-b})$$

where ΔE is the Zeeman splitting energy, which is related to the effective g - value, g_{eff}, by the relation

$$\Delta E = -g_{eff}\,\mu_B H \quad (3)$$

μ_B is the Bohr magneton, and H is the external magnetic field. The magnetic circular dichroism (MCD), expressed in degrees is given by

$$\theta = \frac{90}{\pi}\frac{I^{+} - I^{-}}{I^{+} + I^{-}} \quad (4)$$

By substituting (1), (2-a) and (2-b) into (4), we obtain the following expression :

$$MCD = -\frac{45}{\pi}\Delta E\frac{dk(E)}{dE} \quad (5)$$

Equation (5) shows that MCD is proportional not only to the Zeeman splitting energy ΔE but also to the energy derivative of the light absorption coefficient dk/dE. The value of the Zeeman splitting ΔE can be deduced from combined measurements of MCD and absorption spectra. The value of ΔE thus determined for $Cd_{1-x}Mn_xTe$, agrees with the value obtained from the direct measurement of the Zeeman splitting. This indicates the applicability of (5).

Figure *II*-1 shows a schematic diagram of the MCD measurement in the transmission geometry. Monochromatic light from a Xe lamp in a spectrum range from 200nm to 1000 nm is used. The polarization of light is modulated between σ^{+} and σ^{-} at 50 kHz by a photoelastic modulator. The transmitted light was detected by a photomultiplier and a lock-in amplifier. One degree of MCD corresponds to 7% difference of the transmitted light intensity.

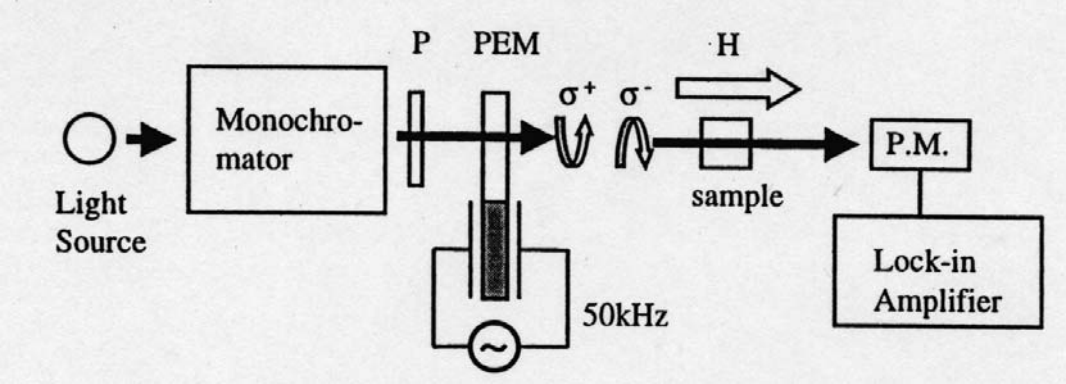

Fig. *II*-1 Experimental setup to measure magnetic circular dichroism (MCD). Alternating σ^+ and σ^- circular polarized light is generated by a combination of a linear polarizer (P) and a photoelastic modulator (PEM). Polarization dependent optical absorption of a sample under magnetic field H is detected by a photo- multiplier (P.M.) and a lock-in amplifier

Appendix *II*–2 Carrier-induced ferromagnetism (RKKY interaction)[3]

One of the candidates of the former framework is the well-known Ruderman-Kittel-Kasuya-Yosida (RKKY) interaction. The RKKY interaction is carrier-induced, sufficiently long ranged to account for the magnetic interaction in dilute systems, and has been put forward to explain the carrier (hole)-induced ferromagnetism observed in a IV-VI compound PdSnMnTe[4]. A mean field theory was also developed taking into account the feed-back mechanism between the magnetization polarization and the carrier polarization; magnetization polarization produces carrier polarization and it in turn produces magnetization polarization[5]. Since the mean field theory results in the same expression of T_C as that of the RKKY interaction, it is difficult and perhaps meaningless to distinguish between the two in terms of uniform polarization of magnetization.

T_C calculated from the RKKY interaction, using the exchange constant and the hole concentration, both determined from the magneto transport measurements, with mean free path as the cut-off length of the RKKY interaction was shown to be in good agreement with the experimentally obtained T_C[6]. This quantitative agreement seems to suggest that the RKKY picture (or the mean field picture) may be a good starting point to understand the appearance of ferromagnetism in (Ga,Mn)As, especially for the metallic samples. The sign of the RKKY interaction is in effect only ferromagnetic because the first zero of the oscillation, beyond which the interaction changes its sign and becomes antiferromagnetic, occurs at much greater distance (because of the low hole concentration) than the cut off length of the interaction. The RKKY picture can also explain the absence of ferromagnetism in n-type materials; in n-type materials, the small effective mass together with the small $N_0\alpha$ (about 0.2 eV) makes it

difficult for the ferromagnetic in-teraction to overcome the direct antiferromagnetic coupling among Mn. The mean field picture was used to explain the hole-induced ferromagnetism in II-VI quantum wells[7].

Figure *II*-2 shows Tc calculated by the mean field theory. Here, Tc was calculated from the hole free energy, which was obtained by solving a 6x 6 Luttinger Hamiltonian taking into account the presence of the p-d interaction, x= 0.05 and $|N_0\beta|$ = 1.0eV was assumed and the direct antiferromagnetic interaction among Mn was neglected. Fig. *II*-2 implies that $N_0\beta$ = 1.3 eV to obtain T_C = 110 K for p =3.5 x $l0^{20}$ cm^{-3}, in rather good agreement with the range of $N_0\beta$ inferred from experiments.

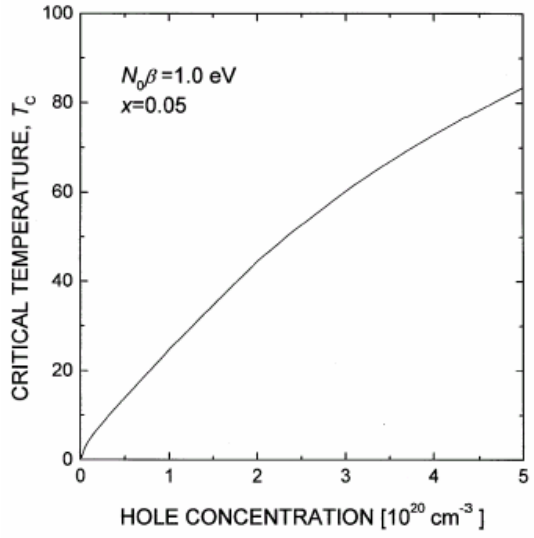

Fig. *II*-2 Ferromagnetic transition temperature T_C as a function of the hole concentration calculated by a mean-field theory. x = 0.05 and $|N_0\beta|$ = 1.0 eV are assumed. T_C was obtained from the hole free energy calculated from a 6x6 Luttinger Hamiltonian with p-d exchange.

Ferromagnetism in insulating samples can be understood along the same line, if one considers the difference between the length scales associated with the transport and the magnetism In insulating samples close to the metal-insulator transition, the localization length is smaller than the sample size (millimeters) but may still be significantly larger than the length scale of magnetic interactions (nanometers), thus making the RKKY-like interaction a good starting point, although localization phenomena would be increasingly important.

The understanding of the ferromagnetism by the RKKY interaction (or by the mean-field theory) is not adequate. It was pointed out[8], for example, that the behavior of the critical scattering may be qualitatively different when the spin-spin interaction is of long range (present case) as opposed to the short-range interaction, which may call for the localization effect to be explicitly included in the framework. Another issue is the validity of the RKKY framework itself. Upon derivation of the RKKY interaction, the exchange is assumed to be small compared to the Fermi energy E_F. The present case of (Ga,Mn)As, and probably (In,Mn)As as well, does not satisfy this condition, where the exchange is of the

order of 1 eV and EF around 300 meV. Although this may invalidate the perturbative approach, it does not affect the conclusion obtained by the mean-field theory. Furthermore, recent Monte Carlo simulation on two-dimensional systems pointed out that the expression for T_C may still be valid. The simulation showed a temperature versus magnetization curve very similar to that can be obtained by mean-field theory[9]: As temperature goes below Tc, the magnetization shows an initial steep rise followed by a plateau and then a rise towards saturation.

Appendix *II* - 3 Double exchange

The other approach to the understanding of the ferromagnetism in III-V DMSs starts from the d-band formed by transition metal impurities. Based on the Korringa-Kohn-Rostoker coherent-potential and local density approximation (KKR-CPA-LDA) calculation of the ground-state energy of (In,Mn)As, which revealed that the ferromagnetic phase is indeed stable, Akai stressed the d-character of the holes and invoked a double-exchange picture for the observed ferromagnetism[10]. The energy gain of the ferromagnetic phase is proportional to the carrier concentration and therefore the calculation showed that compensating the holes results in destabilization of the ferromagnetic state. By introducing donors sufficient to compensate Mn that provides holes, spin-glass phase becomes more stable. It is also interesting to point out that the calculation indicates that (In,Mn)As is half metallic, as was pointed out for (Ga,Mn)As using hypothetical ordered alloy and local spin density approximation[11,12].

Since (In,Mn)As and (Ga,Mn)As are random alloys, the conventional double-exchange picture must be extended to include the random distribution of dilute Mn atoms in this case. If one can experimentally determine the character of conduction holes, which is a mixture of As p-orbitals and Mn d-orbitals, it will advance our understanding of the nature of ferromagnetism observed in (Ga,Mn)As and (In,Mn)As further.

Appendix *II* – 4 Partial ferromagnetism in p-type (In,Mn)As

Partial ferromagnetism observed in p-type (In,Mn)As may be understood along the same line as (Ga,Mn)As[13]. The coexistence of remnant magnetization and unsaturated spins, and the large negative magnetoresistance extending to high fields, can be explained by the formation of unsaturated bound magnetic polarons (BMPs) having partially aligned (canted) spins in them. At B = 0, BMPs are randomly oriented showing no net moment With a small

applied field (the field at which hysteresis ends, i.e. 20 mT), BMPs are rotated and a net moment appears due to the aligned part of spins in BMPs. It is not clear whether a BMP itself acts as a magnetic domain or there is a magnetic domain structure containing a number of BMPs. The alignment of the canted spins at higher fields is responsible for the paramagnetic response as well as for the large negative magnetoresistance, because the alignment of spins means breaking of BMPs responsible for the carrier localization by achieving magnetic homogeneity. Since the nearest-neighbor exchange interaction between Mn is antiferromagnetic[14], the ferromagnetic interaction among Mn spins must again be hole-induced. Canting of spins can be caused by randomly oriented magnetoelastic anisotropy due to high density of lattice mismatch dislocations in the film.

Reference

[1] K. Ando, "Magneto-Optics of Diluted Magnetic Semiconductors: New Materials and Applications", in Magneto-Optics (Eds. S. Sugano and N. Kojima, Springer Series in Solid State Sciences 128.1999. ISBN 3-540-65961-7), pp.211-244.

[2] A. Twardowski, M. Nawrocki, J. Ginter, Phys. Stat. Sol., (b) 96, 497 (1979)

[3] H. Ohno; J. Magn. Magn. Mater. 200 (1999) 110-129

[4] T. Story, R.R. Galazka, R.B. Frankel, P.A. Wolff; Phys. Rev. Lett. 56 (1986) 777.

[5] T. Dietl, A. Haury, Y. Merle d' Aubigné, Phys. Rev. B 55 (1997) R3347.

[6] F. Matsukura, H. Ohno, A. Shen, Y. Sugawara, Phys. Rev. B 57 (1998) R2307.

[7] A. Haury, A. Wasiela, A. Arnoult, J. Cibert, S. Tatarenko, T. Dietl, Y. Merle d' Aubigné, Phys. Rev. Lett. 79 (1997) 511.

[8] A. Haury, A. Wasiela, A. Arnoult, J. Cibert, S. Tatarenko, T. Dietl, Y. Merle d' AubigneH , Phys. Rev. Lett. 79 (1997) 511.

[9] T. Dietl, A. Haury, Y. Merle d' Aubignen , Phys. Rev. B 55 (1997) R3347.

[10] H. Akai, Phys. Rev. Lett. 81 (1998) 3002.

[11] M. Shirai, T. Ogawa, I. Kitagawa, N. Suzuki, J. Magn. Magn. Mater. 177-181 (1998) 1383.

[12] T. Ogawa, M. Shirai, N. Suzuki, I. Kitagawa, J. Magn. Magn. Mater. 196-197 (1999) 428.

[13] H. Ohno, H. Munekata, T. Penney, S. von MolnaH r, L.L. Chang, Phys. Rev. Lett. 68 (1992) 2664.

[14] S. von, Molnár, H. Munekata, H. Ohno, L.L. Chang, J. Magn. Magn. Mater. 93 (1991) 356.

Publication List

Publications

1. "Combinatorial Fabrication and Characterization of Ferromagnetic Ti-Co-O System"
M. Murakami, Y. Matsumoto, M. Nagano, T. Hasegawa, M. Kawasaki and H. Koinuma; Appl. Surf. Sci. accepted.
2. "Structural control and combinatorial doping of titanium dioxide thin films by laser molecular beam epitaxy"
Y. Matsumoto, M. Murakami, T. Hasegawa, T. Fukumura, M. Kawasaki, P. Ahmet, K. Nakajima, T. Chikyow and H. Koinuma; Appl. Surf. Sci., 189, 3-4, 344-348 (2002)
3. "High Throughput Characterization of Magnetic Semiconductor Thin Films with a Scanning SQUID Microscope"
X.J. Fan, C.M. Chen, M. Murakami, R. Takahashi, Y. Matsumoto, T. Hasegawa, T. Fukumura, Proc. MRS Fall Meeting, Boston, Nov. 26-30 (2001).
4. "Ferromagnetism in Co-Doped TiO_2 Rutile Thin Films Grown by Laser Molecular Beam Epitaxy"
Y. Matsumoto, R. Takahashi, M. Murakami, T. Koida, X. J. Fan, T. Hasegawa, T. Fukumura, M. Kawasaki, S. Koshihara, and H. Koinuma; Jpn. J. Appl. Phys. 40 pt2 11B L1204-L1206 (2001)
5. "High throughput fabrication of transition-metal-doped epitaxial ZnO thin films: A series of oxide-diluted magnetic semiconductors and their properties"
Z.W. Jin, T. Fukumura, M. Kawasaki, K. Ando and H. Saito, T. Sekiguchi, Y. Z. Yoo, M. Murakami, Y. Matsumoto, T. Hasegawa, H. Koinuma; Appl. Phys. Lett. **78** 24 3824-3826 (2001)
6. "Anatase TiO_2 thin films grown on lattice-matched $LaAlO_3$ substrate by laser molecular-beam epitaxy"
M. Murakami, Y. Matsumoto, and K. Nakjima, T. Makino and Y. Segawa, T. Chikyow and P. Ahmet, M. Kawasaki and H. Koinuma; Appl. Phys. Lett. **78** 18 2664-2666 (2001)
7. "Room-Temperature Ferromagnetism in Transparent Transition Metal-Doped Titanium Dioxide"
Y. Matsumoto, M. Murakami, T. Shono, T. Hasegawa, T. Fukumura, M. Kawasaki, P. Ahmet, T. Chikyow, S. Koshihara, and H. Koinuma; Science **291** 854-856 (2001)
8. “Fabrication of transition-metal-doped epitaxial ZnO thin films and their optical and magnetotransport properties”
Zhengwu Jin, T. Fukumura, Y.Z. Yoo, M. Murakami, Y. Matsumoto, T. Sekiguchi, M.

Kawasaki, T. Hasegawa, H. Koinuma; Proc. of the Fifth Symp. Atomic-scale Surface and Interface Dynamics 357-360 (2001)

9. "Concept and Develpoment of Combinatorial Laser MBE for Oxide Electronics"
H. Koinuma, M. Kawasaki, T. Itoh, A. Ohtomo, M. Murakami, Z.W. Jin, and Y. Matsumoto; Physica C **335** 245-250 (2000)

10. "Combinatorial laser MBE syntesis of 3d ion doped epitaxial ZnO thin films"
Z.W. Jin, M. Murakami, Y. Matsumoto, A. Ohtomo, M. Kawasaki, and H. Koinuma; J. Crysta. Growth 214/215 55-58 (2000)

11. "Combinatorial Laser Molecular Beam Epitaxy (MBE) Growth of Mg-Zn-O Alloy for Band Gap Engineering"
Y. Matsumoto, Makoto Murakami, Z.W. Jin, A. Ohtomo, M. Lippmaa, M. Kawasaki, H. Koinuma; Jpn. J. Appl. Phys. **38** L603-L605 (1999)

12. "Atomic-scale controlled growth of anatase thin films by laser molecular beam epitaxy"
Y. Matsumoto, M. Murakami, T. Ohsawa, H. Koinuma, M. Kawasaki, P. Ahmet, K. Nakajima, T. Chikyow; Proc. of the Fifth Symp. Atomic-scale Surface and Interface Dynamics 319-322 (2001)

13. "Combinatorial synthesis and high throughput evaluation of doped TiO_2 thin films for the development of photocatalysts" Y. Matsumoto, M. Murakami, Z.W. Jin, A. Nakayama, T. Yamaguchi, T. Ohmori, E. Suzuki, S. Nomura, M. Kawasaki, H. Koinuma; Proc. SPIE **3941** 19-27 (2000)

松本祐司、村上 真、大澤健男、鯉沼秀臣、「コンビナトリアルナノテクノロジーと酸化物透明磁石の開発」、 機能材料、21[9], 45-50 (2001)

Presentation

○"Structural and Magnetic Characterizations of Room Temperature Ferromagnetic Co Doped TiO_2 Thin Films Fabricated by Combinatorial Laser Molecular Beam Epitaxy "
M. Murakami, Y. Matsumoto, M. Nagano, T. Hasegawa, T. Chikyow, K. Ando, M. Kawasaki, H. Koinuma; Carrier Interactions and Spintronics in Nanostructures' (CISN2003), March 10-12, 2003 at NTT Atsugi R&D center

○ "Combinatorial Fabrication and Characterization of Transparent Magnetic Ti-Co-O System""
M. Murakami, Y. Matsumoto, X.J. Fan, T. Hasegawa, P. Ahmet, T. Chikyow, K. Ando, S.

Sasaki, H. Koinuma; The Second U.S.-Japan Workshop on Combinatorial Materials Science and Technology, December 9 – 11, 2002, Winter Park, Colorado, USA

○"Combinatorial Synthesis and High Throughput Characterization of Transition Metal Doped TiO_2 Thin Films"

Makoto MURAKAMI, Zhengwu JIN, Ryota TAKAHASHI, Yuji MATSUMOTO, Masashi, KAWASAKI, and Hideomi KOINUMA; PCPM 2000 The 3rd NIMC International Symposium on Photoreaction Control and Photofunctional Materials March, 2000 AIST Tsukuba Research Center Auditorium

○"ROOM TEMPERATURE TRANSPARENT MAGNET BY COMBINATORIAL LASER MBE"

M. MURAKAMI, Y. MATSUMOTO, T. FUKUMURA, T. SHONO, T. HASEGAWA, P. AHMET, T. CHIKYOW, M. KAWASAKI[3)], H. KOINUMA; The 12th Materials Research Science of Japan in KSP, Dec.7-8, 2000

Presentations in Japanese Applied Physics Society

1. ″コンビナトリアルレーザーMBEによるTiO_2およびTiN薄膜の作製とその高酸素加熱処理効果″ 村上真、松本祐司、金政武、川崎雅司、鯉沼秀臣； 第 46 回応用物理関係連合講演会 東京理科大学（野田キャンパス） 1999 年 3 月 **（講演奨励賞受賞）**
2. ″コンビナトリアルレーザーMBE法による遷移金属ドープTiO_2薄膜の作製とその評価″ 村上真、松本祐司、金政武、小宮山大輔、大友明、川崎雅司 鯉沼秀臣； 第 60 回応用物理学会学術講演会 甲南大学 1999 年 9 月
3. ″コンビナトリアルレーザーMBE法による$LaAlO_3$ (001)上に作製したTiO_2 薄膜の評価″ 村上真、高橋竜太、松本祐司、川崎雅司、鯉沼秀臣； 第 47 回応用物理関係連合講演会 青山大学 2000 年 3 月
4. ″コンビナトリアルレーザーMBE法による高品質アナターゼエピタキシャル薄膜の作製と評価″ 村上真、松本祐司、牧野哲征、瀬川勇三郎、アヘメト･パールハット、中島清美、知京豊裕、川崎雅司、 鯉沼秀臣； 第 61 回応用物理学会学術講演会 北海道工業大学 2000 年 9 月
5. ″コンビナトリアルレーザーMBE法によるCoをドープした二酸化チタン薄膜の作製とその磁気特性″ 村上真、松本祐司、福村知昭、長谷川哲也、川崎雅司、鯉沼秀臣；第 61 回応用物理学会学術講演会 北海道工業大学 2000 年 9 月
6. ″コンビナトリアルレーザーMBE法によるCoをドープしたチタン系酸化物の作製とその磁気特性″ 村上真、松本祐司、福村知昭、范暁娟、長谷川哲也、川崎雅司、鯉沼秀臣； 第 48 回応用物理関係連合講演会 明治大学 2001 年 3 月
7. ″コンビナトリアルレーザーMBE法による$(Sr_xBa_{1-x})Nb_2O_6$薄膜の作製″ 村上 真、H. Y. Hwang、

大友 明、Theo Siegrist、川崎 雅司、鯉沼 秀臣；第 62 回応用物理学会学術講演会　愛知工業大学　2001 年 9 月

8. ″(Sr_xBa_{1-x})Nb_2O_6薄膜のコンビナトリアル作製 （SrO buffer層の効果）″村上 真、H. Y. Hwang、大友 明、川崎 雅司、鯉沼 秀臣；第 49 回応用物理関係連合講演会　東海大学　2002 年 3 月

9. ″コンビナトリアルレーザーMBE法によるCo-Ti-O薄膜の作製及びその磁気特性″村上真、松本祐司、范暁娟、長谷川哲也、アヘメト･パールハット、知京豊裕、安藤功兒、鯉沼秀臣；第 63 回応用物理学会学術講演会　新潟大学　2002 年 9 月

9. ″コンビナトリアルレーザーMBE法による温度傾斜TiO_2-CoO組成傾斜薄膜の作製と高速評価″村上 真，松本 祐司，長野 みか，長谷川 哲也，知京 豊裕，安藤 功兒，川崎 雅司、鯉沼 秀臣；第 49 回応用物理関係連合講演会　神奈川大学　2003 年 3 月（予定）

Acknowledgements

This thesis is the summery of the studies carried out in Tokyo Institute of Technology from 1998 to 2003 under the direction of Professor Hideomi Koinuma. I would like to express my best gratitude to Prof. Koinuma for his valuable advices continuous encouragements and guidance. I am much indebted to assistant professor Masashi Kawasaki and Mamoru Yoshimoto for their previous advises and continuous supports for this study. I want to express my best thanks to assistant Yuji Matsumoto who is my direct supervisor, for his helpful advice and intense discussions during this work. I would like to express my gratitude to Prof. Toyohiro Chikyow for TEM observations and nice advices to my research.

I appreciate Dr. P. Ahmet, Ms. K. Nakajima and Ms. T. Aoyama for TEM observations, Dr. H. Ofuchi and Prof. Nakai for XAFS measurements, Prof. Ando and Dr. Saito for MCD measurements, Prof. Hasegawa, X.J. Fan and M. Nagano for scanning SQUID measurements, Dr. Okazaki for microwave measurements and Dr. Makino for optical characterizations.

Thanks for Dr. H. Y. Hwang, A. Ohtomo and Dr. Y. Horibe for my working in Bell laboratory in United States. I express my gratitude Ms. M. Tanabe, K. Ono and R. Shiroki of Koinuma laboratory secretaries. Mr. K. Tamura and Mr. K. Terai work together with me in the same laboratory in 5 and 3 years.

I am much indebted to my co-workers, Mr. R. Takahashi and Z.W. Jin for their help. Thank is given to all of laboratory people who supported me. I also thank to others member of Koinuma, Yoshimoto, Kawasaki and Hasegawa laboratories for working with me in five years.

Finally, I express my deepest gratitude to my family for their endless support.

March 2003

Makoto Murakami